

**Investigation of the Molecular Mechanism of the Environmental Stress Cracking of  
Polyethylene by Molecular Simulation**

by

Sajjad Kavyani Baghbaderani

A thesis submitted in partial fulfillment of the requirements for the degree of

Doctor of Philosophy

in

Chemical Engineering

Department of Chemical and Materials Engineering

University of Alberta

© Sajjad Kavyani Baghbaderani, 2024

## Abstract

In this molecular dynamics (MD) simulation study, we investigated the impact of an environmental stress cracking (ESC) agent, nonyl ethoxylate (NE), on the packing and free volume coalescence in between polyethylene chains and the ESC agent, focusing on linear polyethylene (LPE) and branched polyethylene (BPE). Our study considered the size and spatial distribution of free volume holes at the [PE]-[NE] interfaces, analyzing the behavior of ethylene (E) and ethylene oxide (EO) segments of NE. BPE models with 10 and 82 hexyl branches/1,000 backbone carbons were employed, and NE concentrations ranged from 0.001 to 1.4 wt%. The results revealed that, regardless of NE concentration, there were no significant changes in the packings of LPE and BPE chains, as characterized by radial distribution functions (RDFs). However, molecular packings at the [PE]-[NE] interfaces varied with NE concentration, with E segments exhibiting stronger association with PE chains compared to EO segments. The Voronoi tessellation method was employed to assess free volume hole size and spatial distributions, indicating that more and larger holes formed around E segments. The Fourier mode analysis further explored the dynamics of free volume coalescence, showing that the power of free volume coalescence around NE molecules was mitigated by the presence of short-chain branches, reducing the free volume coalescence at the [PE]-[NE] interfaces.

Building on this, we extended our investigation to blends of unbranched and branched polyethylene with NE at 0.5 wt%. The branched polyethylene chains had 10 and 82 hexyl branches/1,000 backbone carbons, and we introduced a four-arm small alkane (7,12 hexyl

octadecane) into the blend. Previously, we showed that hexyl branches in branched polyethylene suppressed free volume coalescence, potentially slowing down cavitation. This part of the study, revealed that hexyl branches in the polyethylene chains of the blend exhibited behavior similar to that in pure branched polyethylene. However, hexyl branches in 7,12 hexyl octadecane intensified free volume coalescence, particularly around the hydrophilic EO segments of NE. Addition of 7,12 hexyl octadecane did not appear to slow down void formation, i.e. cavitation, suggesting that the effect of hexyl branches on coalescence dynamics depends on the size of the backbone to which they are attached. This study also revealed that the cavitation may start from the EO-segment of the NE molecule.

Expanding our focus to ESC resistance, we examined the impact of vinyl acetate-modified branch ends on free volume coalescence around NE distributed in a branched polyethylene. Compared to methyl branch ends, vinyl acetate branch ends exhibited higher affinity for the hydrophilic EO-segment of NE. Vinyl acetate branch ends also reduced the power of free volume size fluctuations around both E- and EO-segments, with the reduction correlating with increasing vinyl acetate concentration. The results aligned with experimental observations that the addition of copolymer ethylene vinyl acetate to low-density polyethylene improves ESC resistance, suggesting that vinyl acetate is capable of impeding crack propagation in PE.

In summary, our MD simulations provided insights into the intricate interplay between environmental stress cracking agents, polyethylene chains, and various structural modifications.

The findings contribute to a deeper understanding of ESC phenomena and offer potential pathways regarding predicting ESC by computational platforms.

## Preface

Every chapter presented in this thesis represents my original work. Certain chapters have been submitted or published in peer-reviewed journals and preprints, as detailed below.

A version of Chapter 3, is published at Polymer. As the first author, I was responsible for designing and executing simulations, collecting and analyzing data, and composing as well as revising the manuscript. Dr. Philip Choi was the supervising author involved in shaping the concept, proofreading, and revising the manuscript.

A version of Chapter 4, is published at Polymer Engineering & Science. As the first author, I was responsible for designing and executing simulations, collecting and analyzing data, and composing as well as revising the manuscript. Dr. Philip Choi and Dr. Joao Soares were the supervising authors involved in shaping the concept, proofreading, and revising the manuscript.

A version of Chapter 5, is ready for submission. As the first author, I was responsible for designing and executing simulations, collecting and analyzing data, and composing as well as revising the manuscript. Dr. Philip Choi and Dr. Joao Soares were the supervising authors involved in shaping the concept, proofreading, and revising the manuscript.

Chapters 1, 2, and 6 encompass the project introduction, fundamental simulation methodology, project summary, and future perspectives. Sajjad Kavyani authored these chapters, and they have not been published before.

## Acknowledgments

First and foremost, I want to thank my supervisors Dr. Phillip Choi and Dr. Joao Soares for their invaluable guidance, unwavering support, and mentorship throughout the course of this research. Their expertise, encouragement, and constructive feedback have been instrumental in shaping this thesis. I am truly fortunate to have had the opportunity to work under their supervision, and I am immensely thankful for their contributions to my academic and personal growth.

I extend my appreciation to Imperial Oil for their financial support through the IOL University Research Awards program, facilitated by my supervisor, which has played a pivotal role in making my Ph.D. program. Additionally, I am grateful for the computing resources and technical assistance provided by the Western Canada Research Grid (WestGrid). I am grateful for the recognition of my Ph.D. research from Alberta Innovates Graduate Student Scholarship, Alberta Graduate Excellence Scholarship, Mary Louise Imrie Graduate Student Award and Captain Thomas Farrell Greenhalgh Memorial Graduate Scholarship.

The support of my brilliant colleagues and friends has been instrumental in making my Ph.D. journey more manageable: Mr. Amirmasoud Badkoobeh, Mrs. Maryam Kazemi, Dr. Mohsen Soltanpour, Mr. Mojtaba Akbari, , Dr. Sadegh Aghapour Aktij, Dr. Subhamoy Mahajan and Dr. Wenyuan Sun.

I want to thank my parents, Mohammad Kavyani, and Akhtar Kavyani for their unconditional love and support, and my twin sister, Batoul Kavyani for her love and passion. And

at the end, I want to thank Marziyeh Motaghyian, who, with her smile, brought peace to my life, who helped me to move on the edge of order and chaos, and to be more ambitious. Love you all.

*Sajjad Kavyani Baghbaderani*

*April 2024*

# Table of Contents

<b>Chapter 1: Introduction</b> .....	<b>1</b>
<b>1.1. Background and literature review</b> .....	<b>2</b>
<b>1.2. Statement of problem</b> .....	<b>13</b>
<b>1.3. Objective(s)</b> .....	<b>14</b>
<b>1.4. Proposed research</b> .....	<b>15</b>
<b>1.5. Research outline</b> .....	<b>16</b>
<b>Chapter 2: Molecular Simulation Methodology</b> .....	<b>18</b>
<b>2.1. Molecular Dynamics (MD)</b> .....	<b>18</b>
2.1.1. The leap-frog algorithm: MD integrator .....	22
2.1.2. Temperature coupling .....	24
2.1.3. Pressure coupling .....	26
2.1.4. Forcefield .....	28
2.1.5. Radial distribution function.....	31
<b>2.2. Voronoi tessellation</b> .....	<b>34</b>
<b>Chapter 3: Free Volume Coalescence in Branched and Linear PE</b> .....	<b>37</b>
<b>3.1. Introduction</b> .....	<b>37</b>
<b>3.2. MD Simulation</b> .....	<b>40</b>
<b>3.3. Results and Discussion</b> .....	<b>43</b>
3.3.1. Radial Distribution Functions of PE and NE .....	43
3.3.2. Free Volume Hole Size and Spatial Distributions.....	47
<b>3.4. Conclusion</b> .....	<b>60</b>
<b>3.5. Acknowledgments</b> .....	<b>61</b>
<b>Chapter 4: Effect of Molecular Backbone Size on Free Volume Coalescence</b> .....	<b>62</b>
<b>4.1. Introduction</b> .....	<b>62</b>
<b>4.2. Molecular Dynamics (MD) Simulations</b> .....	<b>65</b>
<b>4.3. Results and Discussion</b> .....	<b>68</b>
4.3.1. Equilibration.....	68
4.3.2. Free Volume Holes Coalescence Dynamics.....	78

<b>4.4. Conclusion .....</b>	<b>83</b>
<b>4.5. Acknowledgments.....</b>	<b>83</b>
<b><i>Chapter 5: Effect Functionalizing the Branch-ends with Vinyl Acetate.....</i></b>	<b><i>84</i></b>
<b>5.1. Introduction .....</b>	<b>84</b>
<b>5.2. Molecular Dynamics (MD) Simulations .....</b>	<b>87</b>
<b>5.3. Results and Discussion .....</b>	<b>93</b>
5.3.1. Intermolecular Radial Distribution Functions .....	93
5.3.2. Coalescence Dynamics.....	103
<b>5.4. Conclusion .....</b>	<b>106</b>
<b>5.5. Acknowledgments.....</b>	<b>106</b>
<b><i>Chapter 6: Conclusions and Future Perspective .....</i></b>	<b><i>107</i></b>
<b>6.1. Overall conclusions.....</b>	<b>107</b>
<b>6.2. Future Perspective.....</b>	<b>108</b>
<b><i>Bibliography.....</i></b>	<b><i>110</i></b>

## List of Tables

<b>Table 1.</b> Cause of in-service failures[9] .....	2
<b>Table 2.</b> Descriptions of the Simulation Systems .....	42
<b>Table 3.</b> Mean free volume hole sizes of carbon atoms ( $\text{\AA}^3$ ) in the last four carbon atoms of butyl/hexyl branches and the last four carbon atoms at the end of the PE polymer chains in the LPE system. Carbon #4 is the terminal carbon. ....	47
<b>Table 4.</b> The number of frequency modes for the coalescing free volume $vfNE18 + vfNE19$ (E-segments) and $vfNE6 + vfNE7$ (EO-segments) for different systems. ....	59
<b>Table 5.</b> The total power ( <i>Amplitude</i> <sup>2</sup> ) for the coalescing free volume $vfNE18 + vfNE19$ (E-segments) and $vfNE6 + vfNE7$ (EO-segment) for different systems. ....	59
<b>Table 6.</b> Concentrations of LPE, BPE, SA and NE molecules used in the simulations.....	68
<b>Table 7.</b> The number of frequency modes of the coalescing free volume holes around different parts of the NE molecule.....	76
<b>Table 8.</b> The power of fluctuations for the coalescing free volume of different beads NE molecule. ....	77
<b>Table 9.</b> Descriptions of the Simulated Systems.....	92

## List of figures

<b>Figure 1.</b> Schematic representations of craze and crack in a polymer sample.....	4
<b>Figure 2.</b> Schematic representation of the ESC process .....	5
<b>Figure 3.</b> (a) Representation of polymer crystalline and amorphous structures [37]. And (b) stages of brittle fracture; (step 1) lamellae start to pull away, (step 2) tie-molecules are stretched, and (step 3) clean break of lamellae [38].....	6
<b>Figure 4.</b> Type of branches in polyethylene structure.....	8
<b>Figure 5.</b> ESCR versus percentage crystallinity.[44].....	10
<b>Figure 6.</b> Stress versus time to failure at various temperatures; (a), (b) and (c) have a common y axis. D designates a ductile region and B designates a brittle region. (a) In Igepal, (b) in air, (c) in air and Igepal at 60°C.[46].....	10
<b>Figure 7.</b> Creep deformation versus time for a PE sample (at 50°C, 2 MPa) for various concentrations of Igepal as ESC agent.[51].....	11
<b>Figure 8.</b> SEM images from the fracture surfaces of a PE sample, showing the effect of Igepal-630 concentration.[52] .....	12
<b>Figure 9.</b> The global MD algorithm.[64] .....	21
<b>Figure 10.</b> The leap-frog algorithm. It is so named because it involves positions $r$ and velocities $v$ leaping back and forth in a manner reminiscent of the movements of jumping frogs.....	23
<b>Figure 11.</b> The Coulomb Force, Shifted Force and Shift Function.[64].....	30
<b>Figure 12.</b> Voronoi tessellation method in 2D space. The right picture represents a half-plane in-between two particles A and B. ....	33
<b>Figure 13.</b> The algorithm of VT for particles with particle diameter $d$ , radial separation $R$ and position of $x_p$ .....	35
<b>Figure 14.</b> Probability distribution of free volume along LPE with 500 carbon atoms. ....	36
<b>Figure 15.</b> Structures of linear PE, branched PE and nonyl phenol ethoxylate (A), a common ESC agent and nonyl ethoxylate (B), an imitated ESC agent used in this work.....	43

<b>Figure 16.</b> Inter-chain radial distribution functions (RDFs) of linear polyethylene (LPE) and branched polyethylene (BPE) in the absence of NE (a) and in the presence of 1 (b), 5 (c) and 10 (d) NE molecules (i.e., $w_{NE} \sim 0.001 - 1.4$ wt%).	44
<b>Figure 17.</b> Intermolecular radial distribution functions for PE and NE's ethylene segments (E-segments) and ethylene oxide segments (EO-segments).	46
<b>Figure 18.</b> Free volume hole size of backbone carbons (blue) and carbons in the short chain branches (orange) of LPE and BPE chains as determined by the Voronoi tessellation (VT) method from an equilibrated snapshot (at 500 ns) of systems LPE, B4PE10, B4PE82, B6PE10 and B6PE82. The green dots on the x-axis denote the locations of the short chain branches ( <i>b</i> -Cs).	48
<b>Figure 19.</b> The probability distributions of free volume hole size ( $v$ ) for LPE and various BPE models without and with NE at different concentrations.	50
<b>Figure 20.</b> The probability distributions of free volume hole size ( $v$ ) around NE molecules in LPE and BPEs with NE at various concentrations.	51
<b>Figure 21.</b> The probability distributions of free volume hole size ( $v$ ) for ethylene segments (E-segments) and ethylene oxide segments (EO-segments) of NE molecules.	52
<b>Figure 22.</b> The time evolution of $vf_{NE18} + vf_{NE19}$ for systems, (a) LPENE10, (b) B4PE10NE10, (c) B4PE82NE10, (d) B6PE10NE10 and (e) B6PE82NE10.	54
<b>Figure 23.</b> The Fourier modes for $vf_{NE18} + vf_{NE19}$ (E-segments: a, b and c) and $vf_{NE6} + vf_{NE7}$ (EO-segments: d, e and f) of NE molecules.	55
<b>Figure 24.</b> Radial distribution functions (RDFs) of terminal carbons, branch carbons (terminal carbons excluded) and backbone carbons of BPEs as referenced to the E-segments of the NE molecules for different types of BPEs with 10 NE molecules.	58
<b>Figure 25.</b> Molecular structures of 7, 12 hexyl octadecane (SA) and nonyl ethoxylate (NE). The black, red and white dots signify carbon, oxygen and hydrogen atoms, respectively.	67
<b>Figure 26.</b> Radial distribution functions (RDFs) of LPE, BPE, SA and their branches using the E-segments (E) of NE as the reference for all fifteen simulation systems as depicted in Table 1.	71
<b>Figure 27.</b> Radial distribution functions (RDFs) of LPE, BPE, SA and their branches using EO-segments (EO) of NE as the reference for all fifteen simulation systems as depicted in Table 1.	72

<b>Figure 28.</b> Radial destruction functions (RDF) of SA molecules with referenced by BPE. ....	73
<b>Figure 29.</b> The probability distributions of free volume hole size ( $v$ ) of LPE, BPE, NE and SA, averaged on systems 10 to 15 in Table 6. ....	73
<b>Figure 30.</b> The probability distributions of free volume hole size ( $v$ ) around (a) E-segment, (b) EO-segment and (c) E-segment and EO-segment together. ....	74
<b>Figure 31.</b> The volume around the constituent atoms of NE molecule (see Figure 25 for the atomic indices) obtained from the last snapshot of the MD trajectories of all fifteen systems use.....	78
<b>Figure 32.</b> The number of Fourier modes vs. location points in NE molecules: EO-terminal ( $vfNE2 + vfNE3$ ), EO ( $vfNE10 + vfC\#11$ ), NE-middle ( $vfNE14 + vfNE15$ ), E ( $vfNE18 + vfNE19$ ) and E-terminal ( $vfNE21 + vfNE22$ ). ....	81
<b>Figure 33.</b> The power of fluctuations vs. location points in NE molecules: EO-terminal ( $vfNE2 + vfNE3$ ), EO ( $vfNE10 + vfC\#11$ ), NE-middle ( $vfNE14 + vfNE15$ ), E ( $vfNE18 + vfNE19$ ) and E-terminal ( $vfNE21 + vfNE22$ )......	82
<b>Figure 34.</b> Different macromolecular structures of PE used in this work.....	89
<b>Figure 35.</b> The chemical structures of a VA branch terminal and nonyl ethoxylate. The black, red and white dots signify carbon, oxygen and hydrogen atoms, respectively.....	91
<b>Figure 36.</b> Radial distribution functions (RDF) of PE models as determined by using (a) E-segments and (b) EO-segments as references, respectively. PE models used were LLDPE, BPE300 and BPE600. ....	94
<b>Figure 37.</b> Radial distribution functions (RDFs) of various types of carbons in branched PE models as determined by using E-segments as references.....	96
<b>Figure 38.</b> Radial distribution functions (RDFs) of various types of carbons in branched PE models as determined by using EO-segments as references.....	97
<b>Figure 39.</b> Radial distribution functions (RDFs) of atoms in VA (see Figure 40) averaged over all PE models (a) E-segments and (b) EO-segments as references. ....	98
<b>Figure 41.</b> The radial distribution functions of different chemical moieties on the branches as referenced by E-segments (a, b) and EO-segments (c, d). ....	99
<b>Figure 42.</b> The free volume hole size ( $v$ ) distributions for VA. ....	100

**Figure 43.** The free volume hole size ( $v$ ) distributions for different VA atoms: ether oxygen  $O$ , carbonyl carbon  $C=$ , carbonyl oxygen  $O=$  and terminal  $C$ . ..... 100

**Figure 44.** The free volume hole size ( $v$ ) distributions for (a) E-segments and (b) EO-segments, for different VA contents. For clarity, only the plots of BPE300 and BPE600, are shown. .... 101

**Figure 45.** The free volume fluctuations of skeletal atoms in the NE molecules from the last 20 snapshots of the MD trajectory for BPE300\_10VA20. .... 103

**Figure 46.** The power of the fluctuations of free volume coalescence for different atom pairs of the NE molecules. .... 105

# List of abbreviations and symbols

## *List of abbreviations*

AA	All-atom
ASP	Alkaline–surfactant–polymer
BPE	Branched polyethylene polymers
CG	Coarse-grained
EOR	Enhanced oil recovery
ESC	Environmental stress cracking
ESCR	Environmental stress cracking resistance
EO-segment	Ethylene oxide segments
E-segment	Ethylene segments
FF	Force field
HC	Hard-core
HDPE	High-density polyethylene
LLDPE	Linear low-density polyethylene
LDPE	Low-density polyethylene
MTTK	Martyna-Tuckerman-Tobias-Klein
MC	Monte Carlo
MD	Molecular dynamics
NE	Nonyl ethoxylate
NPE	Nonyl phenol ethoxylate
PME	Particle Mesh Ewald
PE	Polyethylene
RDF	Radial distribution function
SEM	Scanning electron microscope

SCB	Short-chain branches
SCG	Slow crack growth
SA	Small alkane
TraPPE	Transferable Potentials for Phase Equilibria
VA	Vinyl acetate
VT	Voronoi tessellation

## *List of symbols*

### *Alphabet symbols*

<b>a</b>	Box vector, $x$ component of the box, Chapter 2
<b>b</b>	Box vector, $y$ component of the box, Chapter 2
<b>c</b>	Box vector, $z$ component of the box, Chapter 2
$C_v$	Total heat capacity of the system, Chapter 2
$d$	Particle diameter, Chapter 2
$dW$	Wiener noise, Chapter 2
$\mathbf{F}_i$	Force acting on a particle, Chapter 2
<b>G</b>	A matrix tensor of box matrix <b>h</b> , Chapter 2
$g(r)$	Radial distribution function, Chapter 2
<b>h</b>	Box matrix, Chapter 2
$i$	Particle index, Chapter 2
$j$	Particle index, Chapter 2
$k$	Particle index, Chapter 2
$K$	Kinetic energy at temperature $T$ , Chapter 2
$K_0$	Kinetic energy at temperature $T_0$ , Chapter 2

$k_B$	Boltzmann's constant, Chapter 2
$k_b$	Bond force constant, Chapter 2
$k_\theta$	Angle force constant, Chapter 2
$k_\varphi$	The dihedral force constant, Chapter 2
$l$	Particle index, Chapter 2
$L$	The largest box matrix element, Chapter 2
$\mathcal{L}$	Lagrangian of <i>system + piston</i> , Chapter 2
$M$	Mass of the system, Chapter 2
$m_i$	Mass of particle $i$ , Chapter 2
$N$	Number of particles in the simulation box, Chapter 2
$N_{df}$	Total number of degrees of freedom, Chapter 2
$p$	Momentum of a particle, Chapter 2
$P(r)$	Probability of finding a particle at distance $r$ , Chapter 2
$q_i$	Particle charge, Chapter 2
$R$	Radial separation. Radius of the Voronoi cell, as sphere, Chapter 2
$r_0$	Equilibrium bond length, Chapter 2
$R_g$	Radius of gyration, Chapter 5
$r_i$	Position of particle $i$ , Chapter 2
$r_{ij}$	Distance between two particles $i$ and $j$ , Chapter 2
$r_{test}$	Radius of Voronoi cell during iteration, Chapter 2
$s_i$	Column vector consist of $[\xi_i, \eta_i, \zeta_i]$ , Chapter 2
$t$	Time of molecular dynamics simulation, Chapter 2
$T$	Temperature of the simulation box, Chapter 2
$T_0$	Temperature of the coupled heat bath (reference temperature), Chapter 2
$U(r^N)$	Potential energy of the entire phase space, Chapter 2
$V$	Volume of the box, Chapter 2
$V_{cell}$	Volume of the Voronoi cell, Chapter 2

$V_{free}$	Free volume, Chapter 2
$V_{fc\#}$	Volume of the Voronoi cell for carbon number #, Chapters 3, 4 and 5
$V_{hc}$	Hard-core volume of the particle, Chapter 2
$v_i$	Velocity of a particle, Chapter 2
$W$	Strength of the pressure coupling, Chapter 2
$x_p$	The position of the particles, Chapter 2

### ***Greek symbols***

$\beta$	Isothermal compressibility, Chapter 2
$\delta$	Dirac's delta function, Chapter 2
$\Delta t$	Timestep, Chapter 2
$\epsilon_0$	Dielectric constant of the medium, Chapter 2
$\epsilon_{ij}$	Depth of the potential well between two particles $i$ and $j$ , Chapter 2
$\eta_i$	Factor of $\mathbf{b}$ in the $span(\mathbf{a}, \mathbf{b}, \mathbf{c})$ , Chapter 2
$\theta_0$	Equilibrium angle value for three particles $i, j$ and $k$ , Chapter 2
$\theta_{ijk}$	Angle between three particles $i, j$ and $k$ , Chapter 2
$\lambda$	Scaling factor of velocities, Chapter 2
$\xi_i$	Factor of $\mathbf{a}$ in the $span(\mathbf{a}, \mathbf{b}, \mathbf{c})$ , Chapter 2
$\pi$	Pi number, Chapter 2
$\sigma_{ij}$	Size of two interacting particles, Chapter 2
$\zeta_i$	Factor of $\mathbf{c}$ in the $span(\mathbf{a}, \mathbf{b}, \mathbf{c})$ , Chapter 2
$\tau$	Time constant, Chapter 2
$\tau_P$	Pressure time constant, Chapter 2
$\varphi_{ijkl}$	The dihedral angle between particles $i, j, k$ and $l$ , Chapter 2

### ***Operators***

$\dot{a}$	First order time derivative, Chapter 2
-----------	--

$\mathbf{A}^T$	Transpose of matrix $\mathbf{A}$ , Chapter 2
$\det(\cdot)$	Determinant of a tensor, Chapter 2
$Tr(\cdot)$	Trace of a tensor, Chapter 2
$\Sigma$	Sum, Chapter 2

# Chapter 1: Introduction

---

Anticipating and preventing unexpected failures are crucial aspects of process design, particularly when it comes to using polymers in various industrial applications. Over the past few decades, our understanding of these failures has improved, resulting in a reduction in the occurrence of such incidents. However, the complexity of these failures, particularly Environmental Stress Cracking (ESC), remains a significant challenge [1]. In the context of polymers, these failures manifest as sudden, brittle cracks during service, with the potential for catastrophic consequences [2], [3]. What compounds the issue is that polymer failures often result from a combination of seemingly minor factors, including residual stresses [4], a brief contact with minor components, temperature fluctuations [5]–[7], and exposure to diverse environments [8], some of which may go unnoticed. Table 1 outlines the causes of service failures for polymers in the UK [9]. Notably, environmental factors, encompassing the ESC phenomenon—arising from the interplay of prolonged stress and environmental conditions—feature prominently. It is worth highlighting that among the effects listed in Table 1, chemical attack and "other" factors are also linked to environmental influences. Hence, this table underscores the substantial role played by the environment in polymer failures.

**Table 1.** Cause of in-service failures[9]

Type of failure	Percentage occurrence
Environmental stress cracking	25
Dynamic fatigue	15
Notched static rapture	14
Creep attack	8
Chemical attack	7
UV attack	6
Thermal degradation	4
Other	21

Most of the failures due to ESC are very hard to predict since; *(i)* the active environment is a minor component, *(ii)* the amount of stress for the failure is very small [10], such as residual stress from molding and *(iii)* the time of contact of the polymer with the environment is very short. The two main issues of chemical degradation and ESC should be significantly considered in the designing process, especially in materials and structures exposed to challenging environments.

## **1.1. Background and literature review**

As previously discussed [11], ESC is a phenomenon that arises from the combined effects of prolonged stress applied to a polymer and its exposure to specific chemical agents in the surrounding environment, often referred to as the ESC agents. In situations where such ESC agents are absent, the primary mechanism governing polymer failure becomes creep [12]. Creep describes

a material's inherent tendency to undergo permanent deformation when subjected to constant stress, such as tensile, shear, or flexural stress, especially over extended durations [13], [14]. The severity of creep is more pronounced when the polymer operates at elevated temperatures near its melting point, typically with the applied stress remaining below the material's yield point. The extent of creep is influenced significantly by two key factors: temperature [15] and strain rate [16], [17]. It is widely postulated that the root cause of brittle failure during creep is the disentanglement of polymer chains due to the continuous application of stress [13], [18], [19]. In essence, creep is an outcome of the viscoelastic properties intrinsic to polymer materials [20].

Creep and ESC share commonalities in their underlying processes. Creep progresses through distinct stages: *i*) initiation of craze formation, *ii*) growth and expansion of these crazes, and *iii*) eventual fracture. ESC, while following a similar pattern to creep, differentiates itself by the presence of prolonged stress combined with exposure to an ESC agent. It is noteworthy that creep has occasionally been described as a form of ESC when air serves as the ESC agent. Crazes are essentially pseudo-cracks that originate at a consistent angle relative to the applied load. They are filled with numerous microfibrils (represented in Figure 3) within the polymer, aligning themselves parallel to the direction of stress [21]. Importantly, a polymer material entirely affected by crazes can continue to endure a significant amount of stress without undergoing catastrophic failure. Within crazing, segments of the polymer material are drawn out from the adjacent bulk material, forming cavitated regions in which the unaltered surfaces are connected by aligned polymer fibrils [22]. Figure 1 provides a visual representation illustrating the distinction between a crack and a craze within a polymer.

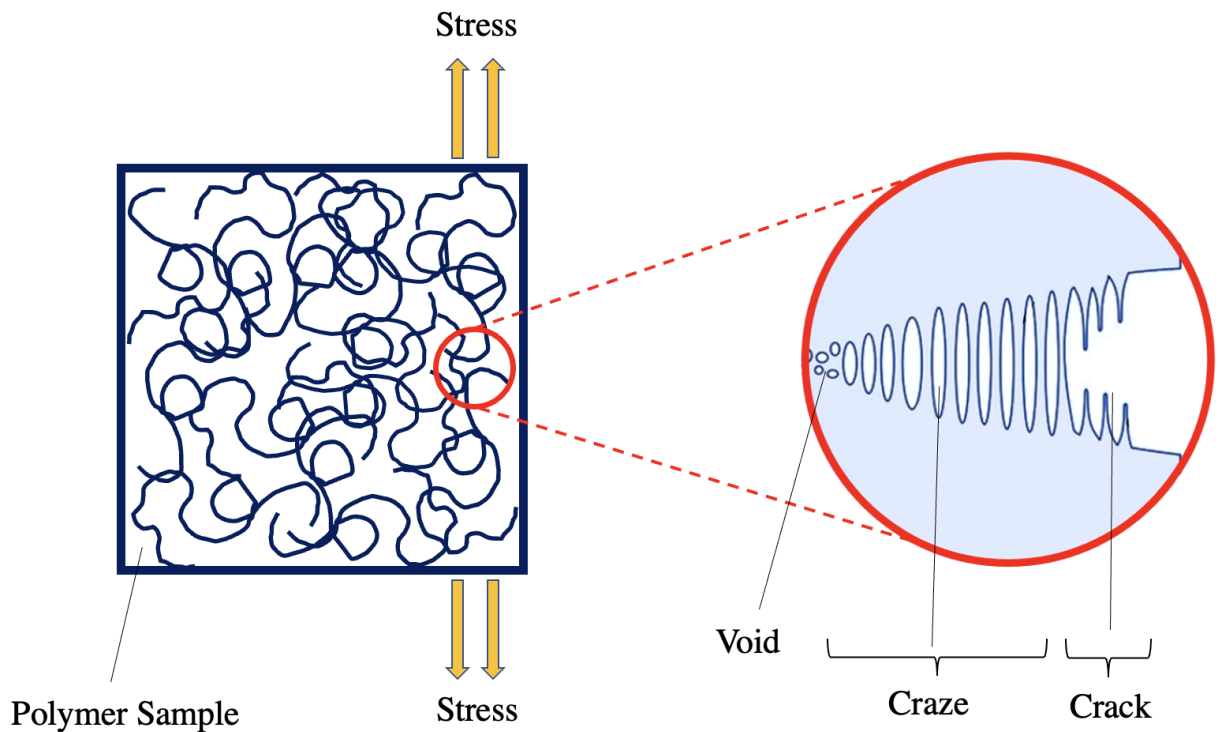


**Figure 1.** Schematic representations of craze and crack in a polymer sample.

Within ESC, the ESC agent plays a pivotal role by diffusing into the polymer structure [23], expediting the separation of polymer chains [19], [24]. The stages in ESC typically include: *i*) absorption of the fluid, *ii*) plasticization, *iii*) voids formation (cavitation), *iv*) initiation of crazes, *v*) cracks growth, *vi*) polymer extension, and ultimately, *vii*) fracture. Notably, the rate at which the polymer absorbs the ESC agent stands out as the primary determinant of ESC [25]. An accelerated absorption rate leads to more rapid failure. The ESC agent penetrates the polymer structure from areas characterized by stress dilation, including defects and crazes, thereby

diminishing the polymer's yield stress [26]. This reduction ultimately leads to polymer failure. Figure 2 provides a visual schematic illustrating the process of ESC.

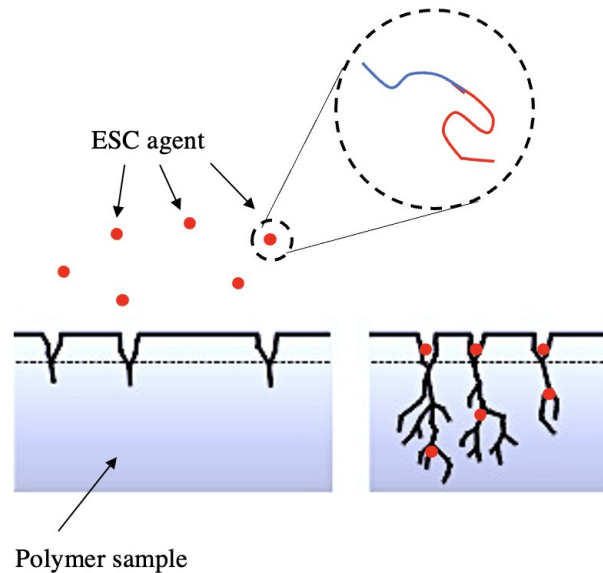


**Figure 2.** Schematic representation of the ESC process. The ESC agents (red dots), are amphiphilic molecules consist of two heads, hydrophobia (blue line) and hydrophilic heads (red line).

When subjected to stress, thermoplastic polymers, such as PE, undergo a process wherein they develop crazes prior to experiencing cracking [27], [28]. These crazes are imperceptible on the surface, and even after craze formation, the polymer retains its ability to bear loads [29]. When dealing with thermoplastic polymers, it is imperative to address the following questions [30]. Why certain environments cause crazing in a polymer under stress? How can the resistance of the polymers be improved? What is the appropriate test to determine the resistivity of the polymers?

To initiate the formation of crazes within a polymer, a significant degree of molecular mobility [31], [32] within the polymer matrix is required. This concept is rooted in the idea that an increased free volume can create localized regions within the polymer that become more accessible under stress [33]. As this local free volume expands, it enhances the mobility of polymer chains within these regions [34]. Notably, crazes tend to initiate at defects in the polymer where stress concentrations are pronounced. The ESC agent can act as a catalyst for crazing by lubricating the polymer chains, facilitating their easy movement past one another [35]. In the case of PE, which is predominantly semi-crystalline, crazing primarily occurs within the amorphous regions [36].

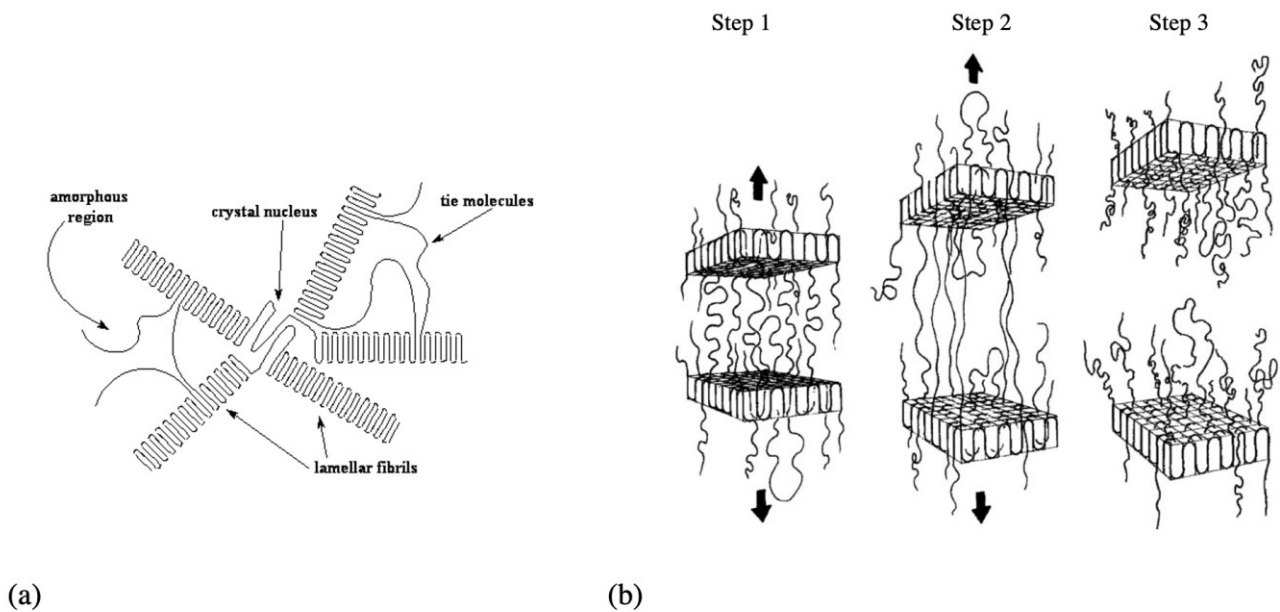


**Figure 3.** (a) Representation of polymer crystalline and amorphous structures [37]. And (b) stages of brittle fracture; (step 1) lamellae start to pull away, (step 2) tie-molecules are stretched, and (step 3) clean break of lamellae [38].

When subjected to stress, such as tensile loading, the tie molecules that link lamellae (as illustrated in Figure 3) elongate in the direction of the applied load. However, there comes a point at which they can no longer stretch. Under conditions of low-level, prolonged loading, these tie molecules begin to disentangle, leading to interlamellar failure. It is worth noting that in situations involving ductile deformation, lamellae break down into smaller units [30].

Environmental Stress Cracking Resistance (ESCR) in polymers is a critical indicator of their ability to withstand slow crack growth (SCG) throughout their intended service life [7] – [9]. Several characteristics of PE play roles in determining its ESCR, including molecular weight averages, molecular weight distribution [10], [11], degree of crystallinity [44], degree of branching [45], and the diffusion rate of the ESC agent through the amorphous phase of PE [46]. However, researchers have increasingly identified that the degree of branching and the degree of crystallinity are two pivotal factors influencing ESCR [3], [15]. For instance, high-density PE (HDPE) typically exhibits lower ESCR compared to branched polyethylene polymers (BPE) like low-density PE (LDPE) or linear low-density PE (LLDPE) containing short-chain branches (SCBs) [47]. Moreover, ESCR tends to be higher in LLDPE with butyl branches compared to LLDPE with ethyl branches [15], [16], as illustrated in Figure 4 which represents the structure of SCBs. Shirkavand *et al.* [48] concurred with these findings, reporting that increasing the number of branches in a polymer, thus reducing its degree of crystallinity, enhancing ESCR. Cheng *et al.* [38] supported this notion, suggesting that polymers with more SCBs exhibit better ESCR due to increased sliding resistance of chains with longer SCBs, a greater number of tie-molecules in the amorphous regions, and lower crystallinity. Yeh *et al.* [49] further demonstrated that PE's ESCR significantly improves

as the branch length increases from 2 to 6 carbons. Additionally, Bubeck *et al.* [45] explored the impact of the quantity and length of SCBs on PE's ESCR, concluding that an increased presence of longer SCBs enhances ESCR. Meanwhile, Sardashti *et al.* [44] investigated the effect of crystallinity on ESCR in both HDPE and LLDPE. Their results indicated that a higher degree of crystallinity reduces ESCR in both types of PE, with a more pronounced effect observed in HDPE compared to LLDPE, as shown in Figure 5. This result signifies that the presence of amorphous structure of polymer is crucial to improve the resistance of PE polymers regarding ESC.

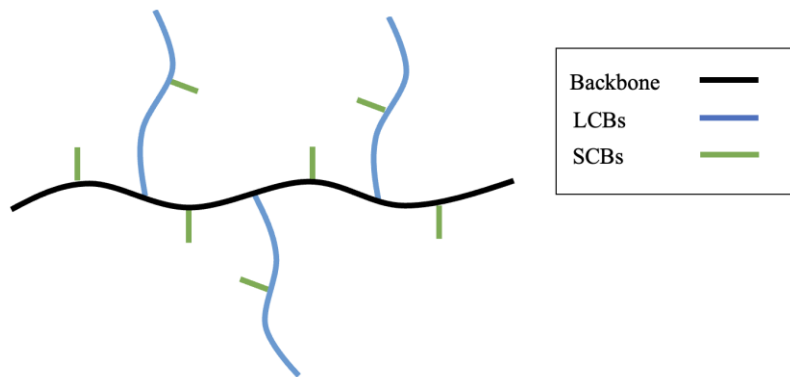


**Figure 4.** Type of branches in polyethylene structure.

Ward *et al.* [46] delved into the behavior of PE specimens exposed to various ESC agents, stress levels, and temperatures, with their findings represented in Figure 6, where, they determined that by increasing the temperature and stress, the time to failure of the PE specimens reduced.

Their study unveiled that ESC agents effectively plasticize the amorphous phase within PE. This plasticization, in turn, fosters crack propagation and accelerates the brittle fracturing of the crystalline phase. They pinpointed the disentanglement of tie molecules as the fundamental reason behind ESC. Importantly, the density of these tie molecules in the amorphous region, a factor primarily regulated by the presence of branches, plays a pivotal role in governing polymer chain disentanglement. Garcia *et al.* [50] extended these insights, highlighting that aside from tie molecules, other inter-lamella links, such as chain entanglements, contribute to the enhancement of ESCR in PE. Collectively, these findings underscore the pivotal role of the amorphous phase's quantity and structure within PE in relation to ESCR. Qian *et al.* [51] explored the impact of ESC agents on slow crack growth (SCG) across various PE samples, varying the concentrations of Igepal as the ESC agent. Their investigations revealed a notable trend: within the concentration range of 0 to 0.1%, the most significant reduction in time to failure occurred, with the minimum time to failure transpiring at approximately a 50% Igepal concentration, as illustrated in Figure 7. Intriguingly, they observed a substantial increase in time to failure when the concentration surged from 50% to 100%. Concerning the influence of the ESC agent and its concentration, Figure 8 presents scanning electron microscope (SEM) images, offering a visual depiction of how varying Igepal concentrations affect a PE sample's texture and its fractured structure. This figure demonstrates that by increasing the concentration of ESC agent, the amount of cavities inside the PE structure severely increases.

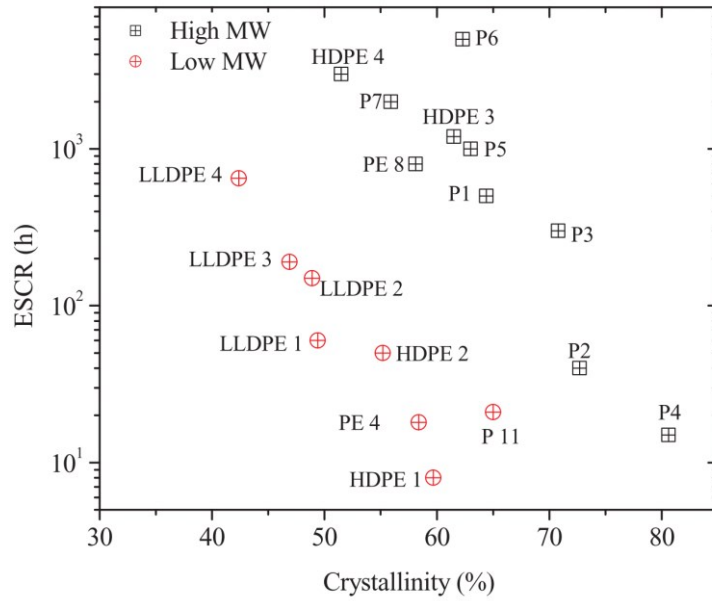


Figure 5. ESCR versus percentage crystallinity [44].

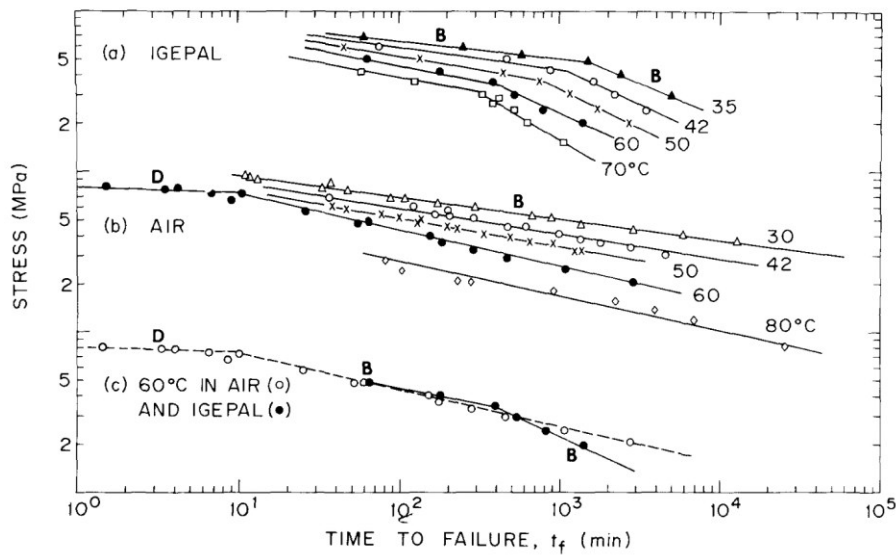
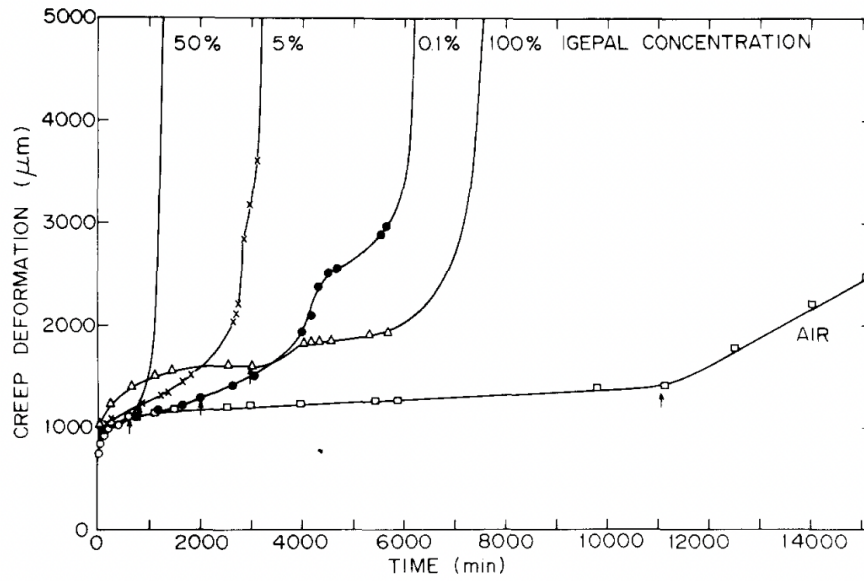
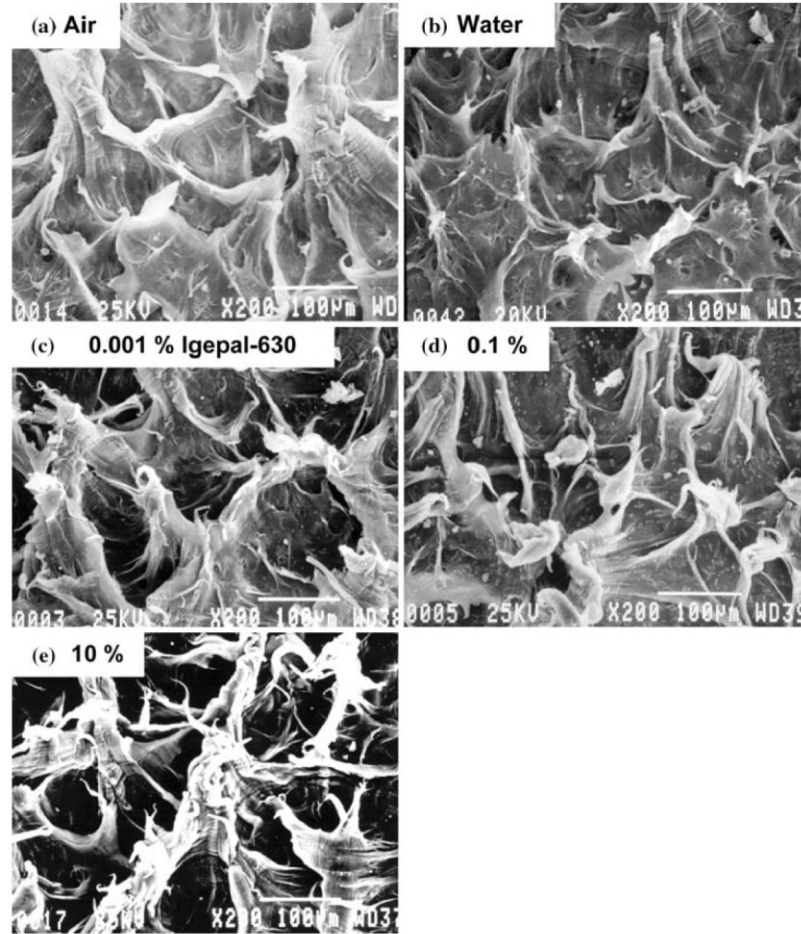


Figure 6. Stress versus time to failure at various temperatures; (a), (b) and (c) have a common y axis. D designates a ductile region and B designates a brittle region. (a) In Igepal, (b) in air, (c) in air and Igepal at 60°C [46].



**Figure 7.** Creep deformation versus time for a PE sample (at 50°C, 2 MPa) for various concentrations of Igepal as ESC agent [51].



**Figure 8.** SEM images from the fracture surfaces of a PE sample, showing the effect of Igepal-630 concentration [52].

Considering the inherent brittleness of PE in ESC failure and the empirical observation of cavitation during the initial stages of crack formation, we propose a hypothesis. Our hypothesis is that cavitation within the amorphous phase of PE may originate from the coalescence of free volume holes when an ESC agent is present. This hypothesis rests on the premise that an increased activity of free volume coalescent leads to cavitation, when the polymer experiences internal or external stresses. It is worth noting that a reduced degree of crystallinity, signifying a higher

proportion of the amorphous phase, diminishes the probability of these free volume holes merging. Crucially, the dimensions of these free volume holes may be influenced by factors such as the nature and concentration of the ESC agent, as well as the specific structural attributes of the PE material. Consequently, our research endeavors to scrutinize whether the introduction of an ESC agent, in this instance, nonyl ethoxylate (NE), at various concentrations below its critical micelle concentration, exerts an influence on the spatial arrangement of polymer chains within PE. Our investigation will particularly focus on PE samples with and without SCBs, employing molecular dynamics (MD) simulations as our investigative tool. We intend to quantify the packing arrangement by evaluating parameters such as the intermolecular radial distribution function and the distribution of free volume hole sizes.

## **1.2. Statement of problem**

Research has highlighted the significant role of ESC in contributing to polymer failures across various industries, accounting for approximately 25% of such failures [9]. ESC remains a substantial concern [53], [54], particularly in the realm of plastics, with a sustained focus on its impact on PE pipelines [54]–[57]. PE pipes represent the predominant and cost-effective solution [58] for transporting process water [59] and produced oil and gas mediums [1]. For instance, in the context of enhanced oil recovery (EOR), where methods like Alkaline–Surfactant–Polymer (ASP) have gained prominence and been endorsed by the Alberta government due to their successful outcomes [60]; ESC prevention is crucial. EOR alone has accounted for a significant portion of total U.S. oil production, as reported [61]. Given that Alberta's economy is significantly reliant on the oil industry, with 80% of Canada's crude oil and 67% of its natural gas originating

from this province [62], there is a pressing need to minimize PE polymer failures and devise innovative strategies to enhance pipeline resistance against ESC.

ESC poses a substantial challenge for the widespread use of PE pipes, which find extensive applications in the oil and gas sector and water distribution networks. Over the past decades, ESC has persistently loomed as a significant concern within the industry. Numerous research teams and laboratories have diligently worked towards minimizing the susceptibility of PE samples to ESC, with the overarching goal of prolonging the lifespan of PE materials, especially in critical applications like pipelines. The potential savings in costs associated with ESC mitigation are substantial. This phenomenon is rooted in the belief that cavitation, the first step of ESC, and a precursor to crack formation, originates within the amorphous phase of PE.

### **1.3. Objective**

The primary aim of the present project is to investigate the molecular understanding underlying the phenomenon of ESC in PE. Our objective is to investigate the causations behind ESC of PE by molecular simulations, introducing a novel perspective centered around the concept of "free volume". It is essential to underscore that despite the wealth of published results in the literature, the current comprehension of PE's ESC remains insufficient. Notably, the proposed molecular mechanisms explaining ESC failures, disentanglement of the PE chains, as put forth by various authors, have not been directly quantified through experiments. Remarkably, there exists no direct experimental evidence elucidating the mechanistic process of disentanglement, especially when multiple segments of the same tie molecule are anchored within the crystalline phase. It is

necessary to recognize that entanglement remains a qualitative concept, inherently immeasurable, and thus, the notion of disentanglement lacks empirical support.

#### **1.4. Proposed research**

In our proposed research, we intend to explore a novel hypothesis that elucidates the initiation of the cracks in PE and its subsequent brittle failure under ESC conditions. We posit that these phenomena are closely linked to the creation and coalescence of free volume regions surrounding the ESC agent. Given the inherent brittleness of PE in ESC failures and the experimental observation of cavitation during the initial stages of crack development, we hypothesize that cavitation within the amorphous phase of PE may arise due to the generation of larger and more extensive free volume holes when an ESC agent is present. Furthermore, we hypothesize that the coalescence of these free volume holes may be contingent on factors such as the nature and concentration of the ESC agent, as well as the specific structural attributes of the PE material. To put this hypothesis to the test, our study will investigate whether the introduction of an ESC agent, specifically nonyl ethoxylate (NE), at various concentrations, alters the free volume coalescence around itself, in the PE matrix both with and without SCBs. To assess our hypothesis, we will analyze the spatial distribution of free volume holes utilizing Voronoi tessellation techniques applied to molecular dynamics (MD) simulation data. Additionally, our research will delve into the dynamics of free volume coalescence around ESC agent during the simulation period, aiming to provide deeper insights into the free volume coalescence, with the goal of finding ESC mechanisms.

## 1.5. Research outline

**Chapter 2** details the molecular simulation methodology, which includes details of the MD method, all-atom (AA) forcefields, radial distribution function (RDF), and potential of mean force.

**Chapter 3** explores the impact of an ESC agent on the free volume coalescence, i.e., cavitation initiation process, in linear polyethylene (LPE) and branched polyethylene (BPE). The investigation focused on assessing the size and spatial distribution of free volume voids at the interfaces between PE and the ESC agent. The BPE models under scrutiny featured two variations, one with 10 and the other with 82 butyl/hexyl branches per 1,000 backbone carbons. The chosen ESC agent was nonyl ethoxylate (NE), examined at concentrations ranging from 0.001 to 1.4 wt%.

**Chapter 4** to investigate the distribution and coalescence of free volume around ESC agent, NE at a concentration of 0.5 wt% within a set of PE blends. These blends included LPE and BPE, where there are two variations of BPE, one with 10 hexyl branches and the other with 82 hexyl branches per 1,000 backbone carbons. Additionally, a small four-arm small alkane known as 7,12 hexyl octadecane (SA) was part of the study, featuring four hexyl branches attached to a backbone containing only four carbons.

**Chapter 5** investigates free volume coalescence in PE is influenced by vinyl acetate (VA) groups, using MD simulations. Previous researches have shown that functionalized PEs with VA could increase the ESCR of PE, and the main focus of this part of the research is to investigate how VAs could affect free volume coalescence around NE.

**Chapter 7** provides the overall conclusion of the thesis and potential future work.

**Chapter 8** represents the bibliography of the thesis.

# Chapter 2: Molecular Simulation Methodology

---

## 2.1. Molecular Dynamics (MD)

To explore how PE interacts with the ESC agent, namely NE, we have employed MD simulation tool. Molecular simulation approaches can be broadly classified into two primary categories: *i*) deterministic and *ii*) stochastic. In contrast to stochastic methods like Monte Carlo (MC), MD stands out as a deterministic molecular simulation technique. It accomplishes this determinism by utilizing equations of motion to compute the forces, velocities, and coordinates of individual particles within a simulation box throughout the simulation period.

MD simulations address Newton's equations of motion for a system comprising  $N$  interacting atoms [63]:

$$m_i \frac{\partial^2 r_i}{\partial t^2} = \mathbf{F}_i, \quad i = 1, \dots, N \quad (2-1)$$

Here,  $\mathbf{F}_i$  is the force acting on a particle  $i$ , at position  $r_i$ , at time  $t$ , with the mass of  $m_i$ . The force  $\mathbf{F}_i$  on a particle is negative derivation of the potential energy  $U(r^N)$ , where  $r^N = (r_1, r_2, r_3, \dots, r_N)$ :

$$\mathbf{F}_i = -\frac{\partial U(r^N)}{\partial r_i} \quad (2-2)$$

The equations are concurrently solved in small time increments. The system is monitored over a period while ensuring that temperature and pressure are maintained at their specified values. At regular intervals, the particle coordinates are recorded in an output file. These coordinates, recorded over time, create a *trajectory* that describes the system's behavior. Typically, after an initial period, the system reaches an *equilibrium state*. Averaging over this equilibrium trajectory allows for the extraction of various macroscopic properties from the output file. Figure 9 represents the global MD algorithm.

Although during the past decades the MD simulations has introduced very promising results, however, this way of representing real systems and molecular structures has its own limitation, such as:

- Applying Newton's equations of motion inherently involves utilizing classical mechanics to characterize atom movements. While this approach is suitable for most atoms under typical temperatures, there are exceptions. Hydrogen atoms, due to their lightweight nature, and proton motion occasionally exhibit essential quantum mechanical traits.
- In MD, the employed conservative force field is solely dependent on the atom positions. Consequently, electronic motions are not explicitly accounted for. In this approach, it is

assumed that electrons instantly adapt their dynamics when atomic positions change and remain in their ground state. This approximation is generally suitable for most cases. However, it cannot handle processes involving electron transfer or electronically excited states. Furthermore, MD isn't well-suited for accurately simulating chemical reactions.

- All non-bonded forces are a result of summing non-bonded pair interactions. Interactions that aren't pair-additive, with atomic polarizability being a significant example, are represented through effective pair potentials. Only average contributions from non-pair-additive interactions are integrated. Consequently, pair interactions aren't purely accurate, as they may not hold for isolated pairs or significantly differing scenarios from the ones used to parameterize the models.
- Long range interactions mostly are cut-off, where a cut-off radius is always applied for Lennard-Jones interactions and sometimes for Coulomb interactions too. For example, GROMACS (the MD tool we have used) follows the "minimum-image convention," which means that for pair interactions, only one image of each particle in the periodic boundary conditions is considered.[64] Therefore, the cut-off radius cannot exceed half the size of the simulation box. While this is generally sufficient for large systems, issues can arise in systems containing charged particles. In such cases, problems like charge accumulation at the cut-off boundary or significant energy inaccuracies can occur. For these systems, it's advisable to consider using one of the implemented long-range electrostatic algorithms, such as particle-mesh Ewald.[65]

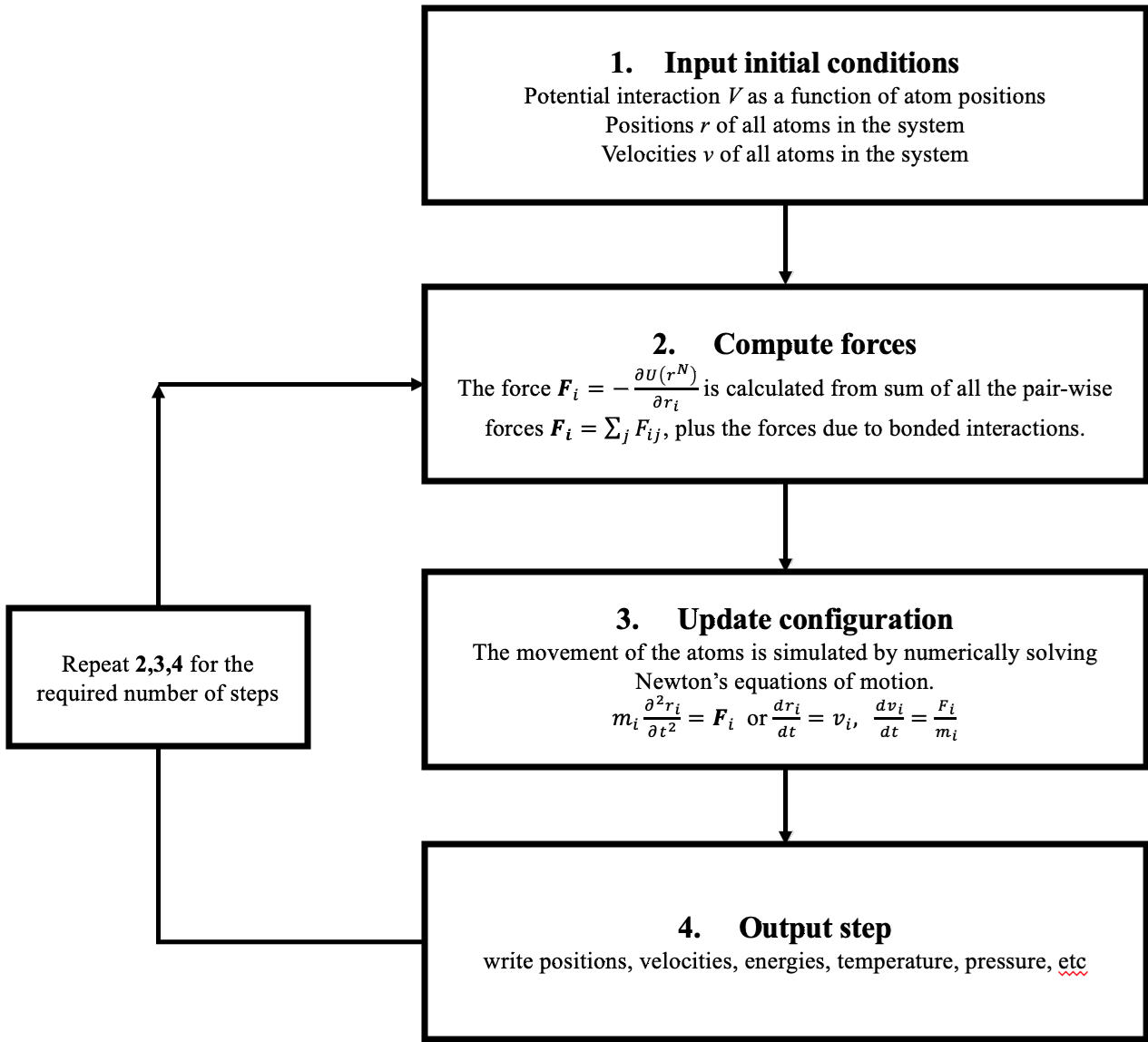


Figure 9. The global MD algorithm [64].

### 2.1.1. The leap-frog algorithm: MD integrator

The leap-frog algorithm is a commonly used numerical integration method in MD simulations for solving the equations of motion for particles in a system over discrete time steps [66]. The leap-frog algorithm is:

1. Initialization: The initial positions and velocities of all particles in the system are known.
2. First Half-Step (Kick): The velocities of all particles are updated by half of a time step ( $\Delta t/2$ ) using the forces acting on them. This step is sometimes called the *kick*.  $\Delta t$  is the integration time step (simulation time step).

$$v\left(t + \frac{1}{2}\Delta t\right) = v\left(t - \frac{1}{2}\Delta t\right) + \frac{\Delta t}{m}\mathbf{F}(\mathbf{t}) \quad (2-3)$$

3. Full Step (Drift): The positions of all particles are updated by a full-time step ( $\Delta t$ ) using the updated velocities from the previous step. This is sometimes referred to as the *drift*.

$$r(t + \Delta t) = r(t) + \Delta t v\left(t + \frac{1}{2}\Delta t\right) \quad (2-4)$$

Figure 10 represents the leap-frog algorithm.

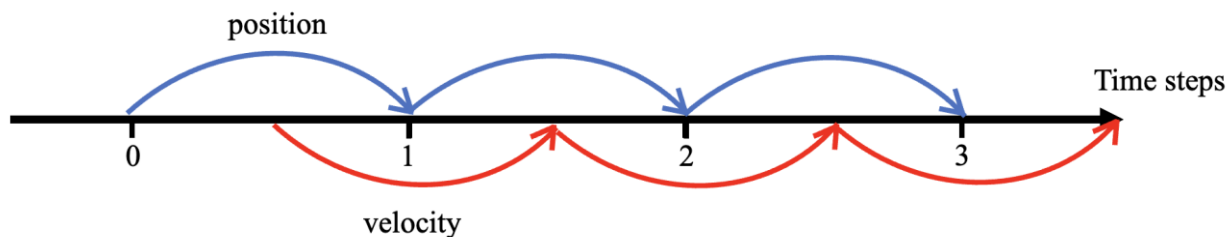


**Figure 10.** The leap-frog algorithm. It is so named because it involves positions  $r$  and velocities  $v$  leaping back and forth in a manner reminiscent of the movements of jumping frogs.

The Leap-Frog algorithm possesses several notable attributes. It is time-reversible and it conserves both energy and momentum. The conservation of energy and momentum is crucial in MD simulations because it ensures that the simulation accurately represents the physical behavior of the system over time, even as it undergoes various interactions and transformations. This property makes the Leap-Frog algorithm particularly valuable in simulations where these conservation principles are essential. Furthermore, it demands memory storage for  $6N$  real numbers linked to position and momentum.

There are other type of integrator in MD such as Verlet [67] and velocity Verlet algorithms [68]. The Velocity Verlet and Leap-Frog algorithms are both time-reversible, with the main difference being in how they update velocities. Velocity Verlet is slightly more accurate but computationally more expensive and will requires days to finish the calculations. Leap-Frog is simpler and more memory-efficient, making it a common choice for practical simulations where computational resources are limited [63]. The choice between them depends on the specific requirements and computational resources available for a given simulation.

### 2.1.2. Temperature coupling

Coupling temperature in MD simulations is a technique used to control and maintain the temperature of a simulated system. This temperature control is crucial for two main reasons:

- (i) **Thermodynamic Equilibrium:** In real-world experiments, systems are often held at a constant temperature, so MD simulations aim to replicate this condition.
- (ii) **Study of Thermodynamic Properties:** MD simulations are often used to calculate various thermodynamic properties of a system, such as specific heat capacity, diffusion coefficients, and phase transitions. Most of the quantities in MD simulations that are required to calculate are from canonical ensemble NVT and Isothermal–isobaric ensemble NPT, where temperature is fixed [69]

Common methods for temperature coupling in MD simulations include Berendsen [70], velocity rescaling [71] Nose-Hoover [72], [73] and the Andersen [74] thermostat. These methods work by adjusting the velocities of particles in the simulation to achieve and maintain the desired temperature. Velocity rescaling algorithm is a modified version of Berendsen algorithm and both of them provide a good stability for the simulated systems. The velocity rescaling algorithm has been used in this work. In the following sections, Berendsen and velocity rescaling algorithms will be explained.

#### 2.1.2.1 Berendsen thermostat

The Berendsen algorithm emulates a weak connection to an external heat reservoir set at a specified temperature  $T_0$ , using a first-order kinetic approach. This algorithm works by gradually

correcting any deviation of the system temperature from the initial value,  $T_0$ , where a temperature deviation decays exponentially with a time constant  $\tau$ .

$$\frac{dT}{dt} = \frac{T_0 - T}{\tau_T} \quad (2-5)$$

The heat exchange between the system and its surroundings is managed by adjusting the velocities of individual particles either at every step or every  $n_{TC}$  steps. This adjustment is performed using a time-dependent scaling factor, denoted as  $\lambda$ , which is determined by the following equation:

$$\lambda = \left[ 1 + \frac{n_{TC}\Delta t}{\tau_T} \left\{ \frac{T_0}{T(t - \frac{1}{2}\Delta t)} - 1 \right\} \right]^{1/2} \quad (2-6)$$

Where  $\tau$  is related to  $\tau_T$  by the following equation:

$$\tau = \frac{2C_v\tau_T}{N_{df}k_B} \quad (2-7)$$

Here,  $C_v$  is the total heat capacity of the system,  $k_B$  is Boltzmann's constant, and  $N_{df}$  is the total number of degrees of freedom.

### 2.1.2.2 Velocity rescaling thermostat

The velocity-rescaling thermostat [71] is essentially similar to the Berendsen thermostat but it incorporates an extra stochastic component. This component is introduced to accurately adjust the kinetic energy distribution and is achieved by modifying it in accordance with Eq. (2-8)

$$dK = (K_0 - K) \frac{dt}{\tau_T} + 2 \sqrt{\frac{KK_0}{N_{df}}} \frac{dW}{\sqrt{\tau_T}} \quad (2-8)$$

where  $K$  is the kinetic energy and  $dW$  a Wiener noise. Without the stochastic term this equation reduces to that of the standard thermostat of Berendsen. The selection of stochastic has some degree of arbitrariness, with the sole requirement being that it maintains the invariance of the canonical distribution [71].

### 2.1.3. Pressure coupling

Similar to temperature coupling, in the pressure coupling methods, the simulation box could be coupled to a pressure bath. There are different type of pressure coupling methods such as Berendsen, Parrinello-Rahman [75] and Martyna-Tuckerman-Tobias-Klein (MTTK) [76]. Parrinello-Rahman and Berendsen can be combined with any of the temperature coupling methods; however MTTK can only be used with Noose-Hoover temperature control. In this work, we have used Parrinello-Rahman. The Parrinello-Rahman barostat allows for isobaric MD simulations with better accuracy. Similar to Andersen barostat [74], it uses a piston to control pressure, however, the Parrinello-Rahman approach is a generalization of that of Andersen in two ways, 1) Instead of expressing the fractional coordinates in relation to Cartesian coordinates using volume, the relationship is provided in a more comprehensive form (as shown in Eq. (2-9)). Therefore, the simulation cell's shape could be any shape. 2) In the Lagrangian equation (Eq. (2-12)), the kinetic energy of the barostat is described in terms of the rate of change of the components of the h-matrix over time, rather than solely in terms of volume.

In Parrinello-Rahman approach, if box vectors are  $\mathbf{a}$ ,  $\mathbf{b}$  and  $\mathbf{c}$ , by having the box matrix  $\mathbf{h} = \{\mathbf{a}, \mathbf{b}, \mathbf{c}\}$  in a  $3 \times 3$  matrix. The volume  $V$  of the box would be:

$$V = \det(\mathbf{h}) = \mathbf{a} \cdot (\mathbf{b} \times \mathbf{c}) \quad (2-9)$$

The position  $\mathbf{r}_i$  of a particle can be written in terms of  $\mathbf{h}$  and a column vector  $s_i$ , with components  $\xi_i$ ,  $\eta_i$  and  $\zeta_i$  as:

$$\mathbf{r}_i = \mathbf{h}s_i = \xi_i \mathbf{a} + \eta_i \mathbf{b} + \zeta_i \mathbf{c} \quad (2-10)$$

Where,  $0 \leq \xi_i, \eta_i, \zeta_i \leq 1$ . The square of the distance between particle  $i$  and  $j$  is given by:

$$r_{ij}^2 = s_{ij}^T \mathbf{G} s_{ij} \quad (2-11)$$

Here,  $\mathbf{G} = \mathbf{h}^T \mathbf{h}$ , is a matrix tensor. By considering the above notations, the Lagrangian of the *system + piston* would be [75], [77]:

$$\mathcal{L} = \frac{1}{2} \sum m_i \dot{s}_i^T \mathbf{G} \dot{s}_i - \sum \sum U(r_{ij}) + \frac{1}{2} M \text{Tr}(\dot{\mathbf{h}}^T \dot{\mathbf{h}}) - pV \quad (2-12)$$

By obtaining the equation of motion from the above equation, the box vectors as represented by the matrix  $\mathbf{h}$  obey the matrix equation of motion [75]:

$$W \frac{d^2 \mathbf{h}}{dt^2} = V \mathbf{h}^T \mathbf{h}^{-1} (P - P_{ref}) \quad (2-13)$$

Where  $W$  is a matrix parameter that determines the strength of the coupling, and it is related to isothermal compressibility  $\beta$  and the pressure time constant  $\tau_p$  in the input file ( $L$  is the largest box matrix element):

$$(W^{-1})_{ij} = \frac{4\pi^2\beta_{ij}}{3\tau_p^2L} \quad (2-14)$$

#### 2.1.4. Forcefield

In molecular simulation, a force field (FF) is a mathematical model that describes the interactions between atoms and molecules in a system. It's a set of equations and parameters used to calculate the forces and energies associated with various interactions, such as bonded interactions (like covalent bonds), non-bonded interactions (like van der Waals forces and electrostatic interactions), and often, dihedral or torsional angles in molecules [78]. These force fields provide a way to predict how molecules will move and interact over time. They play a crucial role in MD simulations by determining the forces acting on each atom, which in turn govern the motion and behavior of the simulated system [79]. Eq. (2-15), represents a typical potential energy that would

be used to calculate the forces, from  $\mathbf{F}_i = -\frac{\partial U(r^N)}{\partial r_i}$ .

$$\begin{aligned}
U(r^N) = & \frac{1}{2} \sum_{bonds} k_b (r_{ij} - r_0)^2 + \frac{1}{2} \sum_{angles} k_\theta (\theta_{ijk} - \theta_0)^2 \\
& + \frac{1}{2} \sum_{torsions} k_\phi (1 + \cos m\phi_{ijkl} - \gamma) \\
& + \sum_{i=1}^N \sum_{j=i+1}^N \left( 4\varepsilon_{ij} \left\{ \left( \frac{\sigma_{ij}}{r_{ij}} \right)^{12} - \left( \frac{\sigma_{ij}}{r_{ij}} \right)^6 \right\} + \frac{q_i q_j}{4\pi\epsilon_0 r_{ij}} \right) \quad (2-15)
\end{aligned}$$

Here,  $U(r^N)$  is the potential energy of the particle;  $k_b$ ,  $k_\theta$  and  $k_\phi$  are bond, angle and dihedral force constants, respectively.  $r_0$  and  $\theta_0$  are equilibrium values for bond and angle, respectively. The depth of non-bonded potential is  $\varepsilon_{ij}$ ,  $\sigma_{ij}$  is the size of two interacting particles with distance  $r_{ij}$ . [80] Also,  $q_i$  and  $\epsilon_0$  are particle charge and dielectric constant of the medium. All of the force parameters for interacting particles are stored in FFs.

There are different type of FFs such as: *i*) all-atoms (CHARMM22 [81] and OPLS [82], [83]), where all of the atoms in the simulation box will consider explicitly, *ii*) united atom (CHARMM19[84], GROMOS [85], [86] and TraPPE [87], [88]), where implicit representation of aliphatic and aromatic hydrogen atoms are achieved by grouping the carbon atom along with its attached hydrogen atoms into a single particle centered on the carbon atom, and *iii*) coarse grained (such as MARTINI [89], [90]), in which they apply a mapping of few heavy atoms into one coarse-grained (CG) interaction site (for example in MARTINI, three to four atoms into one bead) and is parametrized with the aim of reproducing thermodynamic properties.

### 2.1.4.1 Cut-off

In MD simulations, a cut-off is a predefined distance beyond which interactions between particles are considered to be negligible and are effectively truncated [91], [92]. This concept is primarily used to simplify calculations and reduce computational resources in MD simulations, which model the motion and interactions of atoms and molecules over time [91]. Specifically, cut-off is often applied to non-bonded interactions, such as van der Waals forces and long-range electrostatic interactions (e.g., Coulombic forces) [93].

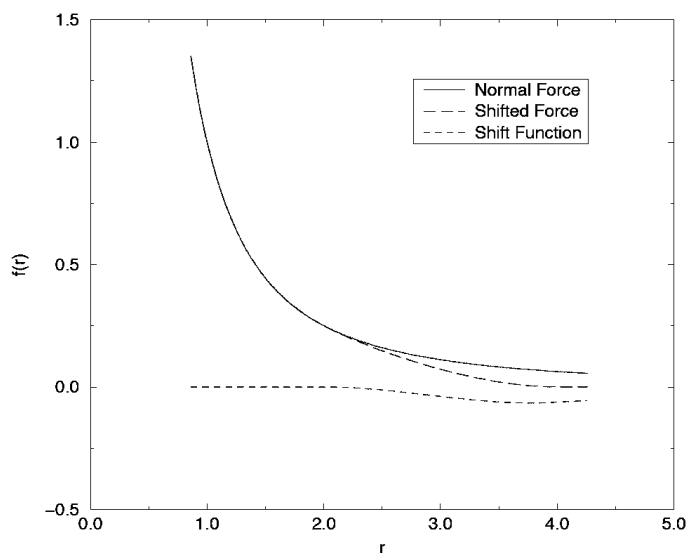


**Figure 11.** The Coulomb Force, Shifted Force and Shift Function as a function of distance from the distance from a given particle [64].

For van der Waals interactions (second last term in Eq. (2-15)) atoms and molecules experience van der Waals forces, which are attractive forces that arise due to fluctuations in electron density. A cut-off for van der Waals interactions means that beyond a certain distance, the

potential energy is set to zero, and the forces are not computed. This simplifies calculations because the van der Waals potential drops off rapidly with distance. For Coulombic interactions (last term in Eq. (2-15)), since they can be computationally expensive to calculate directly in large systems, cut-offs are applied, and interactions beyond the cut-offs distance are ignored. Various methods, like using shifted function (Figure 11) Ewald summation or particle mesh Ewald [65], are used to account for long-range electrostatics accurately. While cut-offs significantly speed up MD simulations, they can introduce artifacts and inaccuracies, particularly for properties influenced by long-range interactions.

In this work, the Transferable Potentials for Phase Equilibria (TraPPE) force field was used to describe the bonded and non-bonded interactions between the atoms and/or united atoms in the systems. The TraPPE force field has been demonstrated to be accurately describing the interatomic potentials for linear and branched alkanes, alcohols, ethers, ketones, and aldehydes, PE and its different structures [94], [95].

#### **2.1.5. Radial distribution function**

The Radial Distribution Function (RDF), also known as the pair distribution function or  $g(r)$ , is a mathematical function used extensively in the field of molecular simulation, particularly in MD and MC simulations [96], [97]. RDF provides essential information about the local structure and arrangement of particles within a system. It gives insights into how atoms or molecules are distributed around a reference particle, helping to understand the material's density, packing, and organization [98], [99].

$$g(r) = C \frac{\int \delta(r'_1 - r_1) \delta(r'_2 - r_2) e^{\frac{\epsilon(r', p')}{k_B T}} dr' dp'}{\int e^{\frac{\epsilon(r', p')}{k_B T}} dr' dp'} \quad (2-16)$$

Where,  $r_1$  and  $r_2$  are the positions of two particles,  $\delta(\cdot)$  is Dirac's delta function,  $C$  is a constant number and  $\epsilon$  is the energy associated to the given phase space state. In a simpler form, Eq. (2-16)) would be written as:

$$g(r) = \frac{V}{4\pi r^2} \sum_{i \in A}^{N_A} \sum_{j \in B}^{N_B} P(r) \quad (2-17)$$

Where  $V$  is the volume and  $P(r)$  is the probability of finding a particle  $B$  at distance  $r$  from a particle  $A$ . The RDF ( $g(r)$  in Eq. (2-16)) quantifies the probability of finding a particle at a certain distance from a reference particle. In other words, it describes how the density of particles varies as a function of distance from a central particle [100]. The RDF is typically normalized so that it equals 1 when the particles are randomly distributed, which serves as a reference state [101]. This means that values of the RDF greater than 1 indicate a higher probability of finding particles at a specific distance compared to a random distribution, while values less than 1 indicate a lower probability [102]. Peaks in the RDF correspond to characteristic distances between particles in the system. For example, in a liquid, the first peak often corresponds to the average distance between nearest neighbor particles, while subsequent peaks may represent larger-scale arrangements.

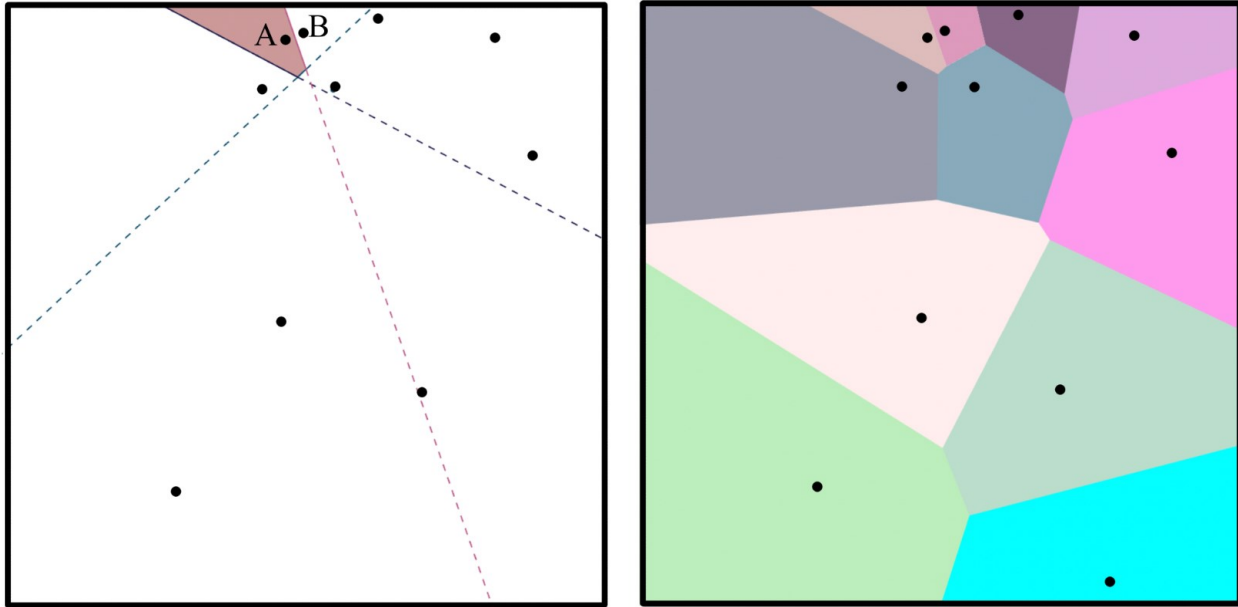


**Figure 12.** Voronoi tessellation method in 2D space. The right picture represents a half-plane in-between two particles A and B.

#### *2.1.5.1 Time average and ergodicity*

Ergodicity is a concept commonly used in statistical mechanics and thermodynamics. It refers to the idea that, over a sufficiently long time, a system's time-average behavior will be representative of its ensemble-average behavior [103]. In simpler terms, it implies that if you observe a system for a long enough duration, the statistical properties you measure will converge to the same values that you would obtain by averaging over all possible states of the system. Ergodicity suggests that you can understand a system's behavior by observing it over time and averaging the observations, rather than needing to sample all possible configurations of the system [77]. Time averages involve observing one system over time, while ensemble averages involve considering many identical systems simultaneously. Ergodicity implies that these averages are

equivalent for an ergodic system. Ergodicity is not universally true for all systems. It applies to systems that explore their phase space (the set of all possible states) thoroughly over time. Some systems may not be ergodic, especially if they are trapped in certain states or have constraints that limit their exploration of phase space. In this thesis, we have assumed that the system we are investigating are ergodic systems, so for some analysis such as RDF, we have used the time average of the RDF over last nanoseconds of the simulations.

## 2.2. Voronoi tessellation

Voronoi tessellation (VT), also known as Dirichlet or Thiessen polygons [104], is a method that can be used to partition a space into regions close to each set of dots (in our case, particles). In general, VT calculates the distance between every two particles and draws a half-plane in between them, then calculates the associated volume for each particle [105], [106]. In this work, in order to compute the Voronoi cells, the `pyvoro` python package[107] has been used. The `pyvoro` package is based on `voro++` library[108]–[110]. `voro++` is an open-source software library designed for calculating the Voronoi diagram, efficiently computes the Voronoi cells directly. Figure 12 represents VT method for a 2D plane. The schematic of the utilized VT algorithm is represented in Figure 13 [111]. The Voronoi cell obtained by this algorithm, will be approximately a sphere with radius  $R/2$ , with many facets due to the particles in the shell. As  $R$  increases, the number of facets will increase without limit. After having the cell volume, the volume space assigned to each particle at every timestep can be calculated by reducing the hard-core (HC) volume of each particle from the calculated volume, one could evaluate the free volume assigned to every particle through:

$$V_{free} = V_{cell} - V_{hc} \quad (2-18)$$

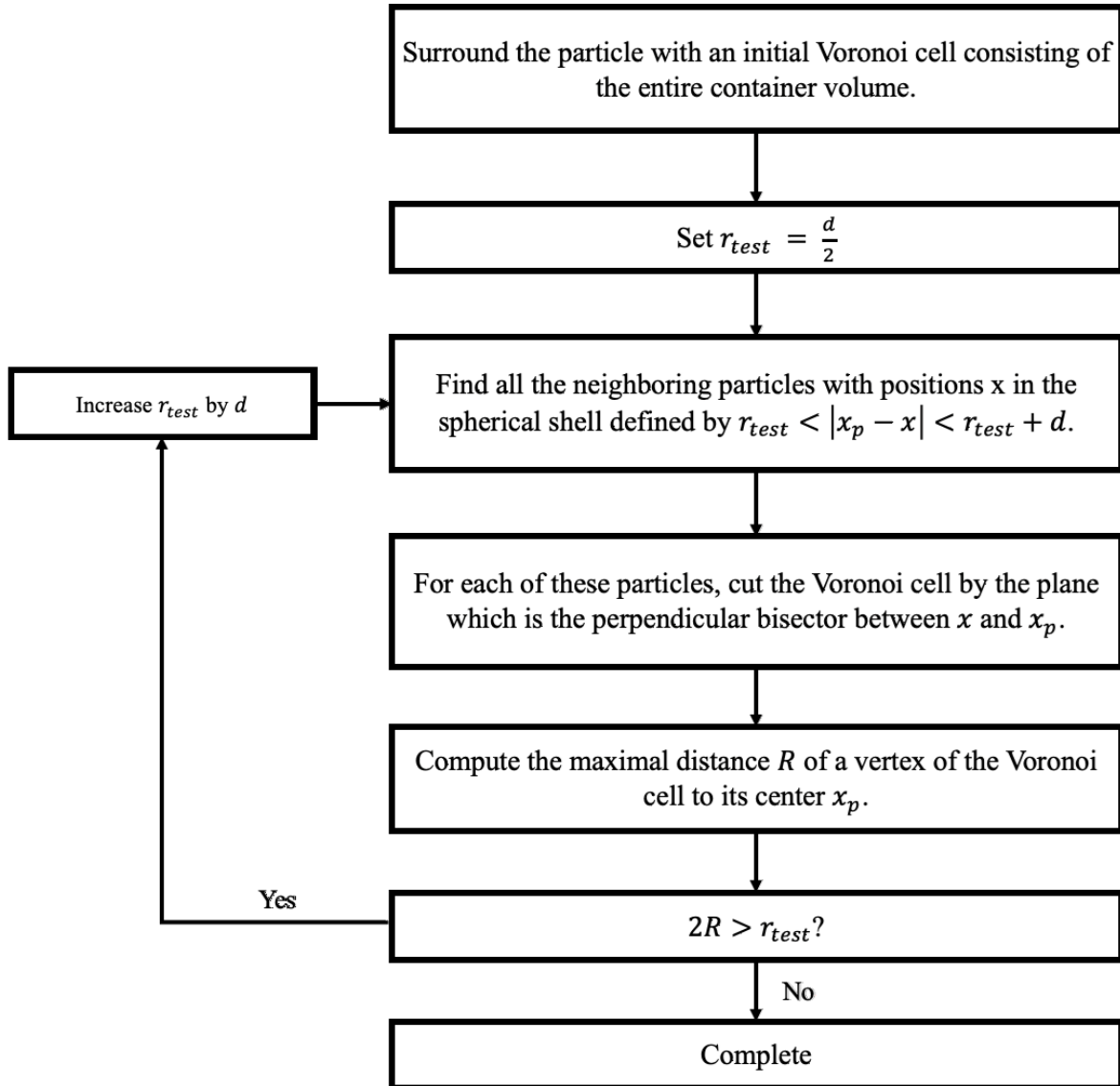


**Figure 13.** The algorithm of VT for particles with particle diameter  $d$ , radial separation  $R$  and position of  $x_p$ .

Where  $V_{free}$ ,  $V_{cell}$  and  $V_{hc}$  are the free volume, cell volume calculated by VT and hard-core (HC) volume of each particle, respectively. By calculating the free volume of each particle, then we could provide a probability distribution for the free volume of different molecules in the simulation box [112]. As an example, Figure 14 provides a probability distribution for a LPE polymer chain with 500 carbon atoms.

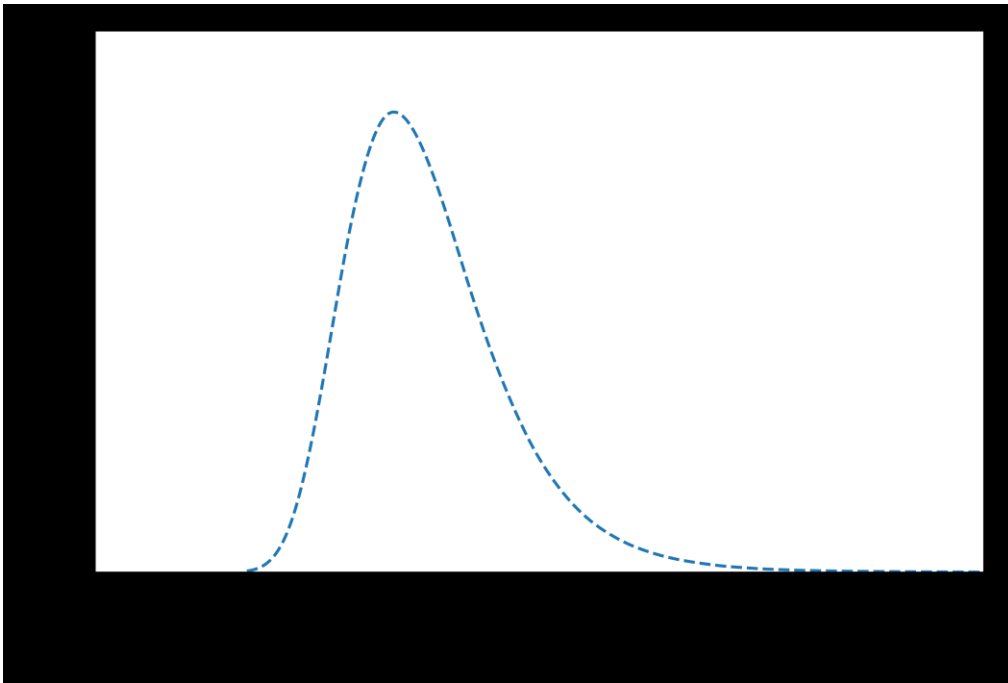


**Figure 14.** Probability distribution of free volume along LPE with 500 carbon atoms.

# Chapter 3: Free Volume Coalescence in

## Branched and Linear PE

\*Version of this chapter's sections has been published in: Kavyani S., and Choi P., Molecular dynamics study of the environmental stress cracking agent assisted cavitation in linear and branched polyethylene. *Polymer*, 2023, 264,125542.

---

### 3.1. Introduction

ESC is an old problem in polymer science [53], [113] but it is still relevant today as it is the major cause for 25 to 40% of polymer failures [114], [115]. ESC occurs to both amorphous and semi-crystalline polymers. In ESC, cracks form prematurely in the presence of inherent stress with the presence of an ESC agent, which is normally a surface-active substance, in the polymer. The cracks undergo SCG and eventually the polymer fails in a brittle fracture mode [115]. ESC is a significant problem in PE pipes that are used extensively in the oil and gas industry and water distribution systems [1].

The brittle failure of PE in ESC is somewhat unexpected as PE is a tough, semi-crystalline polymer. It is believed that cavitation (a precursor to the formation of cracks) is initiated in the amorphous phase of PE as a result of the disentanglement of the tie molecules and/or amorphous

chains followed by a brittle failure [3], [5], [6]. It is interesting to note that cavitation is a common feature of brittle failure in plastics. ESCR of a polymer signifies its ability to resist the SCG within its designed service life [7] – [9]. Indeed, ESCR has been a key consideration for the PE pipe design over the past few decades.

The PE characteristics that determine its ESCR are molecular weight averages, molecular weight distribution [10], [11], degree of crystallinity [44], degree of branching [45], and ease of diffusion of the ESC agent in the PE amorphous phase [46]. However, over the years, researchers have identified that the degree of branching and the degree of crystallinity are the two key attributes that determine ESCR [3], [15]. For example, HDPE exhibits lower ESCR than branched polyethylene such as LDPE or LLDPE that contains SCBs [47]. And the ESCR of LLDPE with butyl branches is generally higher than that of LLDPE with ethyl branches [15], [16]. Shirkavand *et al.* [48] reported similar findings that by increasing the number of branches in a polymer, thereby decreasing its degree of crystallinity, enhances its ESCR. Cheng *et al.* [38] also reported that PE with a higher number of SCBs exhibits higher ESCR. They suggested that the observation is due to the increasing sliding resistance of the chain with longer SCBs and increasing number of tie-molecules in the amorphous region and lower degree of crystallinity. Yeh *et al.* [49] also demonstrated that the ESCR of PE significantly increases when the branch length is increased from 2 to 6 carbons. Bubeck *et al.* [45] studied the influence of the number and length of SCBs on the ESCR of PE and found that the presence of more and longer SCBs in PE increases its ESCR. Sardashti *et al.* [44] studied the effect of crystallinity of PE on its ESCR for HDPE and LLDPE. Their results showed that increasing degree of crystallinity in PEs, for both LLDPE and HDPE,

the ESCR is reduced. However, they observed that crystallinity has a more significant effect on HDPE, compared to LLDPE.

Ward *et al.* [46] found that an ESC agent plasticizes the amorphous phase of PE, thereby promoting the crack growth and intensifying the brittle fracture of the crystalline phase. They mentioned that disentanglement of the tie molecules is the reason for ESC, where the most important factor that controls the disentanglement of the polymer chains are the density of the tie molecules in the amorphous region which is in turn controlled by the number of branches. Garcia *et al.* [50] found that in addition to the tie molecules, other inter-lamella links such as the chain entanglements help improve the ESCR of PE. All of the above findings point to the direction that ESCR is related to the amount and the structure of amorphous phase in PE.

It is important to emphasize that the molecular mechanisms for the ESC failure proposed by various authors are not determined directly from experiments that follow the motion of the macromolecules involved. In fact, there exists no direct experimental evidence for showing how disentanglement takes place mechanistically where two or more segments of the same tie molecule are anchored in the crystalline phase. In fact, entanglement is not a quantitative concept and it is not measurable, let alone disentanglement.

Given that PE fails brittlely in ESC and that cavitation is experimentally observed in the initial step of crack formation, we hypothesize that cavitation in the amorphous phase of PE originates from the formation of possibly more and larger free volume holes when an ESC agent is present. It is believed that having more and larger free volume holes increases the chance of free volume holes coalescence (cavitation) when the polymer is subject to internal/external stress.

Obviously, low degree of crystallinity (i.e., more amorphous phase) lowers the chance of the free volume holes coalescence. It is conceivable that free volume hole sizes depend on the nature and concentration of the ESC agent as well as the PE structure. Therefore, in this work, we will examine whether an ESC agent would alter the chain packings of PE with and without SCBs in the presence of an ESC agent nonyl ethoxylate (NE) at various concentrations below its critical micelle concentration using MD simulation. The packings will be quantified by the intermolecular radial distribution function and free volume hole size and spatial distributions.

### **3.2. MD Simulation**

Molecular dynamics simulations were carried out using GROMACS 2020.4 software package [27 - 28]. The TraPPE force field was used to describe the bonded and non-bonded interactions between the atoms and/or united atoms in the systems. The TraPPE force field has been demonstrated to be accurately describing the inter-atomic potentials for linear and branched alkanes, alcohols, ethers, ketones, and aldehydes, PE and its different structures [94], [95]. Since the main interest of the present work is on the molecular morphology of the amorphous phase of PE with and without an ESC agent, we simulated the systems at 190 °C, a temperature significantly above the melting point of PE to ensure the equilibration of the amorphous phase of the systems [119]. We believe that similar amorphous molecular morphology exists at low temperatures. However, the equilibration would take much longer time to achieve at room temperature that is not achievable in simulation, due to very slow movement of polymer chains at room temperature.

A modified Berendsen thermostat was used to control the temperature [120]. Pressure of the models were kept constant at 1 *bar* using the Parrinello-Rahman barostat [75]. All simulation

boxes were set to  $\sim 14 \times 14 \times 14 \text{ nm}^3$  initially. The periodic boundary conditions were used in  $x$ ,  $y$  and  $z$  directions. In the pure PE simulation unit cells (no ESC agent), according to TraPPE force field, all point charges were set to zero, and the single range cut-off method was used for calculating electrostatic interactions [117]. However, Particle Mesh Ewald (PME) method was used for systems with the ESC agent [65]. The time-step for the simulations was set to  $2 \text{ fs}$  and the neighbor searching updates every 5 steps. All twenty systems were run for about  $530 \text{ ns}$  of simulation time to ensure full equilibration. However, only the data of the last  $30 \text{ ns}$  of each trajectory were used for subsequent analysis.

We used two types of PE in this work – linear (LPE) and branched (BPE). Both types of PEs contained 500 carbons in their backbone. However, in the case of branched PE, it contained 5 and 41 butyl/hexyl branches. It is noteworthy that they correspond to branch contents of 10 and 82 SCBs/1,000 backbone carbons, respectively, and that commercial LLDPEs normally contain 10 – 20 SCBs/1,000 carbons. Figure 1 shows their molecular structures. Nonyl ethoxylate (NE) was used as the ESC agent. Here, nonyl phenol ethoxylate (NPE) is a common ESC agent [121], [122] and is known by its trade name *Igepal* [35], [123]. However, the TraPPE force field does not contain proper force field parameters for the phenol part of the molecule. Therefore, we decided to use an imitated structure NE instead of NPE in our simulations. Nonetheless, NE still contains the hydrophobic ethylene segments (E-segments) and hydrophilic ethylene oxide segments (EO-segments). Considering the goal of our study, we feel justified to use such imitated ESC agent. Figure 15 also shows the NE molecular structure used in this work. The details of all simulation systems are listed in Table 2. In the naming of the systems, the letter before PE denotes the molecular structure of the PE chain (linear or branched) which follows first, by the number of the

butyl(4)/hexyl(6) branches in the entire backbone (10 or 82). The number after NE denotes the number of it (i.e., concentration) used in the simulation unit cells. The corresponding weight fractions of NE are in the range of 0.001 ~ 1.4wt%.

**Table 2.** Descriptions of the Simulation Systems

System Name	PE Structure	Branch Type	Number of PE Molecules	Number of NE Molecules	Number of SCBs	Branch Content; SCBs/1,000
LPE	Linear	-	35	-	-	-
B4PE10	Branched	Butyl	35	-	5	10
B4PE82	Branched	Butyl	35	-	41	82
B6PE10	Branched	Hexyl	35	-	5	10
B6PE82	Branched	Hexyl	35	-	41	82
LPENE1	Linear	-	35	1	-	-
LPENE5	Linear	-	33	5	-	-
LPENE10	Linear	-	33	10	-	-
B4PE10NE1	Branched	Butyl	35	1	5	10
B4PE10NE5	Branched	Butyl	33	5	5	10
B4PE10NE10	Branched	Butyl	33	10	5	10
B4PE82NE1	Branched	Butyl	35	1	41	82
B4PE82NE5	Branched	Butyl	33	5	41	82
B4PE82NE10	Branched	Butyl	33	10	41	82
B6PE10NE1	Branched	Hexyl	35	1	5	10
B6PE10NE5	Branched	Hexyl	34	5	5	10
B6PE10NE10	Branched	Hexyl	36	10	5	10
B6PE82NE1	Branched	Hexyl	35	1	41	82
B6PE82NE5	Branched	Hexyl	33	5	41	82
B6PE82NE10	Branched	Hexyl	34	10	41	82

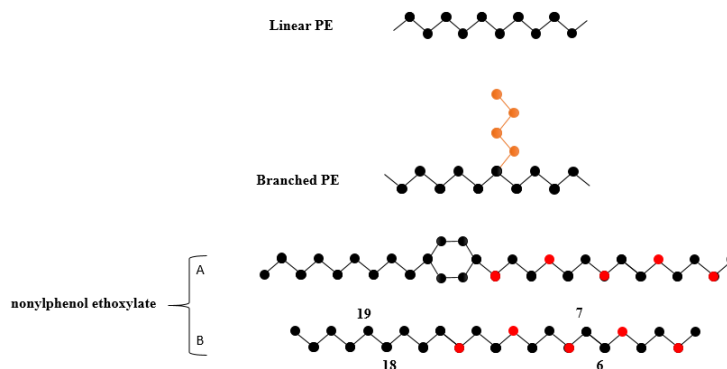


**Figure 15.** Structures of linear PE, branched PE and nonyl phenol ethoxylate (A), a common ESC agent and nonyl ethoxylate (B), an imitated ESC agent used in this work. Black, red dots are carbon and oxygen. The short chain branch is represented in orange.

### 3.3. Results and Discussion

The first part of the discussion will focus on the molecular packings of LPE and BPE as well as those in the presence of NE molecules at various concentrations. Here, the molecular packings are quantified by the corresponding RDFs. The free volume hole size and spatial distributions will be discussed afterwards. As mentioned, we hypothesize that the presence of an ESC agent in the amorphous phase of PE would alter the molecular packings of the dissimilar molecules in the systems, leading to the formation of regions having more and larger free volume holes, precursors for cavitation that is the precursor for the crack formation. Also, it is anticipated that the effect of the ESC agent on LPE and BPE would be different.

#### 3.3.1. Radial Distribution Functions of PE and NE

Interchain RDFs of pure PE with 0, 10, and 82 SCBs/1,000 backbone carbons and those of the same PE in the presence of NE at various concentrations (1, 5, and 10 NE) were determined and are plotted in Figure 16. As shown in Figure 16a, increasing the number of SCBs reduces the peak values of RDF plots but do not change the peak locations, suggesting that PE chains with more

SCBs adopt a less compact molecular morphology. Figure 16(b-d) show that the presence of NE hardly changes the locations and heights of the peaks in the RDFs of PE. This may be due to the low NE concentrations used ( $w_{NE} \sim 0.001 - 1.4 \text{ wt\%}$ ).

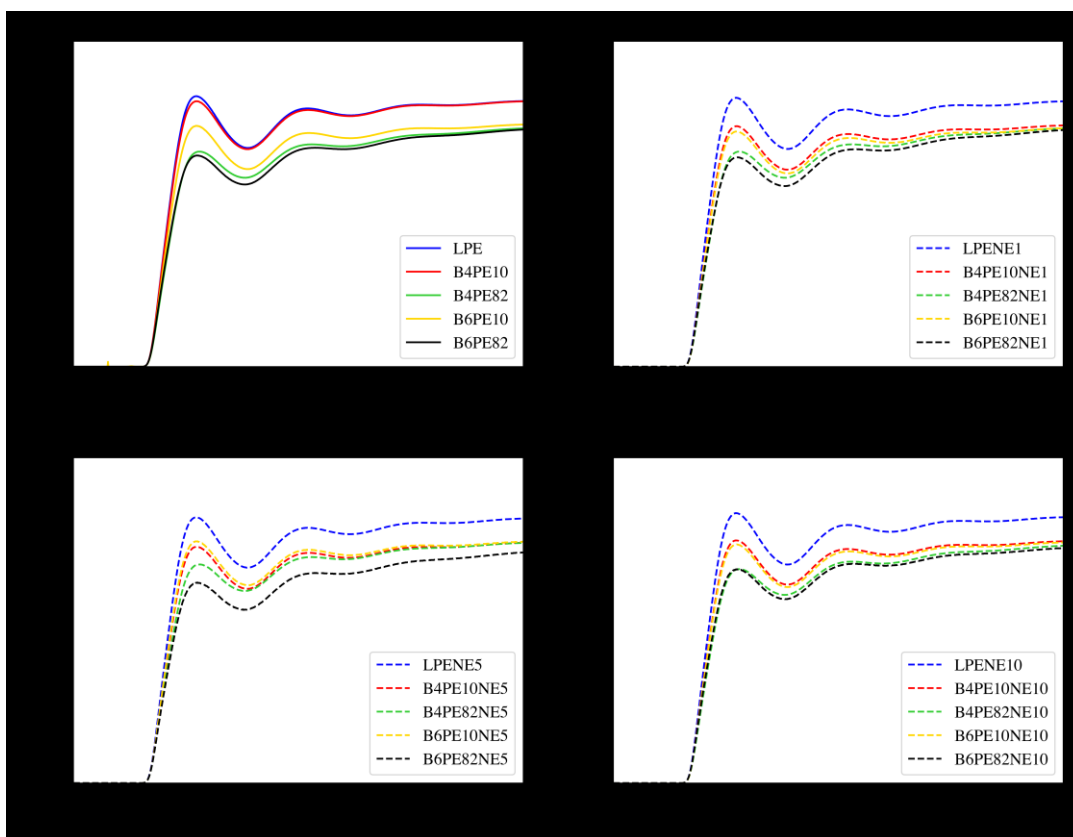


**Figure 16.** Inter-chain radial distribution functions (RDFs) of linear polyethylene (LPE) and branched polyethylene (BPE) in the absence of NE (a) and in the presence of 1 (b), 5 (c) and 10 (d) NE molecules (i.e.,  $w_{NE} \sim 0.001 - 1.4 \text{ wt\%}$ ).

Figure 17 shows the intermolecular RDFs between PE and the hydrophobic E-segments and hydrophilic EO-segments of NE. In both cases, the RDF becomes sharper as NE concentration increases. This is simply because increasing number of NE molecules yields better statistics. It is obvious that the RDF values of the E-segments of NE is slightly greater than those of the EO-segments, indicating that the E-segments exhibit a stronger association with both LPE and BPE

than the EO-segments, a somewhat expected result. However, such association seems to be insensitive to the branch content.

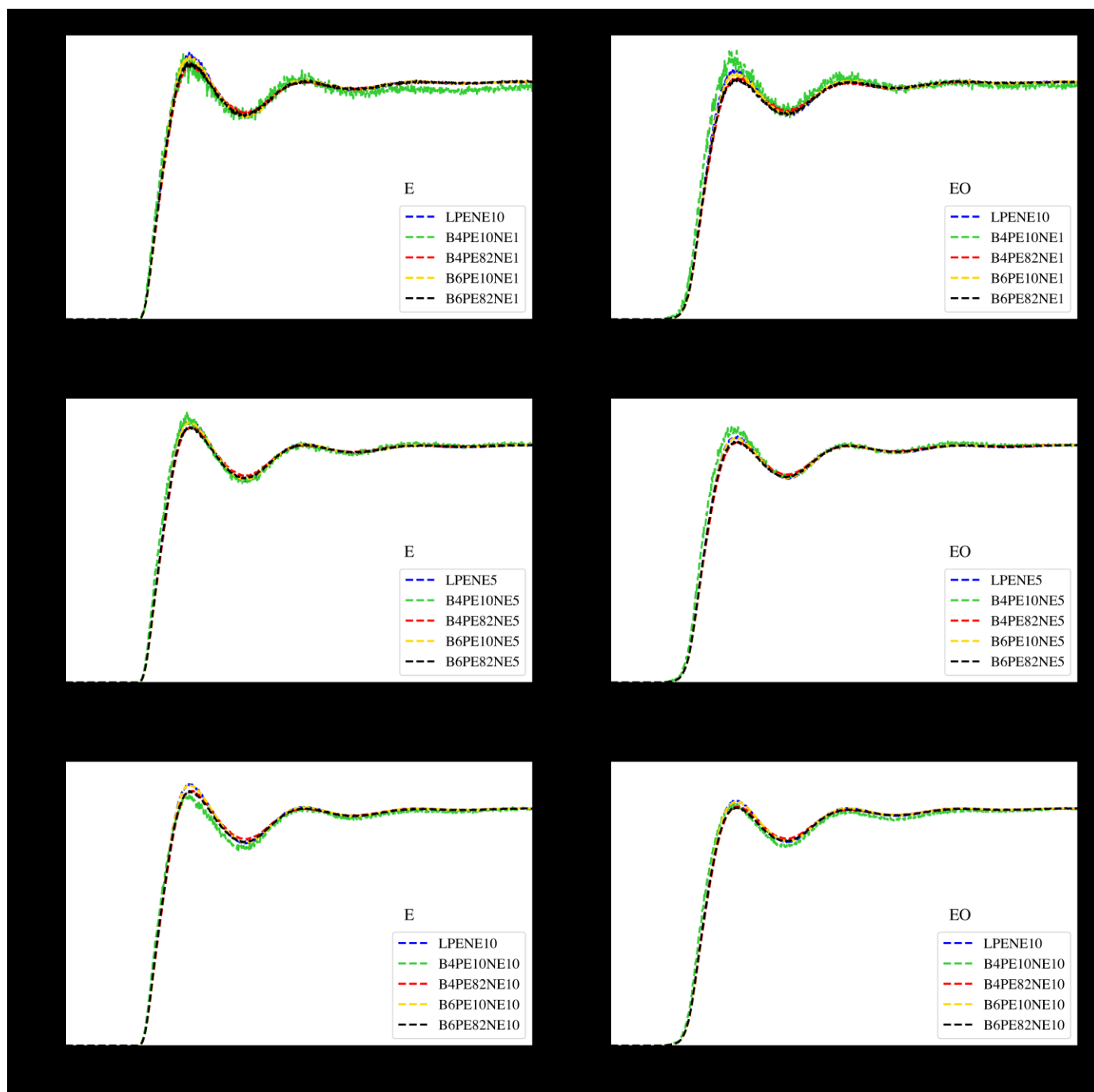


**Figure 17.** Intermolecular radial distribution functions for PE and NE's ethylene segments (E-segments) and ethylene oxide segments (EO-segments).

### 3.3.2. Free Volume Hole Size and Spatial Distributions

Figure 18 shows the free volume hole sizes of LPE, B4PE10, B4PE82, B6PE10, and B6PE82 from the corresponding equilibrated snapshots. Similar figures, not shown here, were obtained from different equilibrated MD snapshots. It can be determined from the figure that the *b*-Cs (the backbone carbon atom that the branch is attached to) are surrounded by a significantly smaller free volume as denoted by the green dots on the *x*-axes of the figures. The small free volume hole sizes of *b*-Cs are due to the fact that they are highly restricted as they are constrained by 3 covalent bonds, 7 bond angles, and 8 dihedrals. As a result, such carbons are not able to move as freely as other carbons in the same PE chain [124], [125]. We also determined the mean free volume hole sizes of the carbons in the butyl/hexyl branches and are shown in Table 3. It can be seen that the mean free volume hole size of the terminal carbons is significantly larger than those of the backbone carbons which are approximately 20 Å<sup>3</sup> (Figure 18). This is consistent with the fact that terminal carbons are more mobile. And the free volume hole size of a carbon in the branch decreases as the carbon is closer to the backbone. This observation is not surprising as such free volume distribution is very similar to that of chain ends (see Table 3).

**Table 3.** Mean free volume hole sizes of carbon atoms (Å<sup>3</sup>) in the last four carbon atoms of butyl/hexyl branches and the last four carbon atoms at the end of the PE polymer chains in the LPE system. Carbon #4 is the terminal carbon.

Carbon #	B4PE10 branches	B6PE10 branches	Chain ends (terminals)
1	6.7	19	10.7
2	9.2	20	11.4
3	10.6	22	12.5
4	30	40	32

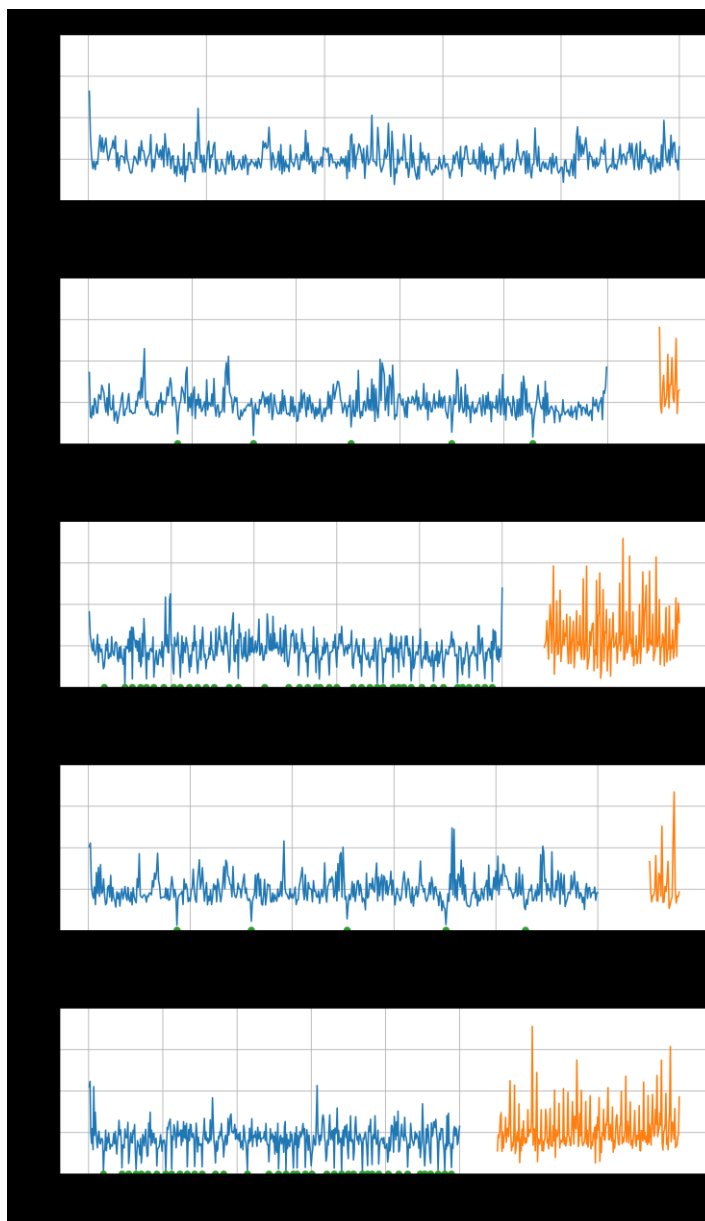
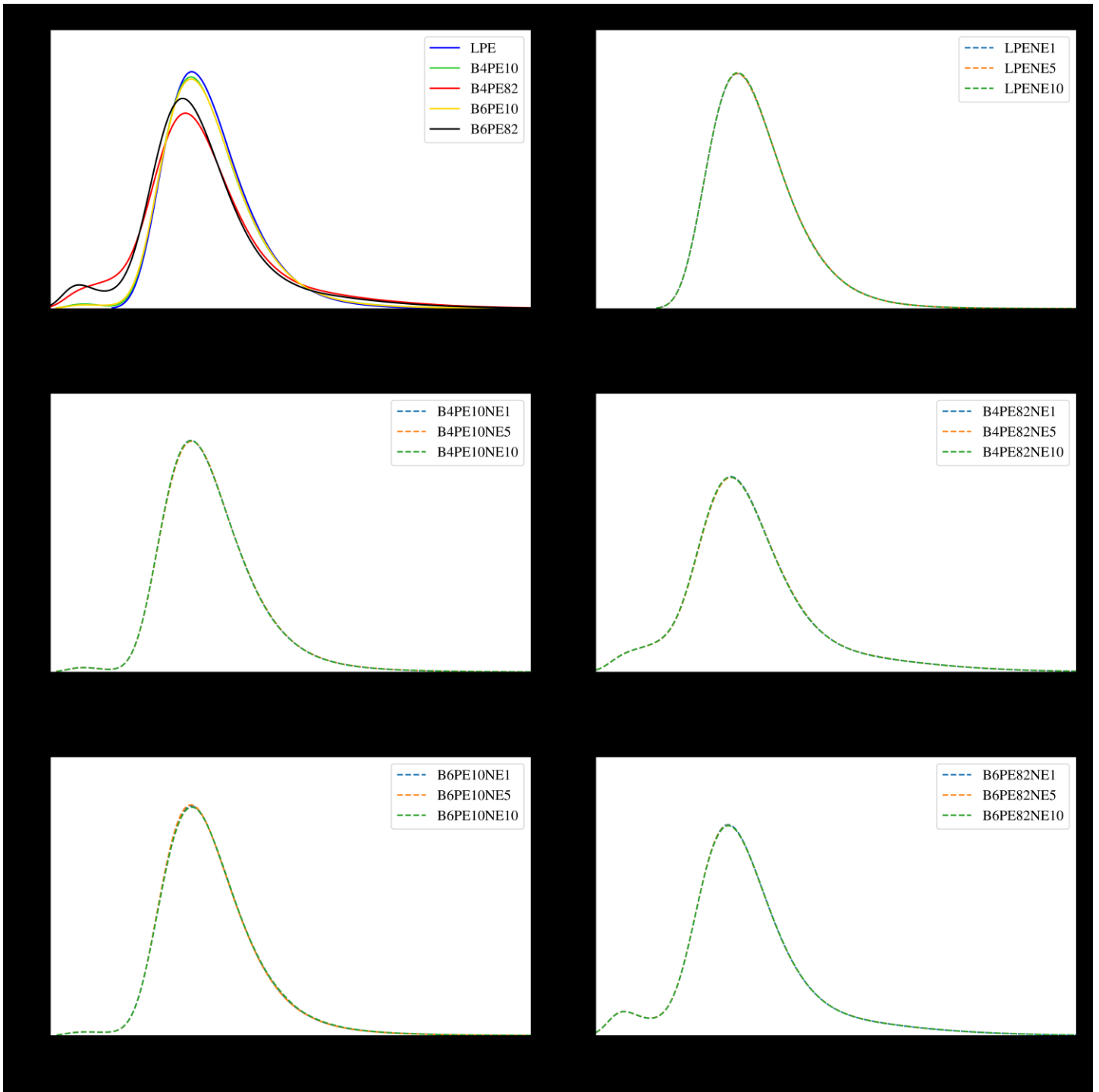


**Figure 18.** Free volume hole size of backbone carbons (blue) and carbons in the short chain branches (orange) of LPE and BPE chains as determined by the Voronoi tessellation (VT) method from an equilibrated snapshot (at 500 ns) of systems LPE, B4PE10, B4PE82, B6PE10 and B6PE82. The green dots on the  $x$ -axis denote the locations of the short chain branches ( $b$ -Cs).

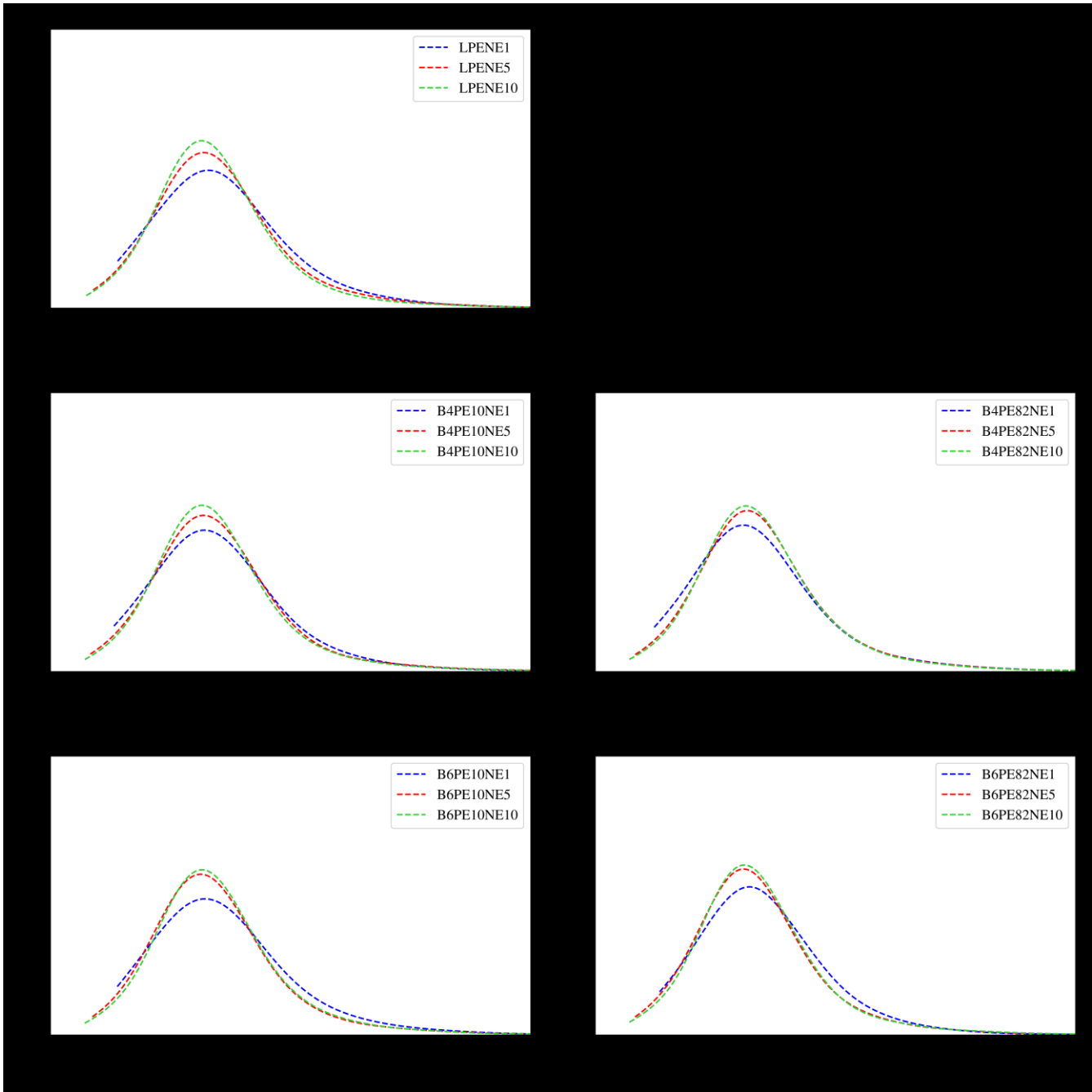
Figure 19 shows the free volume hole size distribution around each carbon in LPE and BPE. Figure 19a clearly shows that by increasing the number of branches in a PE chain, the free volume hole size distribution become broader with a second peak emerging in the range of  $v <$

$20 \text{ \AA}^3$  and the right tail  $v > 40 \text{ \AA}^3$  increases. As a result, the peak value of the mean free volume shifts toward left. It should be pointed out that for all cases, the right tail diminishes essentially to zero at  $60 \text{ \AA}^3$ . The broadening of the free volume hole size distribution is reasonable as there are more branches in the macromolecules yielding both small free volume holes associated with *b-Cs* and large free volume holes associated with the butyl/hexyl branches (Figure 18 and Figure 19). Figure 19(b-d) show that increasing NE concentration barely changes the free volume hole size distribution of PE chains in both LPE and BPEs.

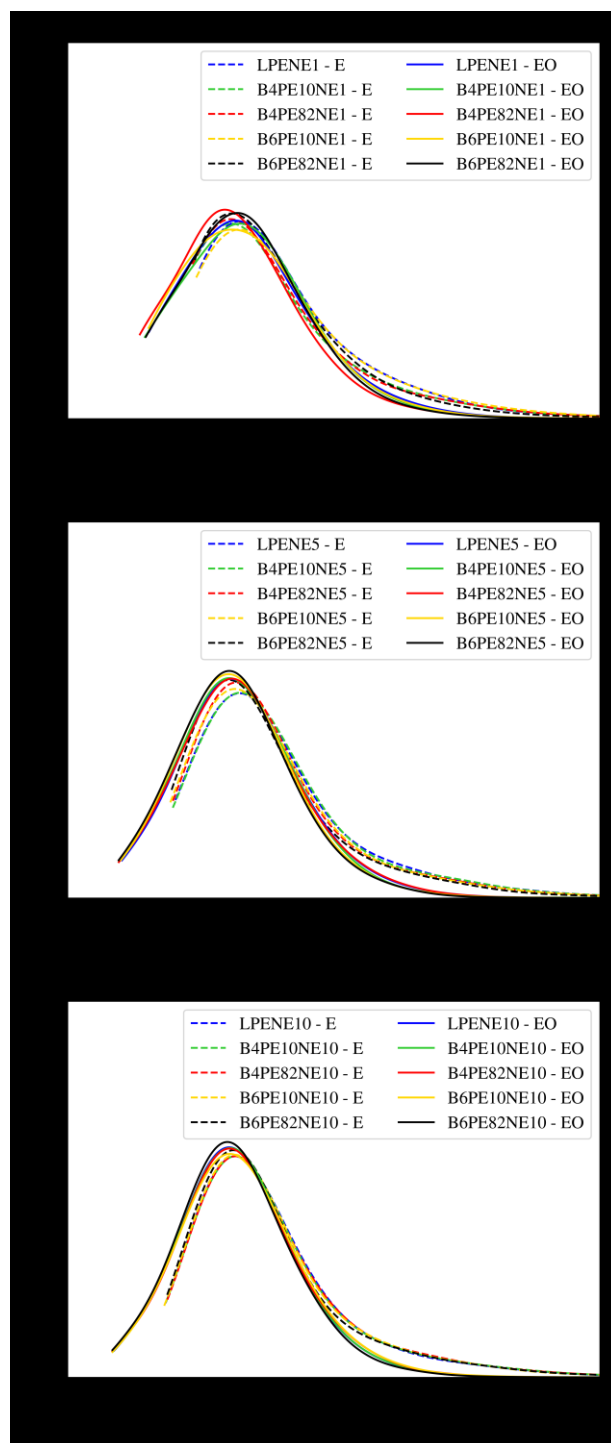
The free volume hole size distributions around the NE molecules are plotted in Figure 20. One obvious trend in Figure 20 is that for both LPE and BPE, increasing NE concentration increases the peak value (i.e., more free volume holes around the NE molecules). Also, in all cases, area under the curve determined based upon free volumes  $v > 10 \text{ \AA}^3$  exhibits a weak positive dependence on NE concentration:  $\sim 0.90$ ,  $0.92$  and  $0.94 \text{ \AA}^3$ . These results indicate that by increasing NE concentration, the free volume around the NE molecules increases. The effect is stronger for LPE than for BPE. This implies that the branches in BPE suppress the formation of free volume holes around the NE molecules. In summary, NE molecules when surrounded by PE chains, especially LPE molecules, forms more and larger free volume holes. It is believed that this will in turn increase the chance of the aggregation of such free volume holes (i.e., higher chance for cavitation), thereby crack formation over a long period of time, when PE is subject to internal/external stress. The results are consistent with the experimental observation (as mentioned in the introduction section of this chapter) that ESCR of BPE is higher than that of LPE.



**Figure 19.** The probability distributions of free volume hole size ( $v$ ) for LPE and various BPE models without and with NE at different concentrations.



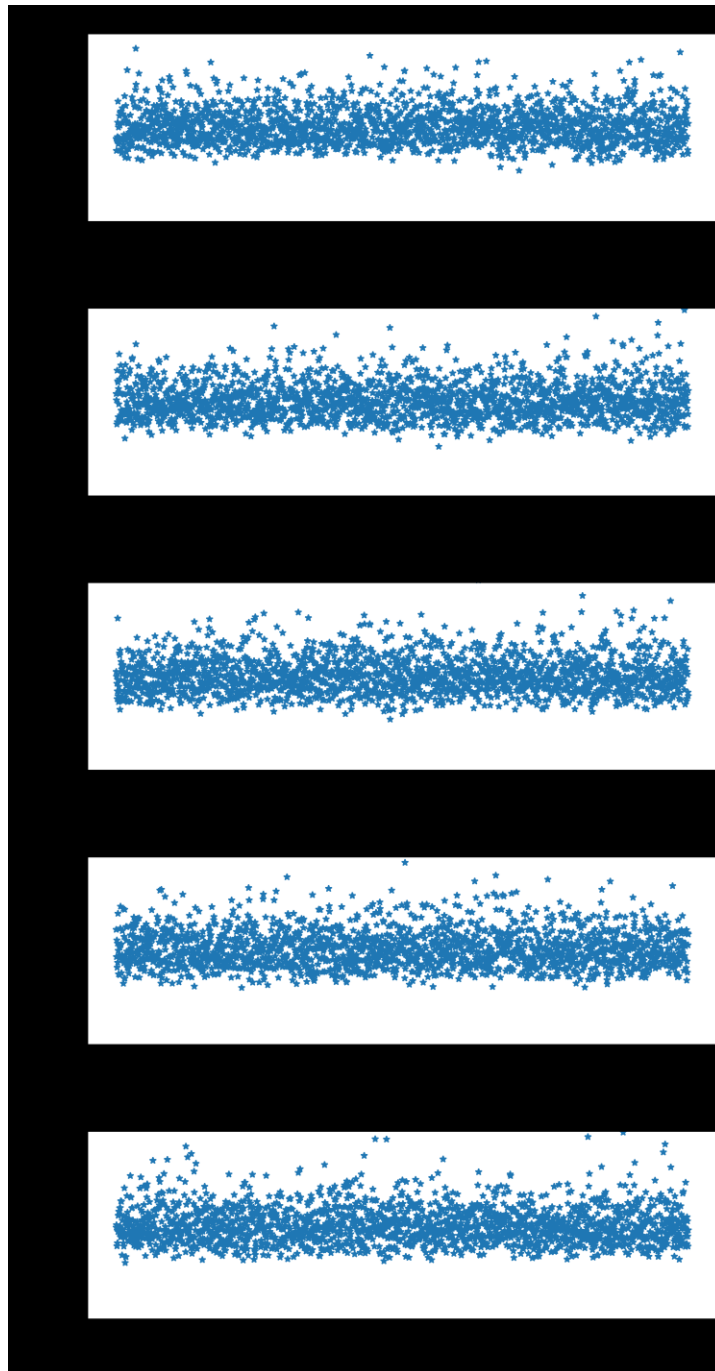
**Figure 20.** The probability distributions of free volume hole size ( $v$ ) around NE molecules in LPE and BPEs with NE at various concentrations.



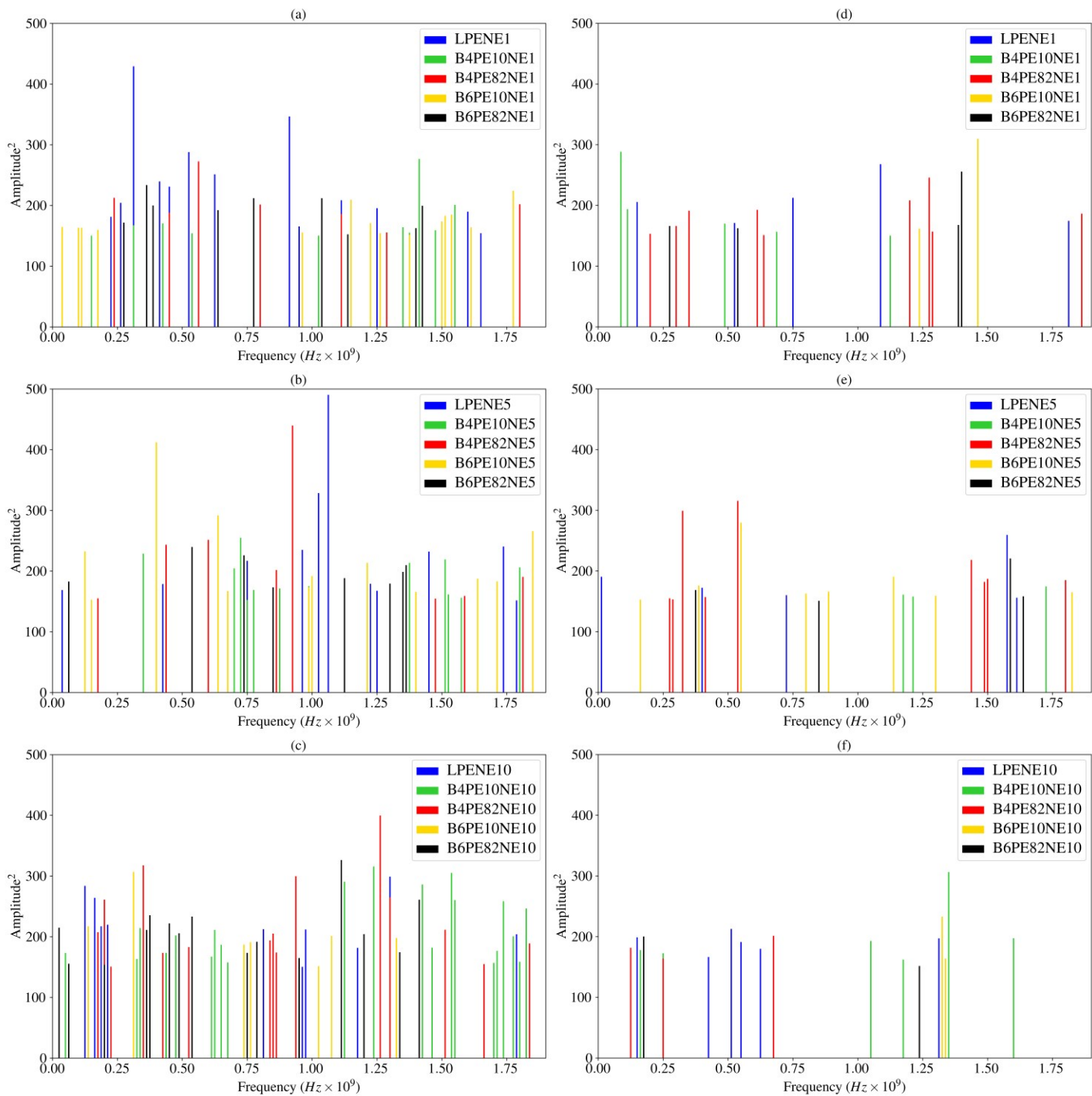
**Figure 21.** The probability distributions of free volume hole size ( $v$ ) for ethylene segments (E-segments) and ethylene oxide segments (EO-segments) of NE molecules.

Figure 21 shows the free volume hole size distributions of E-segments and EO-segments of NE molecules. This figure clearly shows that there are more relatively smaller free volume holes in the vicinity of the EO-segments than E-segments and that there are more relatively larger free volume holes in the vicinity of the E-segments than EO-segments. The smaller free volume holes of EO-segments could be due to their more compact conformation in a hydrophobic environment. Figure 21 also shows that by increasing the branch content and branch length, the peaks of the probability curves of E-segments shift to the left, suggesting that systems with higher branch contents and/or larger branches would reduce the formation of free volume holes around the E-segments. We will discuss this point further when we present the free volume holes coalescence dynamics analysis.

To analyze the free volume coalescence dynamics around the NE molecules, two nearby carbon atoms  $C_{\#6}$  ( $NE_6$ ) and  $C_{\#7}$  ( $NE_7$ ) in the EO-segments and  $C_{\#18}$  ( $NE_{18}$ ) and  $C_{\#19}$  ( $NE_{19}$ ) in the E-segments (Figure 15) of the NE molecule were selected. In particular, we followed the time evolution of the total free volume of the two pairs of carbons (i.e.,  $v_{fNE_6} + v_{fNE_7}$  and  $v_{fNE_{18}} + v_{fNE_{19}}$ ) from a randomly selected NE molecule in each system. Figure 22 shows the time evolution of  $v_{fNE_{18}} + v_{fNE_{19}}$  for the systems with the highest NE concentration used. Here, results on  $v_{fNE_6} + v_{fNE_7}$  are not shown as they are similar to those of  $v_{fNE_{18}} + v_{fNE_{19}}$ . However, they differ when the free volume coalescence dynamics data are expressed in the Fourier modes. In Figure 23, we show the last 80 ns of the data of  $v_{fNE_6} + v_{fNE_7}$  and  $v_{fNE_{18}} + v_{fNE_{19}}$  in the Fourier mode. Here, to attenuate the frequencies with lower amplitudes, we squared the amplitudes. We also applied a filter of 150 on the squared values to remove the low intensity activities.



**Figure 22.** The time evolution of  $v_{f_{NE_{18}}} + v_{f_{NE_{19}}}$  for systems, (a) LPENE10, (b) B4PE10NE10, (c) B4PE82NE10, (d) B6PE10NE10 and (e) B6PE82NE10



**Figure 23.** The Fourier modes for  $v_{f_{NE_{18}}} + v_{f_{NE_{19}}}$  (E-segments: a, b and c) and  $v_{f_{NE_6}} + v_{f_{NE_7}}$  (EO-segments: d, e and f) of NE molecules.

Fourier transforms of such time series data yielded the power (amplitude) of the free volume fluctuations. By considering the time series  $f(t) = v_{fNE_i} + v_{fNE_j}$ , where  $i$  and  $j$  are two consecutive atoms  $i$  and  $j$  in a NE molecule, the Fourier transform was performed on the time series by using [150]:

$$F(\omega) = \int_{-\infty}^{\infty} f(t)e^{-i\omega t} dt \quad (3-1)$$

where  $F(\omega)$  is the evaluated transformed function,  $\omega$  is Fourier frequency and  $t$  is time. The Fast-Fourier transform (FFT) method is utilized to numerically calculate the Fourier transform [150]. After that, the power of fluctuations of the time series  $f(t)$  is evaluated by using [151]:

$$E = \frac{1}{T} \int_T |f(t)|^2 dt \quad (3-2)$$

which by considering Parseval's theorem [152], it also can be calculated by:

$$E = \sum_{k=-\infty}^{\infty} |F_k|^2 \quad (3-3)$$

where  $F_k$  is the amplitude of the  $k^{\text{th}}$  Fourier mode. The power or number of frequencies of a signal, positively correlates to the activity in the coalescence of free volume. Following the Fourier transform of  $f(t)$ , a filter is employed to eliminate noise and undesirable components or features from the signal of the fluctuations. Based on our prior paper, it is recommended to use a filter of 150 on *Amplitude*<sup>2</sup> [135].

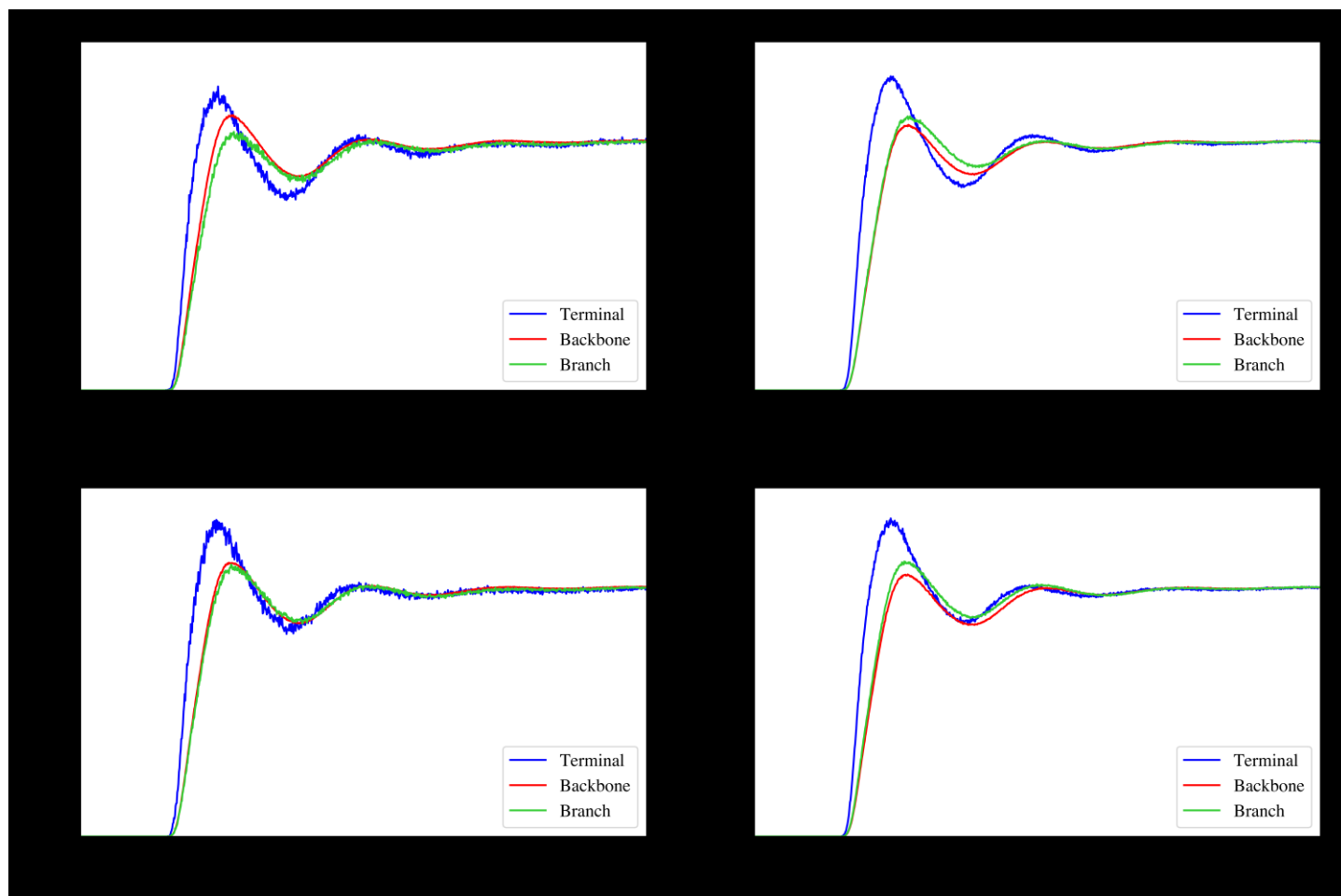
Figure 23 clearly shows that the number of frequency modes of the E-segments is much higher than that of EO-segments and that some of the frequency mode intensities of the E-segments are considerably larger than those of the EO-segments. Also, the number of frequency modes decreases significantly with increasing NE concentration for the EO-segments but not the E-segments. To quantify the above observation, we summarize the number of frequency modes and the total power  $\sum Amplitude^2$  in Table 4 and Table 5, respectively.

Table 4 show that increasing NE concentration increases the number of frequency modes of E-segments but decreases that of EO-segments, especially from NE5 to NE10 systems and that increasing branch content generally decreases the number of frequency modes. This result supports the ideas that more coalescence activities take place when more E-segments are present and that SCBs, especially the terminal carbons, reduce such activities. Table 5 clearly shows that the intensity of free volume coalescence for E-segments is much stronger than that for EO-segments and reduces in the presence of SCBs.

The RDFs between the terminal carbons in the SCBs and E-segments confirms that they have strong association compared to the other carbons (see Figure 24). In Figure 24, only the results for the systems with 10 NE molecules are plotted as the results for lower NE concentrations are similar. It seems that terminal carbons in SCBs which are more mobile suppress the formation of large free volume holes at the [PE]-[E-segments] interfaces by absorbing the newly formed free volume by that of the terminal carbons.

The free volume and free volume dynamics results suggest that coalescence of free volume holes takes place at very frequency modes along with high intensities at the [PE]-[E-segments]

interfaces, thereby increasing the chance for cavitation, a precursor for crack formation. The role of SCBs seem to restrain the coalescence of the free volume holes in the vicinity of E-segments by absorbing such freshly formed free volume into their relatively larger free volume.



**Figure 24.** Radial distribution functions (RDFs) of terminal carbons, branch carbons (terminal carbons excluded) and backbone carbons of BPEs as referenced to the E-segments of the NE molecules for different types of BPEs with 10 NE molecules.

**Table 4.** The number of frequency modes for the coalescing free volume  $v_{fNE_{18}} + v_{fNE_{19}}$  (E-segments) and  $v_{fNE_6} + v_{fNE_7}$  (EO-segments) for different systems.

System type	NE1		NE5		NE10	
	E	EO	E	EO	E	EO
LPE	13	5	13	6	16	6
B4PE10	13	6	12	3	24	6
B4PE82	7	10	8	11	17	3
B6PE10	15	2	12	8	7	2
B6PE82	9	4	8	4	15	2
Summation	57	27	53	32	79	19
Total (E+EO)	84		85		98	

**Table 5.** The total power ( $\sum Amplitude^2$ ) for the coalescing free volume  $v_{fNE_{18}} + v_{fNE_{19}}$  (E-segments) and  $v_{fNE_6} + v_{fNE_7}$  (EO-segment) for different systems.

System type	NE1		NE5		NE10	
	E	EO	E	EO	E	EO
LPE	3085	1031	2848	1101	3342	1146
B4PE10	2275	1141	2312	493	4992	1209
B4PE82	1418	1802	1796	2230	3697	547
B6PE10	2586	471	2637	1452	1452	397
B6PE82	1736	752	1598	698	3126	352
Summation	11100	5197	11191	5974	16609	3651
Total (E+EO)	16297		17065		20260	

### 3.4. Conclusion

We used molecular dynamics simulation to study the molecular morphology in the amorphous phase of LPE and BPE with 10 and 82 butyl/hexyl branches/1,000 backbone carbons in the presence of an ESC agent namely nonyl ethoxylate (NE). Packings of LPE and BPE were not affected by the presence of NE as characterized by both (i) their interchain radial distribution functions and (ii) free volume hole size distributions as determined by the technique of VT. The E-segments of NE, compared to the EO-Segments, exhibited a strong association with the PE chains, especially with the terminal carbons of the short chain branches in BPE. Increasing NE concentration increased the number and size of free volume holes at the [PE]-[E-segments] interfaces. It is believed that this will, in turn, increase the chance of free volume coalescence (i.e., cavitation, the precursor for the crack formation). It is interesting to note that short chain branches in BPE were observed to suppress the formation of free volume holes around the [PE]-[E-segments] interfaces. The Fourier mode analysis of free volume holes coalescence dynamics indicates that E-segments of NE molecules exhibit considerably more activities in free volume holes coalescence than the EO-segments, supporting the idea that cavitation is likely to take place at the [PE]-[E-segments] interfaces. The Fourier mode analysis also shows that the presence of more mobile short chain branches nearby the E-segments restrains the formation of large free volume holes. This can be viewed as the newly formed free volume holes are absorbed by the large free volume holes associated with the terminal carbons. In this work, we propose a different view on the initiation of the ESC process using the free volume concept.

### **3.5. Acknowledgments**

The authors gratefully acknowledge the financial support from Imperial Oil through the IOL University Research Awards program. This study was also enabled by the high-performance computing resources provided by WestGrid, Compute Canada ([www.computecanada.ca](http://www.computecanada.ca)).

# Chapter 4: Effect of Molecular Backbone Size on Free Volume Coalescence

\*Version of this chapter's sections has been published in: Kavyani S., Soares J. B. P. Choi P., The Size Effect of Backbone with Attached Hexyl Branches on the Free Volume Size Distribution and Coalescence around an Amphiphilic Molecule. *Polymer Engineering & Science*, 2024.

---

## 4.1. Introduction

PE is commonly used in a wide range of consumer and industrial products due to its versatility, low cost, and ease of manufacturing. It is a thermoplastic polymer made from the monomer ethylene and is characterized by its flexibility and durability. Some of the common applications of polyethylene include packaging, consumer goods, electrical and electronic components, construction materials and pipelines.

When a polyethylene sample is exposed to an amphiphilic liquid and subjected to a stress at the same time, it will crack prematurely [113]. This type of failure is termed as ESC [53], [113]. The cracks obviously reduce PE's strength and durability [8]. In general, ESC is believed to take place in the following steps: *i*) amphiphilic liquid absorption, *ii*) crack propagation and *iii*) brittle

fracture [115]. It is important to point out that the rate of the progression of each stage varies depending on the macromolecular structure of polyethylene and the conditions it is exposed to (e.g., temperature, type and concentration of the amphiphilic liquid and stress level).

Certain polyethylene shows only limited crack growth and takes a longer time to fail while others exhibit rapid crack growth and fail quickly. However, in ESC failures, slow crack growth (SCG) is the dominant mode of failure and it has been observed as an interlamellar phenomenon, only occurring in the amorphous phase of polyethylene [126]–[128].

The crack propagation stage can be divided into three sub-stages: *i*) cavitation (void formation), *ii*) craze initiation, and *iii*) crack growth. Properties of PE that play significant roles in the rate of the crack propagation stage are the degree of crystallinity [44], molecular weight [41], [42], degree of branching [45], and size of branches [49]. The above properties are not totally independent. For example, the degree of branching determines the degree of crystallinity under the same crystallization conditions. The degree of branching of PE and its degree of crystallinity show a negative dependence [48].

Nonetheless, it has been shown that the branch content and branch length (size) of PE exert a strong influence on the crack propagation stage. It is well-known that HDPE that contains essentially no branches exhibits low ESCR compared to BPE such as LDPE containing both LCBs and SCBs or LLDPE containing only SCBs. It is well-known that amount of SCBs determines the concentration of tie molecules that are the segments of a macromolecule reside in the amorphous phase. Their function is to bridge crystalline lamella. Ward *et al.* [46], proposed that the disentanglement of tie molecules is the molecular mechanism responsible for ESC.

Bubeck *et al.* [45] investigated the effects of the number and length of SCBs on the ESCR of PE and found that increasing the number and length of SCBs, improves the ESCR of PE. Yeh *et al.* [49] showed that when the branch length increases from ethyl to hexyl branches, the ESCR of PE increases significantly. Also, it has been observed that LLDPE exhibits higher ESCR with butyl branches compared to ethyl branches [3], [47], [38].

Lu *et al.* [129] reported that by increasing the amount of SCBs, the polyethylene service lifetime even in the presence of an amphiphilic ESC agent increases SCG period. They also mentioned that SCBs serve a dual role, acting as pins that impede the sliding of tie molecules on each other and simultaneously restricting lamella thickness, leading to an increase of the percentage of amorphous phase and tie molecules. Lustiger *et al.* [126] found out that SCBs help improve ESCR of PE in two ways: *i*) reducing its crystallinity, *ii*) increasing the number of tie-molecules and *iii*) preventing tie molecules from slipping past another.

Böhm *et al.* [57] suggested that pipes made of a PE blend containing PE with SCBs on a long backbone (e.g., LLDPE) exhibit approximately two orders of magnitude higher ESCR. The potential beneficial of PE blends was investigated previously by Hubert *et al.* [128], where they mentioned that ethylene/ -olefin copolymers with a bimodal molar weight distribution exhibit a higher ESCR. They also showed that SCBs attached to a long PE backbone improves ESCR [130]. Krishnaswamy *et al.* [131] investigated the time to failure of different binary PE blends containing PE with SCBs placed exclusively either on “short” or “long” backbone and found that SCBs on long backbone delay failure significantly.

Free volume is the space that is not occupied by the molecules in a material [132]. By using the free volume concept, Wong and Choi have been successful in predicting diffusivity and viscosity of PE with different macromolecular structures [112], [133], [134]. Most recently, we found that relatively larger free volume holes are formed at the interface between an amphiphilic molecule and the amorphous phase of PE and that such free volume holes exhibit high propensity for coalescence [135]. We believe that such free volume coalescence forms the precursor for the cavitation process, the first stage of SCG. In the same work, we also demonstrated that SCBs suppress free volume holes coalescence. This is somewhat in line with the experimental observations that SCBs help improve ESCR. It is noteworthy that our previous work was carried out at a temperature above the melting temperature of PE used in order to ensure the equilibration of its amorphous phase. However, we expect that a similar coalescence process would take place at lower temperatures but at much slower rates, as in real life it takes place in a room temperature.

In the previous work, neat PE was used. In this work, we will further our study using PE blends containing PE with linear structure and with hexyl branches. A four-arm star alkane namely 7, 12 hexyl octadecane, hereafter referred to as SA was also added to the PE blend. Here, SA contains four hexyl branches but they are all attached to a backbone containing only four carbons. The objective of this study is twofold. One is to study the effect of blending and the other is on the effect of hexyl branches that are attached to backbones with significantly different sizes.

## **4.2. Molecular Dynamics (MD) Simulations**

We used the GROMACS 2020.4 software package [27 - 28] to run all MD simulations. The TraPPE force-field was used. This force field has been successfully used to describe the short chain branching effect on the interlamellar structure of LLDPE [94], [95] and also on the short and long

chain branching effects on the topology of PE melt [95]. The TraPPE force field was also used by Wong *et al.* [112] to determine how free volume affects the diffusivity of PE. Most recently, our group has used the same force field to study the effect of short chain branching on the size distribution and coalescence dynamics of free volume holes of PE in the presence of an ESC agent [135].

The simulation boxes for all the systems were set to  $\sim 15 \times 15 \times 15 \text{ nm}^3$  initially. We used Parrinello-Rahman barostat [75] to control the pressure at 1 *bar*. All simulation systems were coupled to a heating bath with a modified Berendsen thermostat that was set at a temperature of 190 °C [120]. It is noteworthy that since our main interest is on the free volume characteristics in the amorphous phase of PE blends in the presence of a star alkane and an ESC agent, we used a temperature that is significantly above the melting temperatures of PEs to ensure the equilibration of the amorphous phase of all blends [119]. It is believed that what is observed at 190 °C would occur at low temperatures but with low rates. It should be noted that equilibrating the systems of interest at low temperatures would require prohibitively high computational cost.

MD simulations were performed on all systems for at least 530 *ns*, which is sufficient to equilibrate the systems of interest [135], and the last 30 *ns* of the trajectories was used for the data analysis. The time step was set to 2 *fs*. The update frequency for neighbour searching was set to every 5 steps. The periodic boundary conditions were applied to all three dimensions *x*, *y* and *z*. In order to calculate the electrostatic forces between charged particles, the Particle Mesh Ewald (PME) method was used [65].

The PE blends contained LPE and BPE with short chain branches. To introduce more branches to the PE blends, we added a four-arm small alkane molecule namely 7, 12 hexyl octadecane (SA), which contains four chain ends, to the PE blends. This reason of studying systems containing a considerable amount of branches is that our previous work [135] showed that the chain ends of BPEs suppress the coalescence of free volume holes (i.e, cavitation, the first step of ESC).

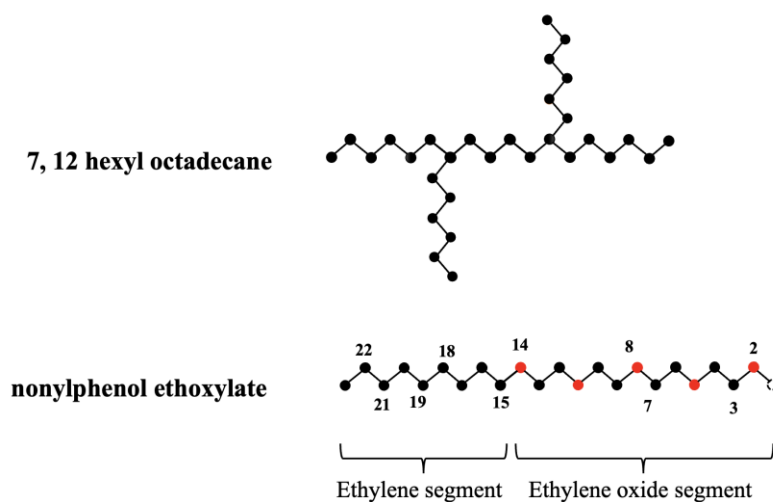


**Figure 25.** Molecular structures of 7, 12 hexyl octadecane (SA) and nonyl ethoxylate (NE). The black, red and white dots signify carbon, oxygen and hydrogen atoms, respectively.

All simulation systems contained different concentrations of LPE, BPE and SA but with the same amount of a simple amphiphilic ESC agent, nonyl ethoxylate (NE), at a concentration of  $\sim 0.5$  wt%. NE consists of a hydrophobic ethylene segment (E-segment) and a hydrophilic ethylene oxide segment (EO-segment). The LPE model contained 500 carbon atoms while the LLDPE models contained 500 carbon atoms in the backbone with 10 and 82 hexyl SCBs/1,000 backbone carbon atoms. Using a branch content of 82 was simply to amplify the chain end effect. The Voronoi tessellation method was used to calculate the volumes of the atoms[135]. The

molecular structures of SA and NE molecules used are illustrated in Figure 25 and all simulated systems are listed in Table 6.

**Table 6.** Concentrations of LPE, BPE, SA and NE molecules used in the simulations

#	System Name	Number of LPE molecules	Number of BPE molecules	Number of SA molecules	Number of NE molecules	Number of branch terminals/system
1	LPE_5BPE10	35	5	-	5	25
2	LPE_10BPE10	24	10	-	5	50
3	LPE_20BPE10	12	20	-	5	100
4	LPE_5BPE82	35	5	-	5	205
5	LPE_10BPE82	24	10	-	5	410
6	LPE_20BPE82	12	20	-	5	815
7	LPE_50SA	39	-	50	5	200
8	LPE_100SA	34	-	100	5	400
9	LPE_200SA	30	-	200	5	800
10	LPE_5BPE10_200SA	25	5	200	5	825
11	LPE_10BPE10_100SA	17	10	100	5	450
12	LPE_20BPE10_50SA	10	20	50	5	300
13	LPE_5BPE82_200SA	25	5	200	5	1005
14	LPE_10BPE82_100SA	17	10	100	5	810
15	LPE_20BPE82_50SA	10	20	50	5	1015

## 4.3. Results and Discussion

### 4.3.1. Equilibration

Figure 26 and Figure 27 show the radial distribution functions (RDFs) of LPE, BPE, SA and SCBs including the branch terminals calculated using E- and EO-segments of NE as the references, respectively. In general, the first peaks of the RDFs located at around 0.5 nm using E-segments as references are higher. Branch terminals, regardless of BPEs and SA, exhibit much

higher first peaks, clearly demonstrating that branches (either from BPE or SA) tend to cluster around both the E- and EO-segments. However,

Figure 26a-f and Figure 27a-f seem to indicate that an “optimal” branch concentration (within the concentration range of BPE of interest) exists in the PE blends to maximize the interaction between the BPE branches and NE (Figures 2b and 3b).

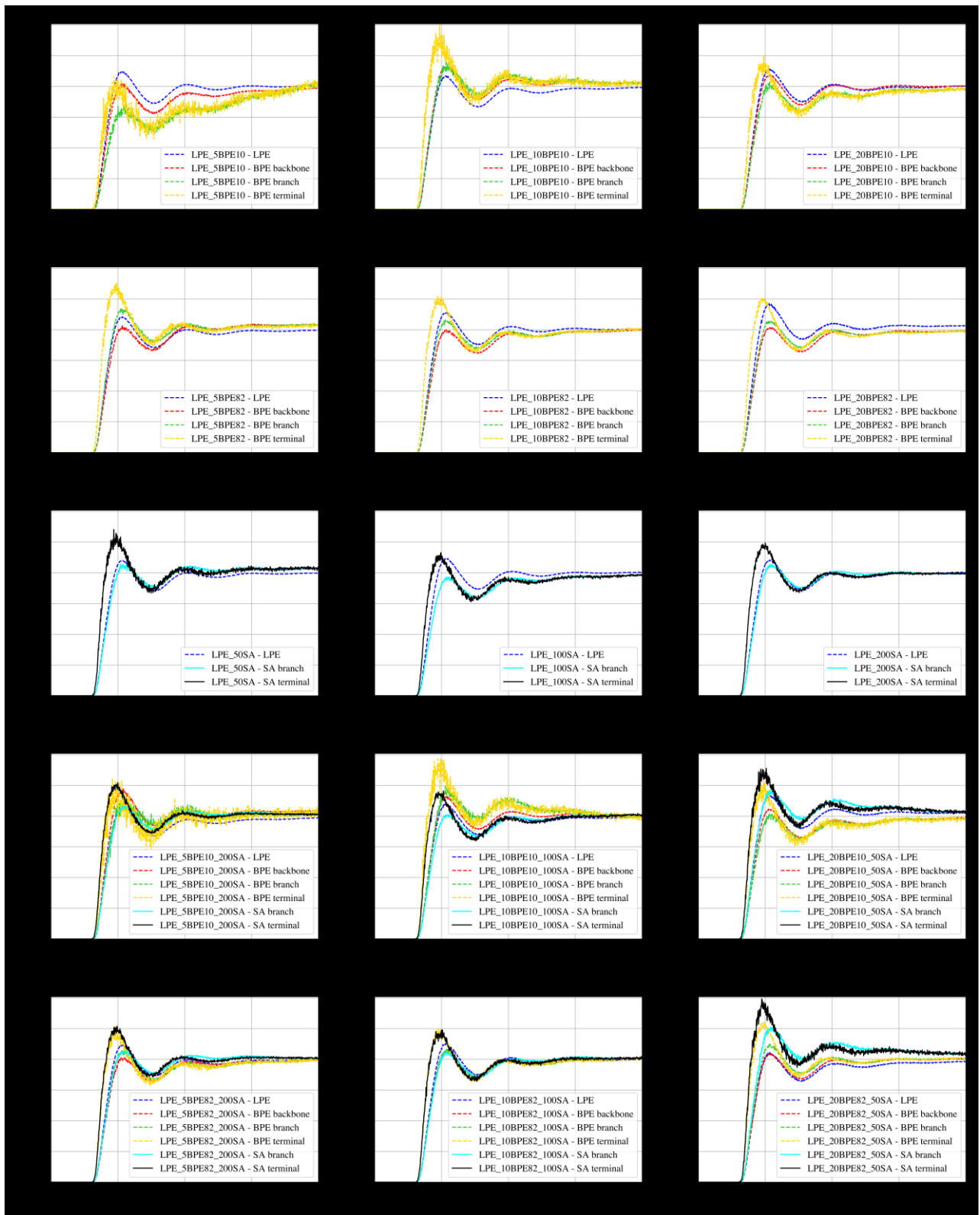
On the other hand,

Figure 26g-i and Figure 27g-i show that by adding more SA molecules in LPE, the height of the first peak of the branches decreases (from 50 to 100 SA molecules) and then increases (from 100 to 200 SA molecules), indicating that an “optimal” branch concentration (within the concentration range of SA of interest) exists to minimize the interaction between the SA branches and NE. Similar behavior is also observed for PE blends (

Figure 26j-o and Figure 27j-o). The aforementioned results suggest that branches of BPE and SA, with comparable sizes but attached to backbones with significantly different sizes, behave differently in terms of interacting with NE. Nonetheless, Figure 28 shows that the first peaks of the RDFs are significantly below 1, indicating that BPE and SA do not cluster much together in the PE blends.

It is clear from the above results that branches from BPE or SA tend to cluster in the vicinity of NE. However, it is not clear whether both types of branches, behaving somewhat differently, would help facilitate the coalesces of free volume holes, the first step of cavitation? As we showed

in our previous work [26], branches from BPE do facilitate the formation of larger free volume holes around NE.



**Figure 26.** Radial destruction functions (RDFs) of LPE, BPE, SA and their branches using the E-segments (E) of NE as the reference for all fifteen simulation systems as depicted in Table 1.

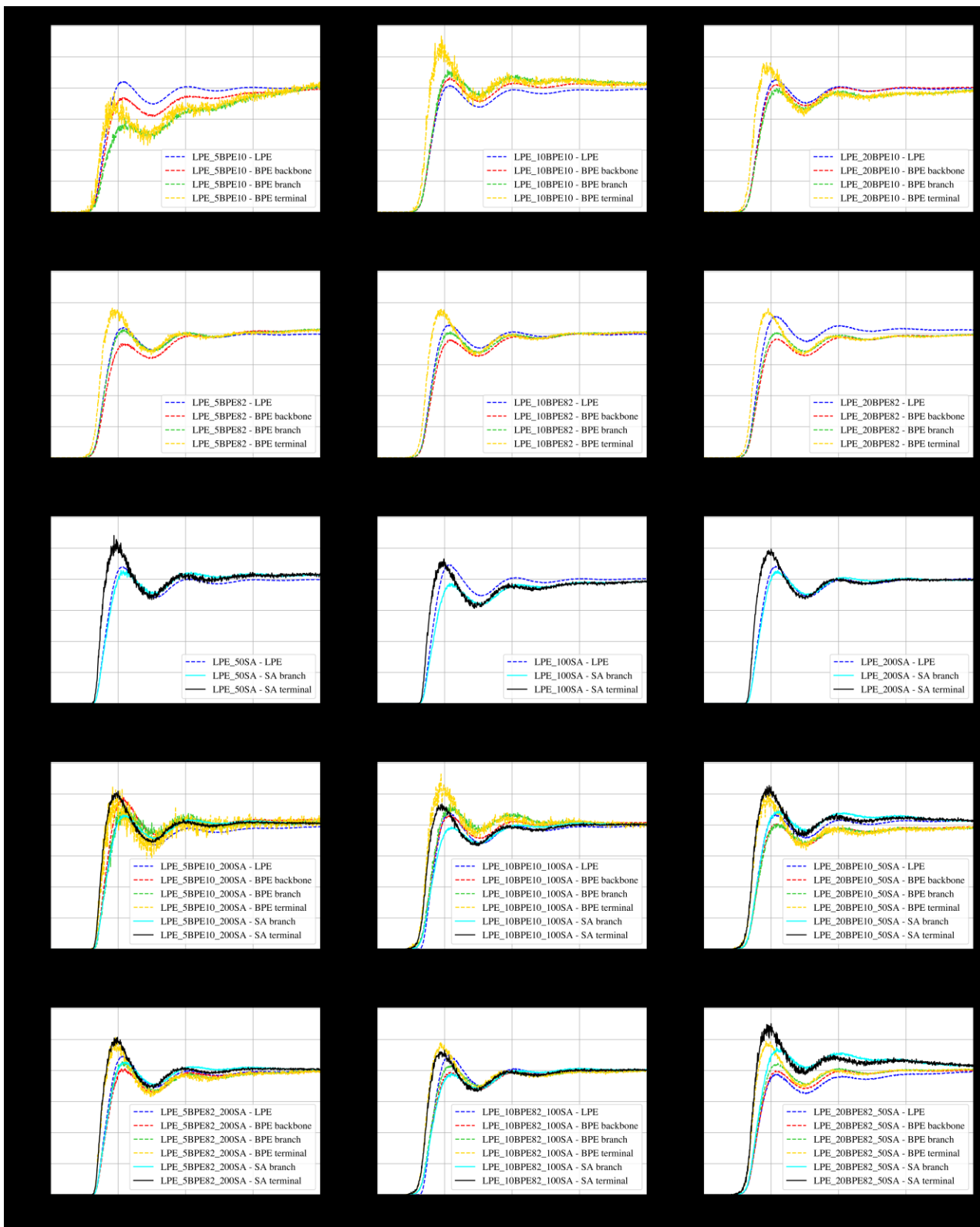


**Figure 27.** Radial distribution functions (RDFs) of LPE, BPE, SA and their branches using EO-segments (EO) of NE as the reference for all fifteen simulation systems as depicted in Table 1.

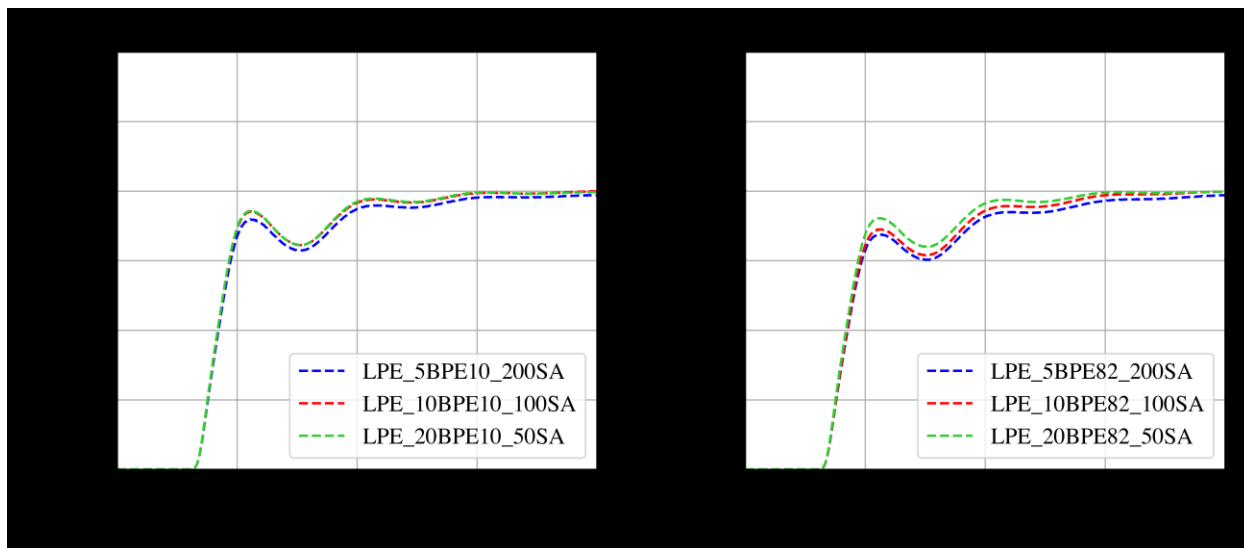


**Figure 28.** Radial distribution functions (RDF) of SA molecules with referenced by BPE.

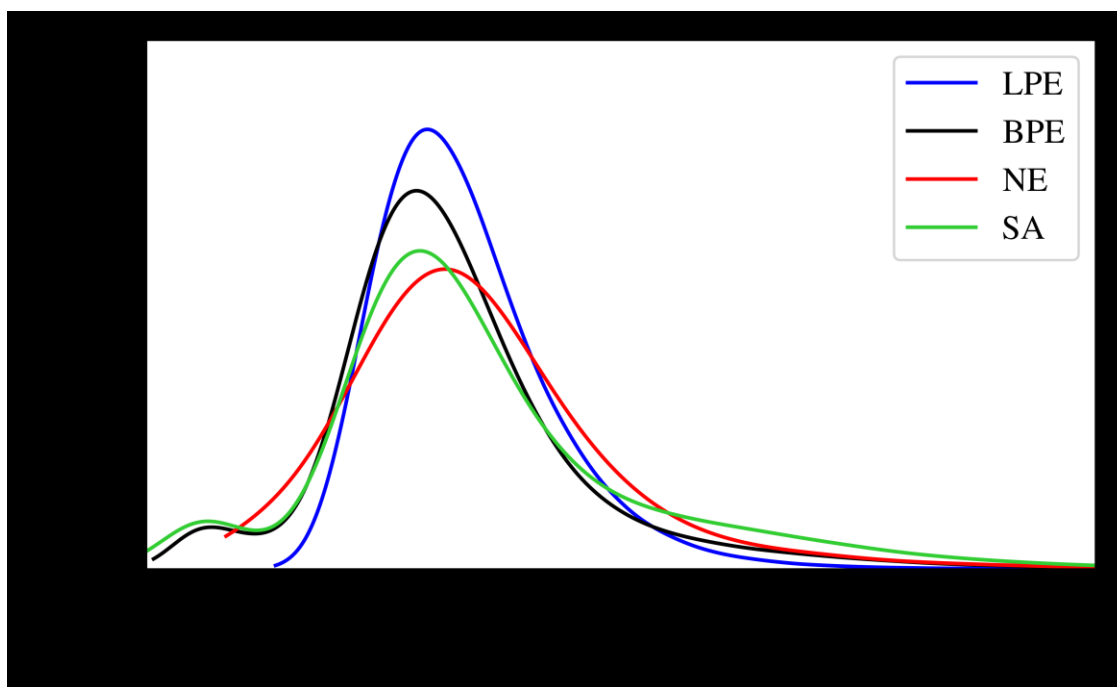


**Figure 29.** The probability distributions of free volume hole size ( $v$ ) of LPE, BPE, NE and SA, averaged on systems 10 to 15 in Table 6.

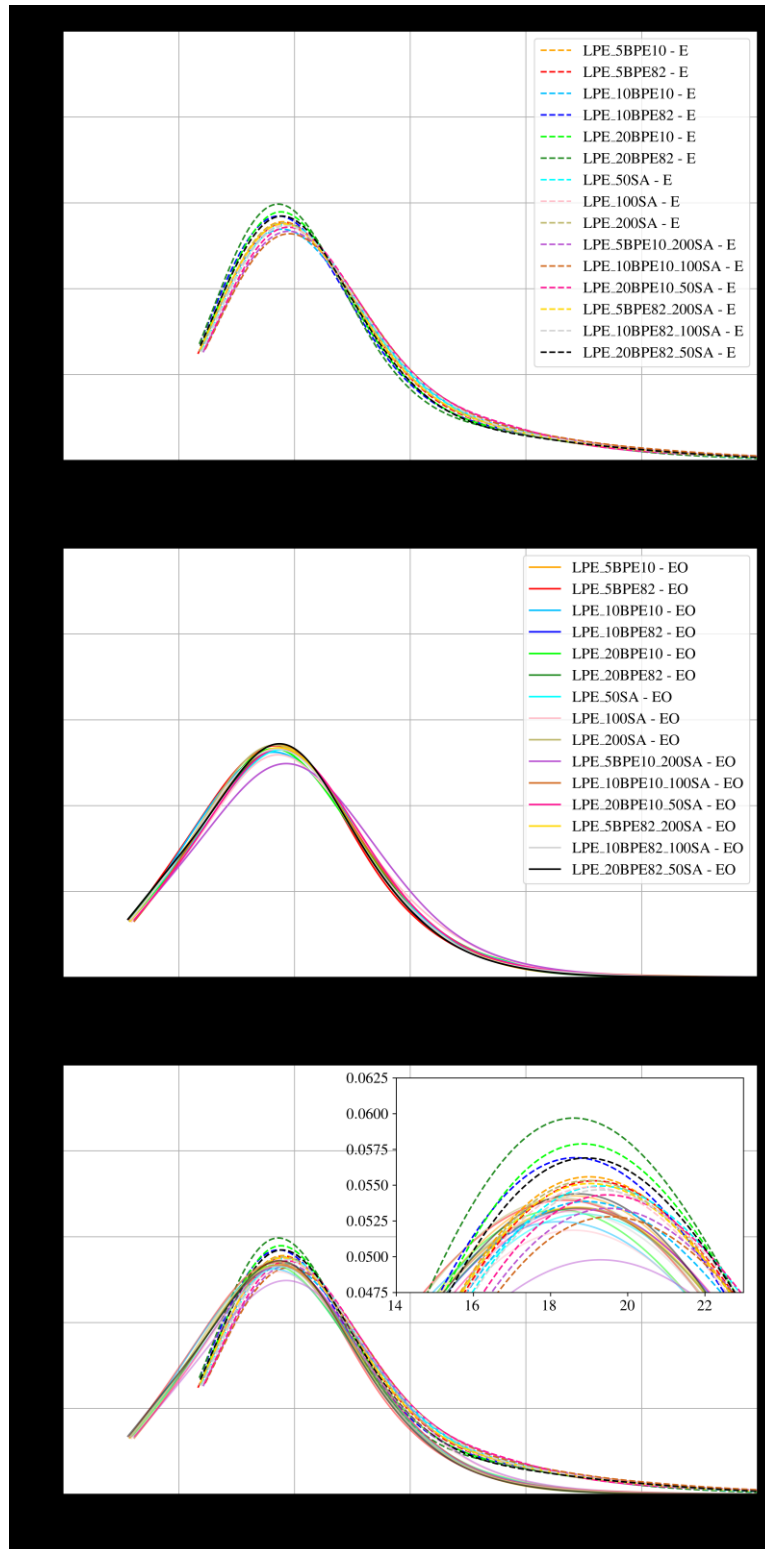


**Figure 30.** The probability distributions of free volume hole size ( $v$ ) around (a) E-segment, (b) EO-segment and (c) E-segment and EO-segment together.

Figure 29 shows the averaged probability distributions of free volume hole size of LPE, BPE, NE, for systems 10 to 15 in Table 6. Since the probability distributions for these four molecules is similar, the average plot is represented in Figure 29. In Figure 29, it is interesting to note that branched molecules such as BPE and SA as well as NE (no branches) possess significant fractions of relatively smaller ( $< 10 \text{ \AA}^3$ ) and relatively larger ( $> 30 \text{ \AA}^3$ ) free volume holes compared to LPE. Figure 30 shows in detail the probability distributions of the E-segment and EO-segment's free volume hole sizes. The figure clearly shows that there are larger free volume holes associated with the E-segments than the EO-segments and that the peaks of the E-segments located at  $\sim 18 \text{ \AA}^3$  are slightly higher than those of EO-segments. Both BPE and SA seem to increase the fraction of large free volume holes around NE, especially on the E-segments.

Figure 31 shows the volume around the constituent atoms of NE at the last snapshot of the MD trajectories of all fifteen systems used. It is obvious that the volume associated with the terminal atom on the E-segment of NE is the largest for all systems. This leads to the observation that E-segments, compared to EO-segments, have larger volume around them as seen in Figure 30. However, it can be seen in Figure 31 that the amplitudes of the volume variations around the EO-segments are larger than those of the E-segments. This is consistent with the fact that EO- volume curves are wider than those of the E-segments shown in Figure 30.

**Table 7.** The number of frequency modes of the coalescing free volume holes around different parts of the NE molecule.

System	E-terminal ( $v_{fNE_{21}} + v_{fNE_{22}}$ )	E ( $v_{fNE_{18}} + v_{fNE_{19}}$ )	NE-middle ( $v_{fNE_{14}} + v_{fNE_{15}}$ )	EO ( $v_{fNE_7} + v_{fNE_8}$ )	EO-terminal ( $v_{fNE_2} + v_{fNE_3}$ )
LPE_5BPE10	17	7	8	11	48
LPE_10BPE10	19	19	5	15	39
LPE_20BPE10	13	12	5	8	28
LPE_5BPE82	22	14	11	13	40
LPE_10BPE82	18	19	8	9	33
LPE_20BPE82	19	8	17	7	29
LPE_50SA	17	14	10	4	38
LPE_100SA	18	12	12	9	35
LPE_200SA	16	14	9	9	37
LPE_5BPE10_200SA	25	12	13	16	23
LPE_10BPE10_100SA	15	12	11	13	44
LPE_20BPE10_50SA	20	15	10	14	35
LPE_5BPE82_200SA	28	7	8	11	35
LPE_10BPE82_100SA	18	16	18	5	27
LPE_20BPE82_50SA	15	10	6	14	36
Summation	280	191	151	158	527

**Table 8.** The power of fluctuations for the coalescing free volume of different beads NE molecule.

System type	E-terminal ( $v_{fNE_{21}} + v_{fNE_{22}}$ )	E ( $v_{fNE_{18}} + v_{fNE_{19}}$ )	NE-middle ( $v_{fNE_{14}} + v_{fNE_{15}}$ )	EO ( $v_{fNE_7} + v_{fNE_8}$ )	EO-terminal ( $v_{fNE_2} + v_{fNE_3}$ )
LPE_5BPE10	3,836	1,502	1,534	4,700	12,793
LPE_10BPE10	4,498	4,077	901	4,636	10,058
LPE_20BPE10	2,847	2,732	948	4,214	6,607
LPE_5BPE82	5,154	3,122	2,241	2,559	10,650
LPE_10BPE82	3,787	3,938	1,801	3,015	7,892
LPE_20BPE82	4,329	1,682	2,449	4,906	6,681
LPE_50SA	4,462	2,695	2,102	3,806	8,764
LPE_100SA	3,855	2,657	2,364	2,883	8,563
LPE_200SA	3,746	3,089	1,944	6,370	8,912
LPE_5BPE10_200SA	5,101	2,800	2,424	2,684	6,048
LPE_10BPE10_100SA	3,295	2,416	2,021	2,233	11,410
LPE_20BPE10_50SA	4,135	3,031	1,945	4,399	9,366
LPE_5BPE82_200SA	6,042	1,763	1,509	2,819	10,068
LPE_10BPE82_100SA	5,068	3,215	3,310	3,230	5,706
LPE_20BPE82_50SA	3,178	2,166	1,008	2,708	9,197
Summation	63,332	40,884	28,500	55,167	132,714

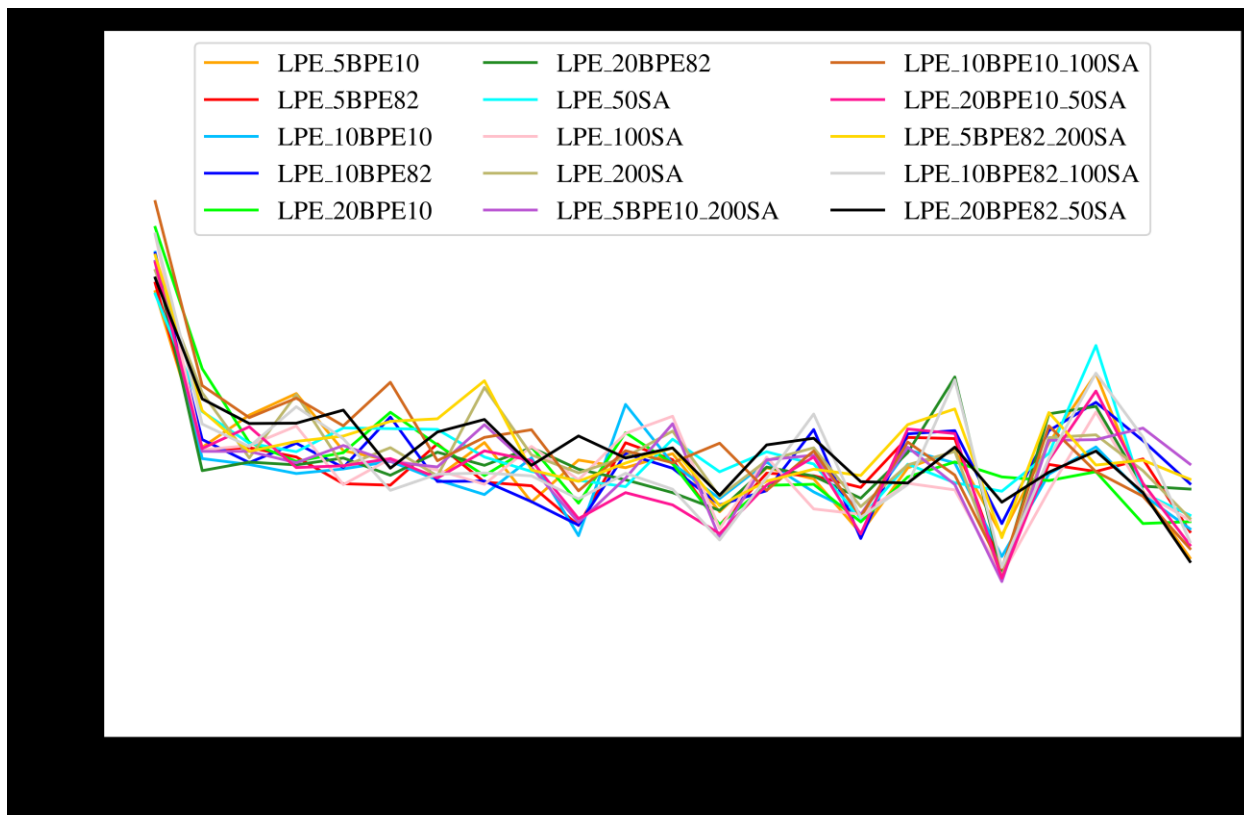


**Figure 31.** The volume around the constituent atoms of NE molecule (see Figure 25 for the atomic indices) obtained from the last snapshot of the MD trajectories of all fifteen systems use

### 4.3.2. Free Volume Holes Coalescence Dynamics

The coalescence of nearby free volume holes around different parts of NE molecules such as EO-terminal ( $v_{fNE_2} + v_{fNE_3}$ ), EO ( $v_{fNE_7} + v_{fNE_8}$ ), NE-middle ( $v_{fNE_{14}} + v_{fNE_{15}}$ ), E ( $v_{fNE_{18}} + v_{fNE_{19}}$ ) and E-terminal ( $v_{fNE_{21}} + v_{fNE_{22}}$ ) were calculated using the free volume data over the last 80 ns of all simulation trajectories. Since the terminal atom in EO-segment is hydrogen while the terminal atom in the E-segment is carbon, we did not include those two terminal atoms in the calculation. Data on the free volume fluctuations (coalescence dynamics) was transformed into Fourier modes

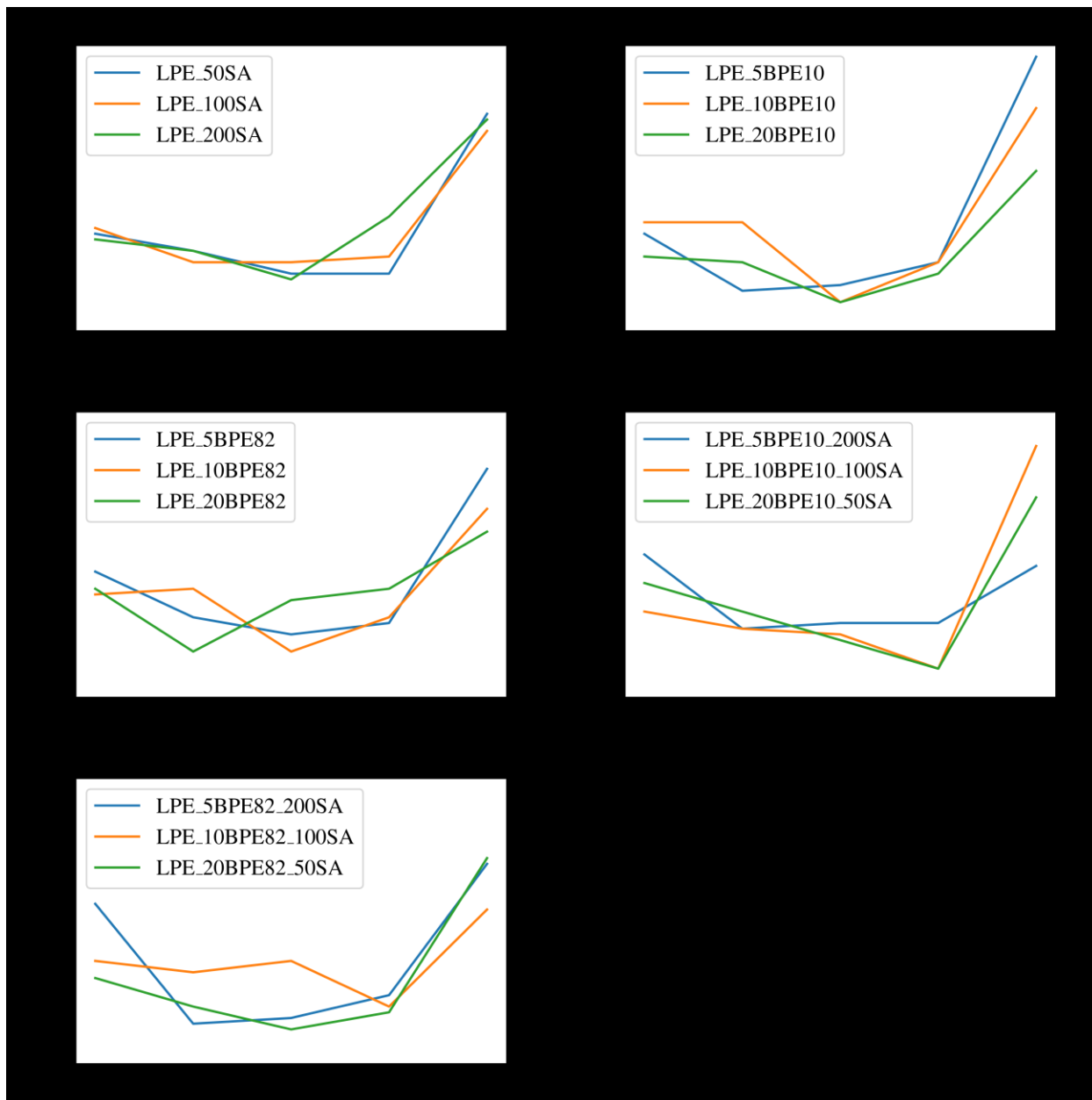
and the corresponding mode intensities were calculated. Our previous work suggests that using a filter of 150 on the intensities is appropriate [135]. The results are summarized in Table 7 and Table 8 and graphically shown in Figure 32 and Figure 33. The Fourier transform formulation is explained in (3-1) to (3-3).

Figure 32 and Figure 33 clearly show that EO-terminals ( $v_{fNE_2} + v_{fNE_3}$ ) exhibit the highest number of Fourier modes and intensity of fluctuations (power) than other parts of NE and that the middle part of NE the lowest coalescence activity. Respective sums of the Fourier modes and power of the EO-segments of all PE blends are almost 65% higher than those of E-segments. It is noteworthy that in our previous work, we reported that the E-segments exhibit higher coalescence activity than EO-segments. This is because we only compared the coalescence activities of the middle part of the E- (i.e., ( $v_{fNE_{18}} + v_{fNE_{19}}$ )) and EO-segments (i.e., ( $v_{fNE_6} + v_{fNE_7}$ )) in neat PE. The data of Figure 29, Figure 30 and Figure 31 shows an interesting behavior of NE in PE blends in the absence and presence of SA; that is, the hydrophobic end of NE has much larger free volume holes than its hydrophilic end but the hydrophilic end exhibits more free volume coalescence activities as quantified by a higher number of Fourier modes and more power.

Nevertheless, the dynamic data show that BPE branches reduce the free volume coalescence activities around NE in the PE blends. This observation is similar to that of neat BPE as reported in our previous work [26]. It is believed that such observation suppresses the formation of larger free volume holes (cavitation) around NE. However, SA seems to exhibit an opposite concentration effect. In other words, SA branches intensify the free volume coalescence activity, especially on EO-segments, thereby increasing the chance of forming larger free volume holes

around NE. The behavior of SA seems to be in line with the experimental observation that addition of a small molecules with multiple terminals to LPE system decreases the time of LPE to ESC failure (i.e., decreasing ESCR) [131]. We are aware that cavitation is only the first step of ESC and that ESC is a multifactor, complex phenomenon. Examination of the free volume coalescence dynamics around a surface-active agent (NE in this particular case) as studied by MD simulation seems to provide a simple approach for predicting ESC behavior.

Considering these results, it seems that, the EO-segment may be more responsible to aggregate free volume, even though it has lesser free volume than E-segment (Figure 30). This could be due to the fact that the hydrophobic groups of LPE, BPE and SA cannot interact well with EO-segment (due to hydrophilic/hydrophobic interaction). Therefore, this segment, would have more free time to aggregate free volume around itself. On the other hand, by adding BPE to the system, since the branched polymer act like a blender in the mixture, by moving all the molecules, forces EO-segments to engage in more interactions with other molecules in its surrounding environment. Therefore, the EO-segment would have less free time to aggregate free volume. It also could be seen in RDF and free volume hole distributions results, that by adding different molecule types, the behavior of EO-segments, compared to E-segment, experiences least amount of changes.



**Figure 32.** The number of Fourier modes vs. location points in NE molecules: EO-terminal ( $v_{fNE_2} + v_{fNE_3}$ ), EO ( $v_{fNE_{10}} + v_{fC_{\#11}}$ ), NE-middle ( $v_{fNE_{14}} + v_{fNE_{15}}$ ), E ( $v_{fNE_{18}} + v_{fNE_{19}}$ ) and E-terminal ( $v_{fNE_{21}} + v_{fNE_{22}}$ ).

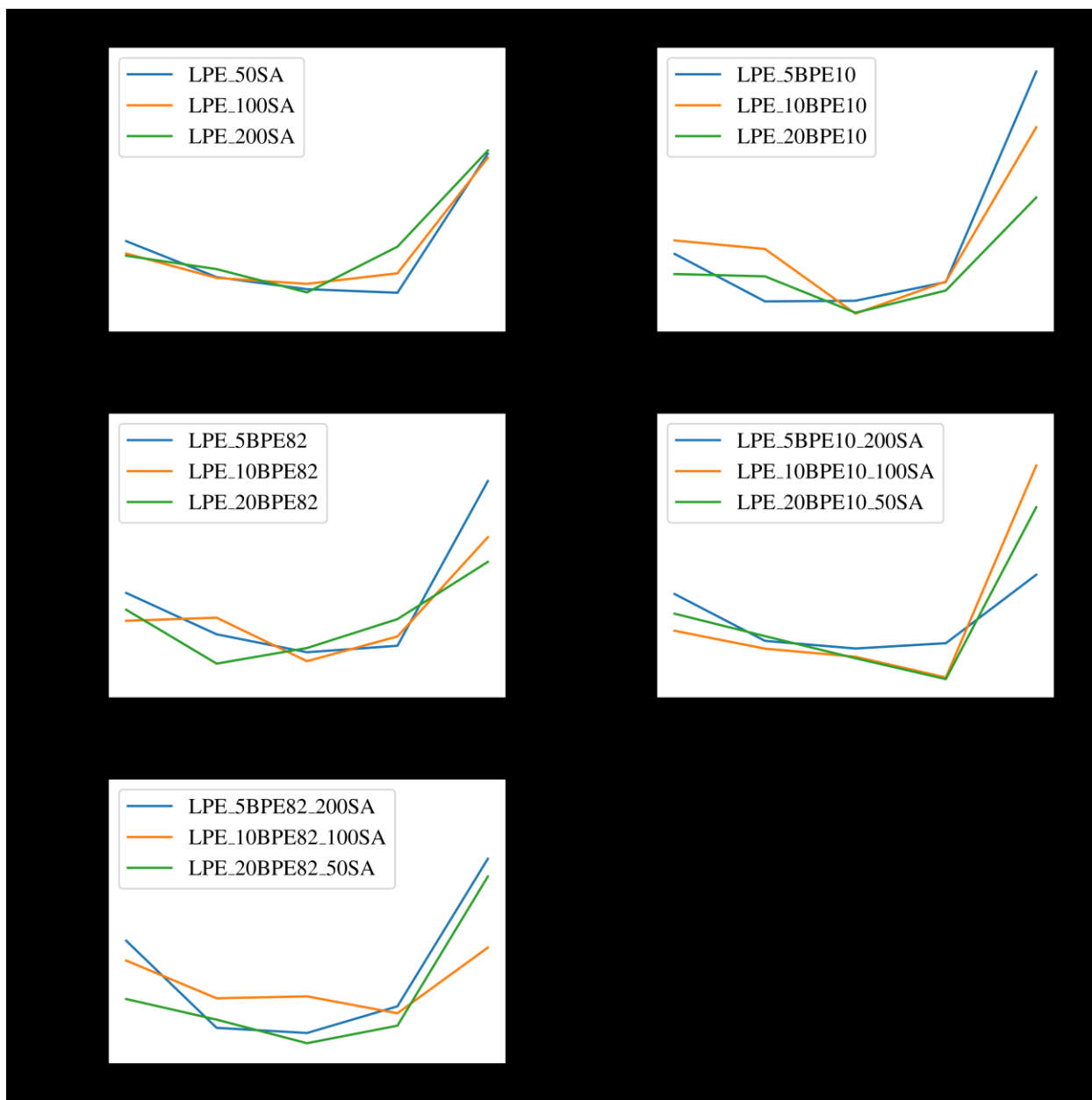


**Figure 33.** The power of fluctuations vs. location points in NE molecules: EO-terminal ( $v_{fNE_2} + v_{fNE_3}$ ), EO ( $v_{fNE_{10}} + v_{fC_{\#11}}$ ), NE-middle ( $v_{fNE_{14}} + v_{fNE_{15}}$ ), E ( $v_{fNE_{18}} + v_{fNE_{19}}$ ) and E-terminal ( $v_{fNE_{21}} + v_{fNE_{22}}$ ).

## 4.4. Conclusion

In this paper, we used molecular dynamics simulation to study effects of blending LPE with BPE and size of backbone to which hexyl branches attached on the free volume size distribution and coalescence dynamics around NE, a surface-active (ESC) agent. The BPE used had a backbone of 500 carbons and contained 10 and 82 SCBs/1,000 carbons while SA's backbone had only 4 carbons and contained 4 hexyl branches. The RDF results showed that an "optimal" branch concentration (within the concentration range of BPE of interest) exists in the PE blends to maximize the interaction between the BPE branches and NE. On the other hand, there exists an "optimal" branch concentration (within the concentration range of SA of interest) to minimize the interaction between the SA branches and NE. The aforementioned results suggest that branches of BPE and SA, with comparable sizes but attached to backbones with significantly different sizes, behave differently in terms of interacting with NE. The results showed that the hydrophobic end of NE has larger free volume holes while the hydrophilic end of NE tend to a larger variation in size of free volume holes. The coalescence dynamics results indicated that hexyl branches of BPE suppress the formation of larger free volume holes while those of SA enhance it, especially on the hydrophilic end of NE. It is expected that addition of hexyl branches attached a long backbone may slow down cavitation while this is not the case for the hexyl branches attached to a short backbone.

## 4.5. Acknowledgments

The authors gratefully acknowledge the financial support from Imperial Oil through the IOL University Research Awards program. This study was also enabled by the high-performance computing resources provided by WestGrid, Compute Canada ([www.computecanada.ca](http://www.computecanada.ca)).

# Chapter 5: Effect Functionalizing the Branch-ends with Vinyl Acetate

\*Version of this chapter's sections has been submitted in: Kavyani S., and Choi P., Molecular Dynamics Study of Free Volume Coalescence around Nonyl Ethoxylate in Polyethylene with Vinyl Acetate Modified Branches. *Polymer Science & Engineering*, 2024.

---

## 5.1. Introduction

Polyethylene is a widely used polymer known for its excellent mechanical properties, chemical resistance, and durability [136], [137]. However, polyethylene is susceptible to a phenomenon called environmental stress cracking (ESC) when exposed to certain environmental conditions [53], [113]. Implications of ESC in polyethylene for industries such as oil and gas, packaging, construction, and automotive are profound, as polyethylene-based products are extensively used. ESC of polyethylene refers to the process of crack initiation and propagation in the material that leads to fracture when it is exposed to ESC agent and subjected to mechanical stresses concurrently. The crack initiation process could be divided in to three sub-stages *a*) cavitation (void formation), *b*) craze initiation, *c*) crack growth.

According to the branching characteristics of the macromolecules, polyethylene can be categorized as low-density polyethylene (LDPE), high-density polyethylene (HDPE), and linear low-density polyethylene (LLDPE). Each type may exhibit varying degrees of susceptibility to ESC [48], [49]. The susceptibility of polyethylene to ESC is influenced by factors such as the polymer's molecular weight ( $M_w$ ) [41], [42], [44], [52], cooling rates during processing [138], branch distribution [38], [139] and the nature of the environment the polymer is exposed to [51]. Exposure to chemicals such as detergents, alcohols, oxidizing agents, and certain solvents can trigger ESC in polyethylene. Additionally, environmental factors like UV radiation [140], temperature variations [13], [46], and mechanical stresses [46] can contribute to crack formation and propagation.

The ESC Resistance (ESCR) of a polymer indicates its capacity to withstand the slow crack growth (SCG) throughout its intended lifespan [39], [40]. One of the main parameters that has been shown to help improve ESCR of PE is the branches in the macromolecular structure of PE. PEs with longer branches exhibit higher ESCR. As it was found that by increasing the number of carbons in short chain branches (SCBs) from 2 to 6, ESCR increases [49]. Bubeck *et al.* [45] examined how the number and length of SCBs impact the ESCR of PE. Their findings revealed that by increasing both the number and length of SCBs in PE, the ESCR can be enhanced. Krishnaswamy *et al.* studied the time to failure of different PE mixtures with SCBs placed exclusively on either the “short” or the “long” chains of binary blends [131] and demonstrated that the presence of SCBs has a significantly greater impact on the time to failure compared to the effect of molecular weight. Specifically, they observed that placing SCBs on the longer chains resulted in superior performance in terms of time to failure. Lustiger *et al.* [5] discovered that

SCBs contribute to enhanced ESCR in PE materials by reducing the crystallinity of the material, increasing the number of tie-molecules, thereby minimizing their tendency to slip past each other.

The addition of copolymer ethylene vinyl acetate (EVA) to LDPE has been commercially utilized to improve ERSC, toughness, film tear resistance, flexibility and optical properties [141]. It was mentioned that by increasing the VA percentage of EVA and also the  $M_w$  of EVA, the ESCR of EVA would increase [142]. Alothman [143] studied the effect of VA percentage of EVA (6.5 and 27 wt%) and of the concentration of EVA in HDPE/EVA blend (0, 5, 20, 40 and 100 wt% of EVA) on the thermal, fracture toughness, mechanical, and rheology of the blends. Vinyl acetate in EVA introduces chemical bonds and structural changes in the polymer chain that affects the physio-mechanical properties of the PE [144]–[146]. Chen [147] studied the effect of EVA copolymer on HDPE/EVA and LDPE/EVA Blends. The EVA used in Chen's work contained 18 wt% of VA. He reported that for both HDPE and LDPE, the presence of EVA improved the ESCR of the PE material, where the improvement for LDPE/EVA was greater. Borisova and Kressler [148] investigated the LLDPE blends with the addition of random copolymers of ethylene and vinyl acetate (LLDPE/EVA), with a EVA having 28 wt% VA and the LLDPE/EVA blends with 1.8, 3.6, 5.4, 7.1 and 8.9 wt% of EVA. They reported that the LLDPE/EVA with 8.9 wt% did not fail during the ESC test, indicating that EVA are capable of slowing the crack propagation in the LLDPE material.

Understanding the behavior and properties of polymers at the molecular level is crucial for designing and optimizing their performance. Molecular dynamics (MD) simulation is a powerful computational technique that enables the study of the dynamics and thermodynamics of polymer

systems at the atomistic scale. One of the key advantages of MD simulation is its ability to capture the atomistic details and dynamic processes that are otherwise difficult to access experimentally. By providing insights into the local and global structure of polymers, MD simulation can help elucidate the relationships between molecular structure and material properties. Most recently, we have used MD simulation to show that an ESC agent enhances free volume coalescence around it and that SCBs slow down free volume coalescence [135]. It is worth noting that free volume coalescence is a short time scale process while cavitation is a much longer time scale process. However, we believe that cavitation starts with free volume coalescence and that slow cavitation increases ESCR.

Free volume refers to the empty spaces or voids within a polymer material at the molecular level. These voids exist between polymer chains and are essential in governing several key properties, including mechanical, thermal, and transport properties [132]. The presence of free volume influences factors such as polymer chain mobility, diffusion rates, and the ability to accommodate stress and deformation [112], [133], [134]. Changes in free volume can lead to significant alterations in the overall behavior and properties of polymers. Given the hypothesis that we proposed in our previous work that free volume coalescence leads to cavitation [135], we furthered our MD simulation to study if SCBs chemically modified by VA groups would slow down the free volume coalescence process of PE with different branching characteristics. As mentioned, PE and PE blends containing VA have been experimentally observed to exhibit higher ESCR.

## **5.2. Molecular Dynamics (MD) Simulations**

GROMACS 2020.4 software package [117], [118], a widely used software package for molecular dynamics (MD) simulations of biomolecules, polymers, and other complex systems, was used in this work. GROMACS provides a comprehensive set of tools and algorithms specifically designed for efficient and accurate simulations of molecular systems. The Transferable Potentials for Phase Equilibria (TraPPE) force field was used to describe the potential energy and the forces between particles. TraPPE employs a united atom force field, treating hydrogen atoms in  $CH_x$  implicitly by combining the entire  $CH_x$  moiety into a single united atom [87]. TraPPE has shown to be effective in capturing the influence of both SCBs and LCBs on the topological properties of PE melt [95], impact of SCBs on the interlamellar structure of LLDPE [94], [95], effect of chain length on the diffusivity of PE [112] and effect of SCBs on the ESC of PE, in the presence of an ESC agent [135].

The simulation unit cell of each simulation was set to  $\sim 15 \times 15 \times 15 \text{ nm}^3$  initially and all of the molecules were inserted into the simulation unit cell randomly. Temperature and pressure of each unit cell were controlled at 190 °C by velocity-rescaling (v-rescale) thermostat [120] and at 1 bar by Parrinello-Rahman barostat [75], respectively. Here, the choice of 190 °C, a temperature at which PE is in the melt state, is explained in our previous work [135]. In particular, it helps equilibrate the systems of interest that is not accessible at room temperature.

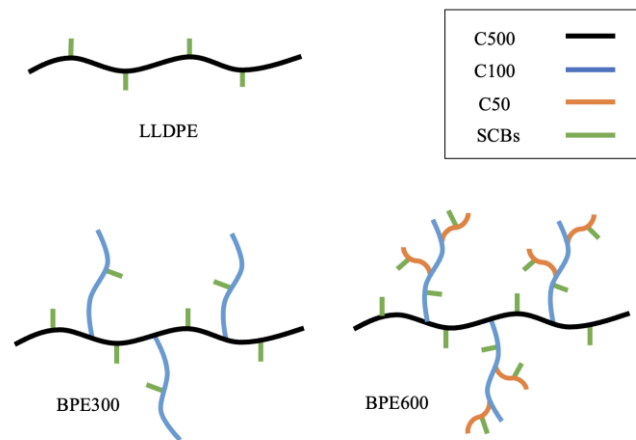


**Figure 34.** Different macromolecular structures of PE used in this work.

The production runs of all simulation unit cells were carried out for at least 530 *ns*, with a time step of 2 *fs*. The last 30 *ns* were used for data analysis. For all coordinates of *x*, *y* and *z*, the periodic boundary conditions were used. The neighbour search frequency update was set to 5 steps. The Particle Mesh Ewald (PME) method was used to calculate the electrostatic forces between charged particles [65].

In order to generate the amorphous unit cells, the steps shown below were followed.

- i)* Five nonyl ethoxylate molecules were randomly distributed in an empty simulation unit cell of size  $\sim 15 \times 15 \times 15 \text{ nm}^3$
- ii)* Distributed the PE molecules, randomly, to fill the unit cells
- iii)* Carried out multiple steps of energy minimization on the unit cells to reach the minimum force  $< 10 \text{ kJ mol}^{-1} \text{ nm}^{-1}$  in each unit cell
- iv)* NVT with leap-frog algorithm, a timestep of 0.5 fs, for 1 ns
- v)* NPT, with leap-frog algorithm, a timestep of 0.1 fs, for 5 ns
- vi)* NPT, with leap-frog algorithm, a timestep of 0.5 fs, for 5 ns
- vii)* NPT, with leap-frog algorithm, a timestep of 2 fs, for 5 ns
- viii)* The production run with leap-frog algorithm

As mentioned, three different types of PE structures were used in this work, with different branch contents (see Figure 34). The SCBs are with the length of four and seven carbon atoms with branch contents of 10 and 82 SCBs/1,000 backbone (BB) carbon atoms. In some PE models, branch ends are chemically modified to vinyl acetate (VA) (see Figure 35) [149]. Nonyl ethoxylate (NE) rather than nonyl phenol ethoxylate (NPE) (a common ESC agent [121], [122] known by its trademark name *Igepal* [35], [123]), was used as the TraPPE force field does not provide adequate parameters for the phenol moiety in NPE. Figure 35 shows the molecular structure of NE and the numbering of the carbon atoms in it. NE obviously contains the hydrophobic ethylene-segment (E-segment) and the hydrophilic ethylene oxide-segment (EO-segment) and was used in our previous work [135]. The concentration of NE molecules was kept constant in all simulations to five NE molecules per unit cell. The Voronoi tessellation method was used to calculate the free volume around each atom in the systems [135]. Voronoi tessellation (VT) is a method used to partition a space into regions surrounding each set of particles [104]. In order to utilize the Voronoi algorithm, the pyvoro Python package [107] which relies on the voro++ library [108]–[110], an open-source software library, was used. After establishing the volume of Voronoi cells containing individual particles, the free volume space assigned to each particle at each timestep can be calculated by subtracting the hard-core (HC) volume of each particle from the determined volume (i.e.,  $V_{free} = V_{Voronoi\ cell} - V_{hc}$ ). This enables the evaluation of the free volume assigned to each particle throughout the process.

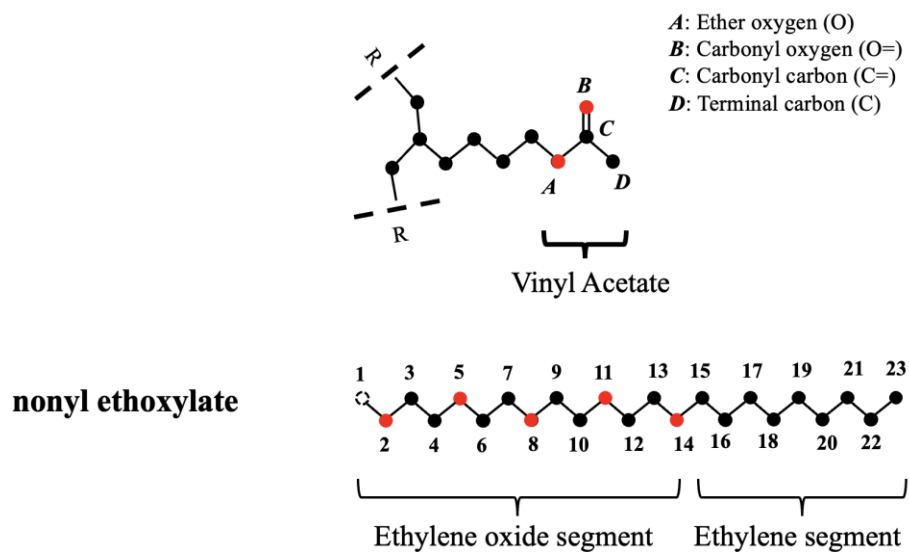


**Figure 35.** The chemical structures of a VA branch terminal and nonyl ethoxylate. The black, red and white dots signify carbon, oxygen and hydrogen atoms, respectively.

**Table 9.** Descriptions of the Simulated Systems

System Name	Number of PE molecules in the box	PE structure	Branch content (SCBs/1,000 BB carbons)	Percentage of VA branch terminals	wt% of VA
LLDPE_10VA0	35	LLDPE	10	0	0
LLDPE_10VA20	35	LLDPE	10	20	0.3
LLDPE_10VA40	35	LLDPE	10	40	0.6
LLDPE_10VA60	35	LLDPE	10	60	0.9
LLDPE_82VA0	28	LLDPE	82	0	0
LLDPE_82VA20	26	LLDPE	82	20	0.8
LLDPE_82VA40	25	LLDPE	82	40	1.6
LLDPE_82VA60	24	LLDPE	82	60	2.4
BPE300_10VA0	22	BPE300	10	0	0
BPE300_10VA20	22	BPE300	10	20	0.2
BPE300_10VA40	22	BPE300	10	40	0.4
BPE300_10VA60	21	BPE300	10	60	0.6
BPE300_82VA0	17	BPE300	82	0	0
BPE300_82VA20	17	BPE300	82	20	0.8
BPE300_82VA40	16	BPE300	82	40	1.6
BPE300_82VA60	16	BPE300	82	60	2.4
BPE300_82VA100	15	BPE300	82	100	7.9
BPE600_10VA0	16	BPE600	10	0	0
BPE600_10VA20	16	BPE600	10	20	0.3
BPE600_10VA40	16	BPE600	10	40	0.6
BPE600_10VA60	15	BPE600	10	60	0.9
B7PE300_82VA0	16	BPE300	10	60	0

All simulation systems are shown in Table 9. The nomenclature of the systems:  $\{PE\}$   $\{structure\}$   $\{branch\ content\}$   $\{number\ of\ VA\ branch\ terminals\}$ . It is noteworthy that the numbers of VA branch terminals and the corresponding weight concentrations of VA were chosen to be comparable with experimental results. The SCBs in all systems have four carbon atoms, except the model system B7PE300\_82VA0, where the branches have seven carbon atoms. The addition of it is to check if the observed VA effect is attributed to its chemical structure or VA's branch length (seven branch backbone atoms). Here, the results of B7PE300\_82VA0 will be compared with those of BPE300\_82VA100. The BPE600\_10VA(0-60) model systems were included to study whether longer branches to which SCBs with VA terminals are attached would influence their interaction with NE.

## 5.3. Results and Discussion

### 5.3.1. Intermolecular Radial Distribution Functions

Previous work suggested that free volume coalescence, thereby cavitation, likely takes place at the PE-NE interfaces [30]. We hereby examine their intermolecular radial distribution functions (RDFs) as they characterize local molecular packings. In the same manner as it is discussed in Chapter 2, the RDFs were evaluated using [64]

$$\begin{aligned}
 g_{AB}(r) &= \frac{\langle \rho_B(r) \rangle}{\langle \rho_B \rangle} \\
 &= \frac{1}{\langle \rho_B \rangle} \frac{1}{N_A} \sum_{i \in A} \sum_{j \in B} \frac{\delta(r_{ij} - r)}{4\pi r^2}
 \end{aligned} \tag{5-1}$$

where  $N_A$  and  $N_B$  are the numbers of particles A and B, respectively. Also,  $\langle \rho_B(r) \rangle$  is the average particle density of type B particles at a distance  $r$  from particles A;  $\langle \rho_B \rangle$  is the bulk density of particles B.

Figure 36 shows the PE RDFs by using E- and EO-segments as references, respectively. It is obvious that packings between PE and NE are not sensitive to the length of backbone to which SCBs are attached as well as the branch content of PE.

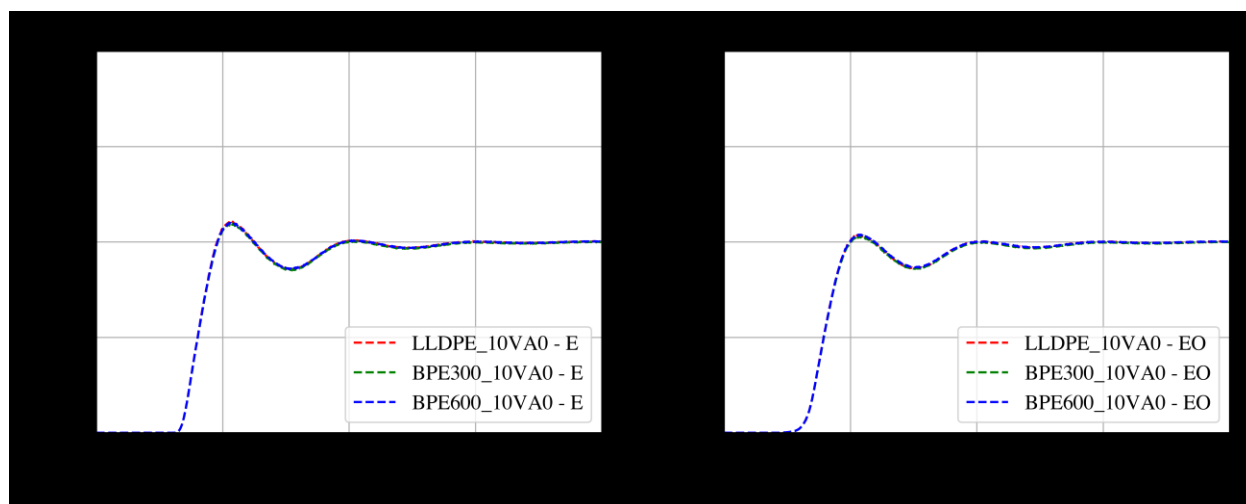


**Figure 36.** Radial distribution functions (RDF) of PE models as determined by using (a) E-segments and (b) EO-segments as references, respectively. PE models used were LLDPE, BPE300 and BPE600.

The RDFs of carbons in the backbones, branches, butyl branch ends and branch ends chemically modified by VA, as calculated using E- and EO-segments of NE as references, are plotted in Figure 37 and Figure 38, respectively. The two figures show clearly that regardless of the macromolecular structure of PE, butyl branch ends and VA branch ends exhibit strong affinity for both E- and EO-segments of NE. However, owing to the hydrophilic nature of the ether and carbonyl moieties in the VA branch ends, VA branch ends show stronger affinity to interact with EO-segments compared to E-segments. Interestingly, RDF values, using E-segments as the

references, decrease slightly with increasing VA concentration for all three branched PE models but those using EO-segments are more or less insensitive to the VA concentration except VA branch ends in BPE300 with 10 SCBs that exhibit an inverse VA concentration dependence. It is not clear as to what causes this behavior.

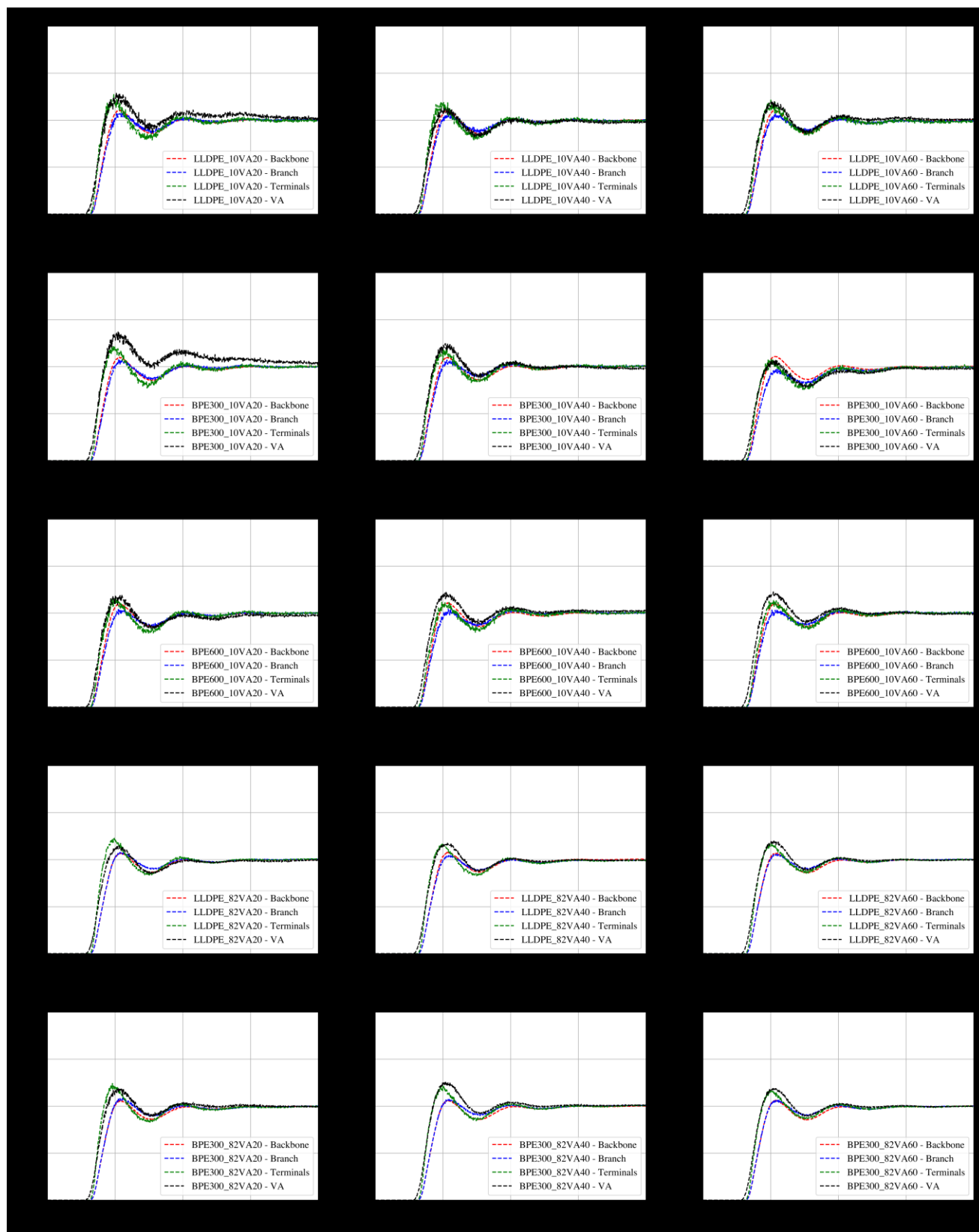


**Figure 37.** Radial distribution functions (RDFs) of various types of carbons in branched PE models as determined by using E-segments as references.

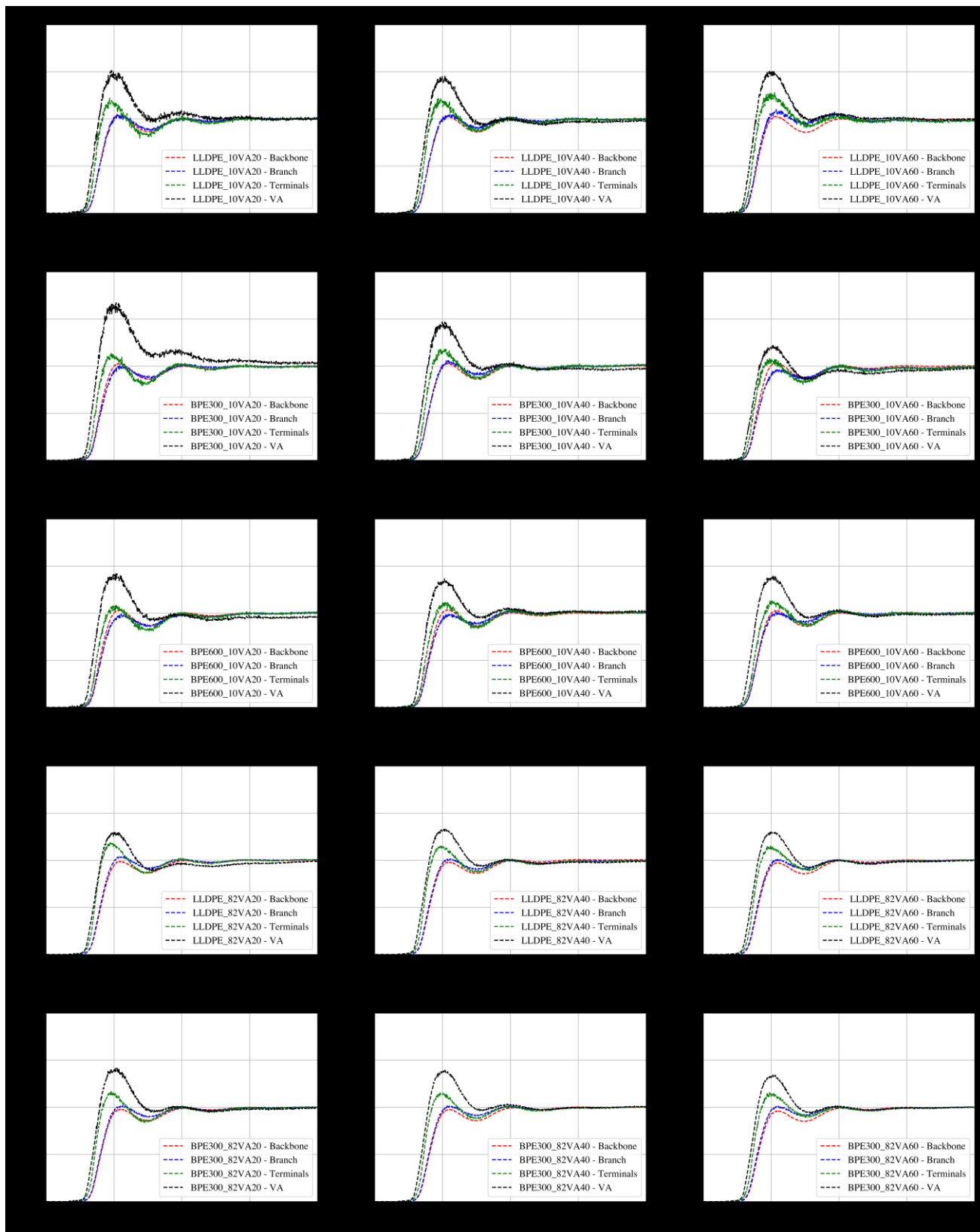


**Figure 38.** Radial distribution functions (RDFs) of various types of carbons in branched PE models as determined by using EO-segments as references.

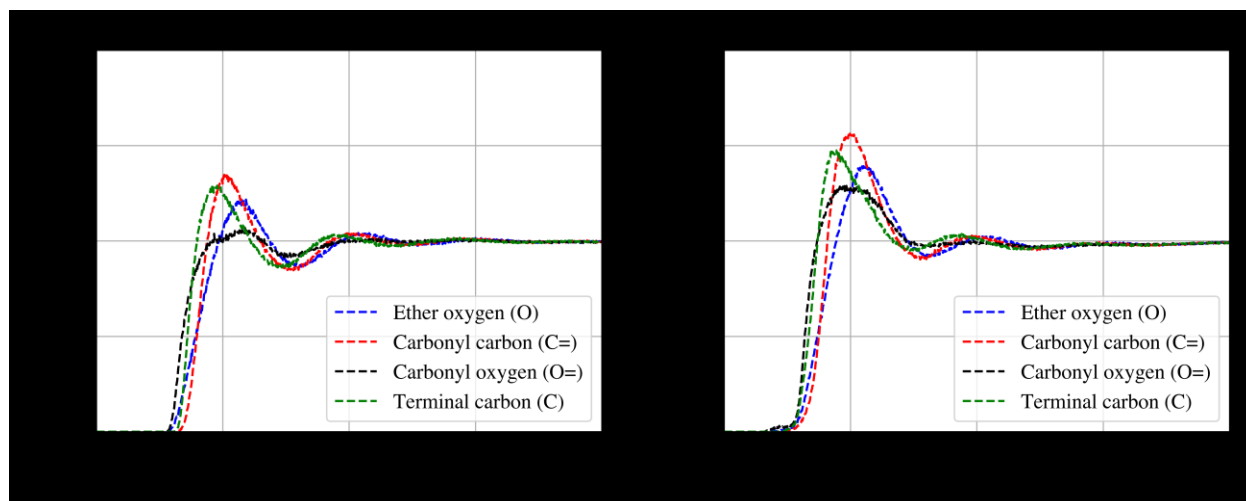


**Figure 39.** Radial distribution functions (RDFs) of atoms in VA (see Figure 40) averaged over all PE models (a) E-segments and (b) EO-segments as references.

The average RDFs of different constituent atoms (i.e., ether oxygen  $O$ , carbonyl carbon  $C=$ , carbonyl oxygen  $O=$  and terminal carbon  $C$  of VA as defined in Figure 35) were calculated and are plotted in Figure 39. It clearly shows that the carbonyl and terminal carbons exhibit strong affinity for the EO-segments than the E-segments. Here, the carbonyl carbon has a fairly large point charge with the value of  $+0.55$  which drives it toward the ether moieties of the EO-segments.

The RDF of B7PE300\_82VA0 and BPE300\_82VA100 were calculated and are plotted in Figure 41, referenced by E-segments (Figure 41a, b) and EO-segments (Figure 41c, d). This figure shows that the attraction between VA branch ends and both E- and EO-segments is not due to its branch length. Indeed, the methyl group in the alkyl branches exhibit higher RDF values than the terminal carbons in the VA functionalized branch ends.

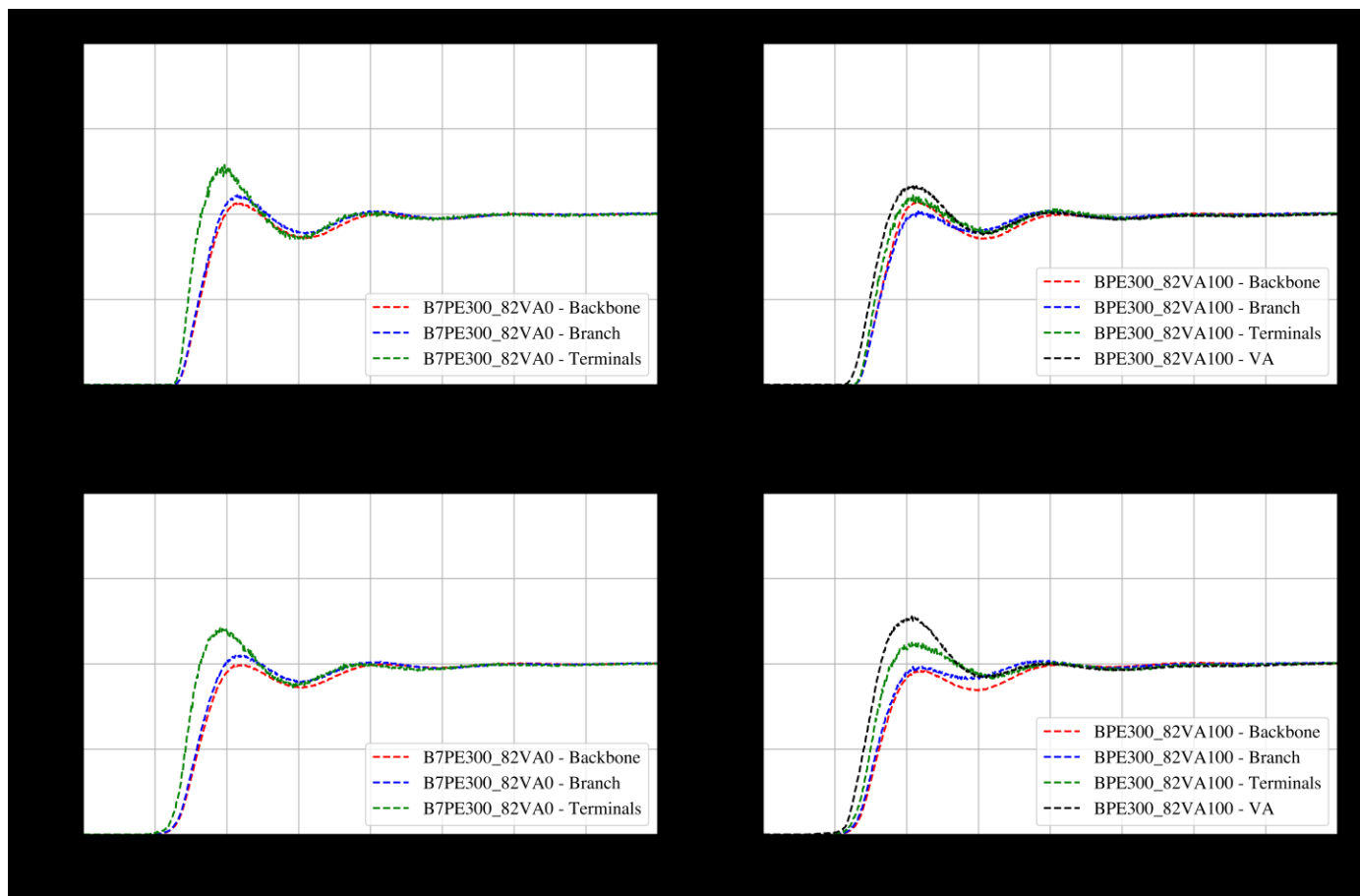


**Figure 41.** The radial distribution functions of different chemical moieties on the branches as referenced by E-segments (a, b) and EO-segments (c, d).

The free volume hole size ( $v$ ) distributions around the VA functionalized branch ends in various polyethylene models are plotted in Figure 42. The distributions are bimodal. It is essentially attributed to the fact that the free volume size around the carbonyl carbon is small while this is not the case for the three neighboring atoms (i.e., carbonyl oxygen, ether oxygen and terminal carbon) (see Figure 43). This is somewhat expected as the carbonyl carbon is the only atom that is attached to three atoms in VA. Figure 43 shows that the free volume terminal carbon (C) and carbonyl oxygen (O=) is very high which shows that the VA molecules are very mobile.

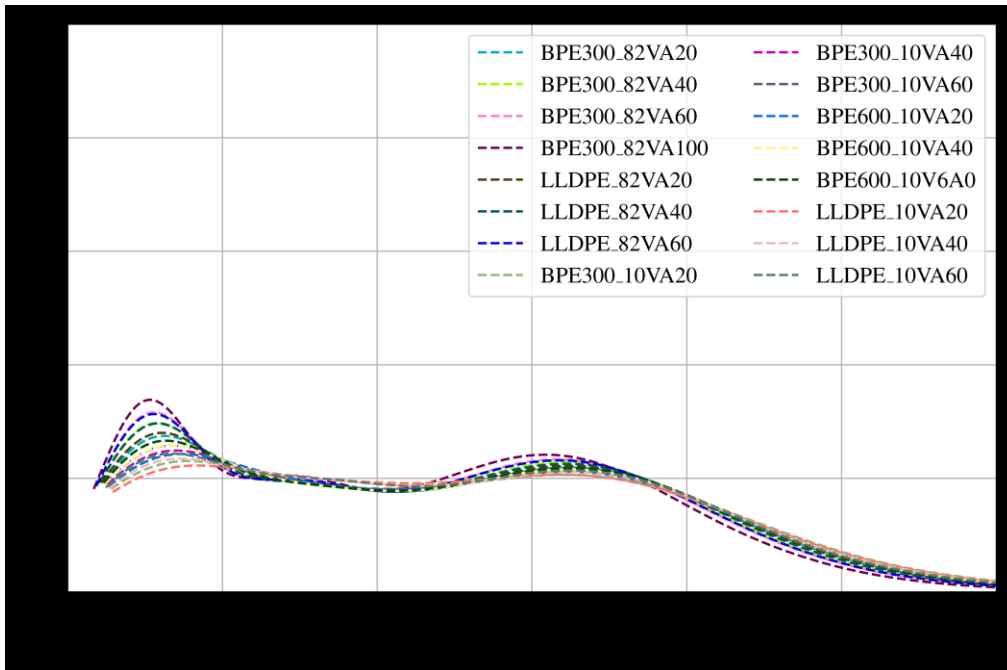


**Figure 42.** The free volume hole size ( $v$ ) distributions for VA.

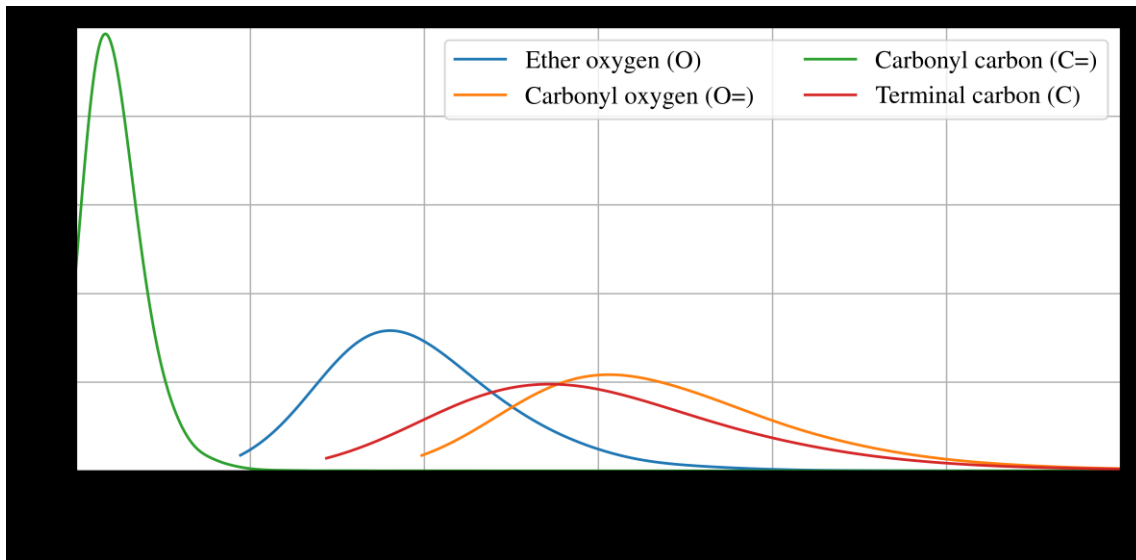


**Figure 43.** The free volume hole size ( $v$ ) distributions for different VA atoms: ether oxygen  $O$ , carbonyl carbon  $C=$ , carbonyl oxygen  $O=$  and terminal  $C$ .

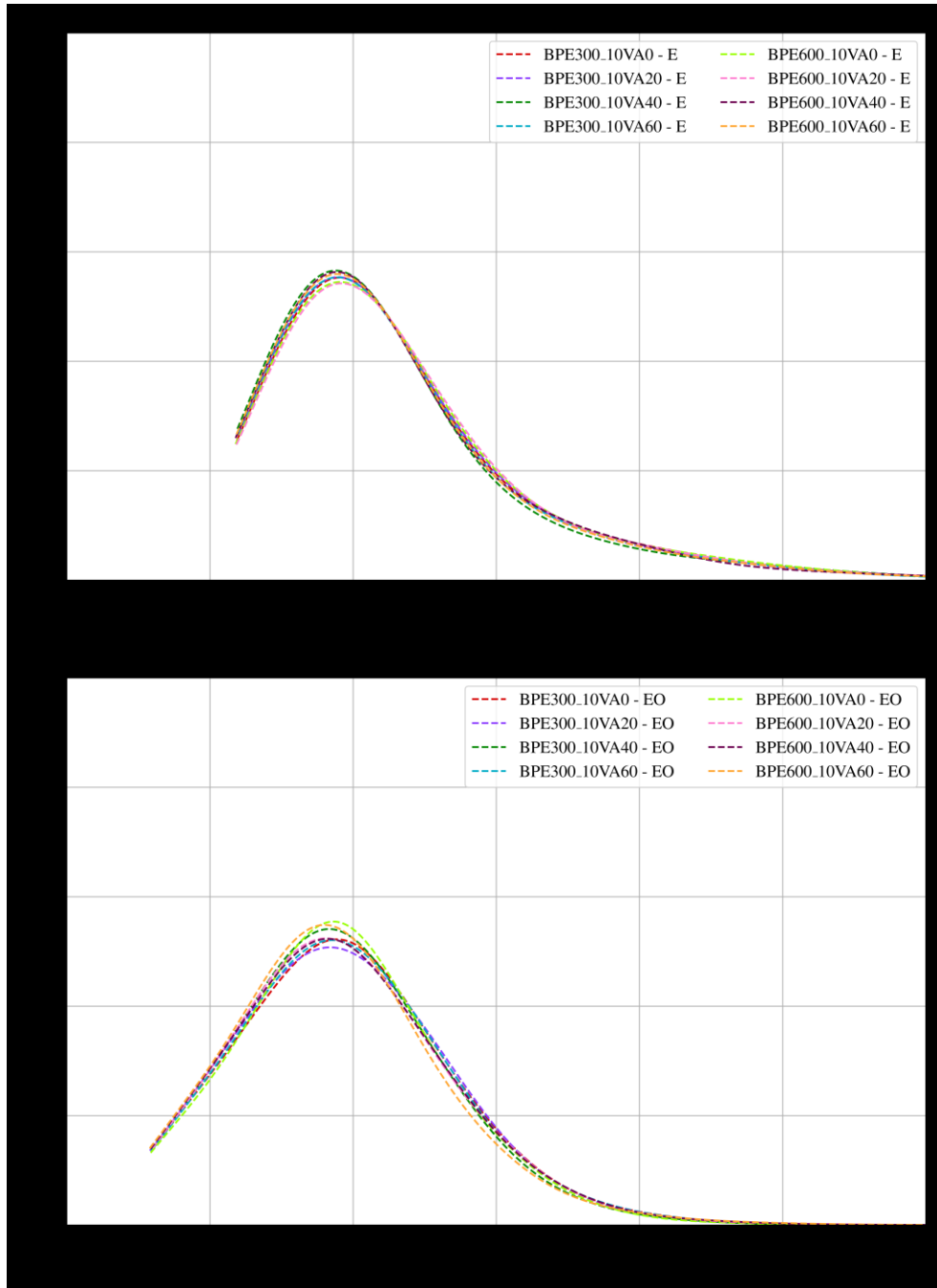


**Figure 44.** The free volume hole size ( $v$ ) distributions for (a) E-segments and (b) EO-segments, for different VA contents. For clarity, only the plots of BPE300 and BPE600, are shown.

We further examine the characteristics of the free volume around E- and EO-segments of NE (see Figure 44). Since the results of the high branch content models (Table 6) are similar to those with low branch contents, only the results of the low branch content models are shown. In particular, Figure 44 shows that all free volume holes around the E-segments are larger than  $10 \text{ \AA}^3$  and the distributions show a long tail while a small fraction of the free volume holes around the EO-segments are smaller than  $10 \text{ \AA}^3$  and the distributions show a shorter tail. In other words, free volume holes around E-segments are larger than the EO-segments. Figure 44 also indicates that generally, by increasing the VA content, the free volume distribution slightly shifts to the left, where the effect for the EO-segments is slightly stronger than E-segments.

Further investigation of the free volume hole size of the entire NE molecule yielded Figure 45 that corresponds to the free volume data in the last 20 snapshots of BPE300\_10VA20. All other polyethylene models show similar behavior. Therefore, their results are not shown here. Figure 45 clearly indicates that only the terminal methyl moieties in E-segments have much larger free volume holes around them than the methylene carbons. This may explain the long tail observed in Figure 44a. Figure 45 also shows that the free volume fluctuations of all atoms in the EO-segments are significantly higher than those in the E-segments, suggesting that there are more free volume coalescence activities around the EO-segments.

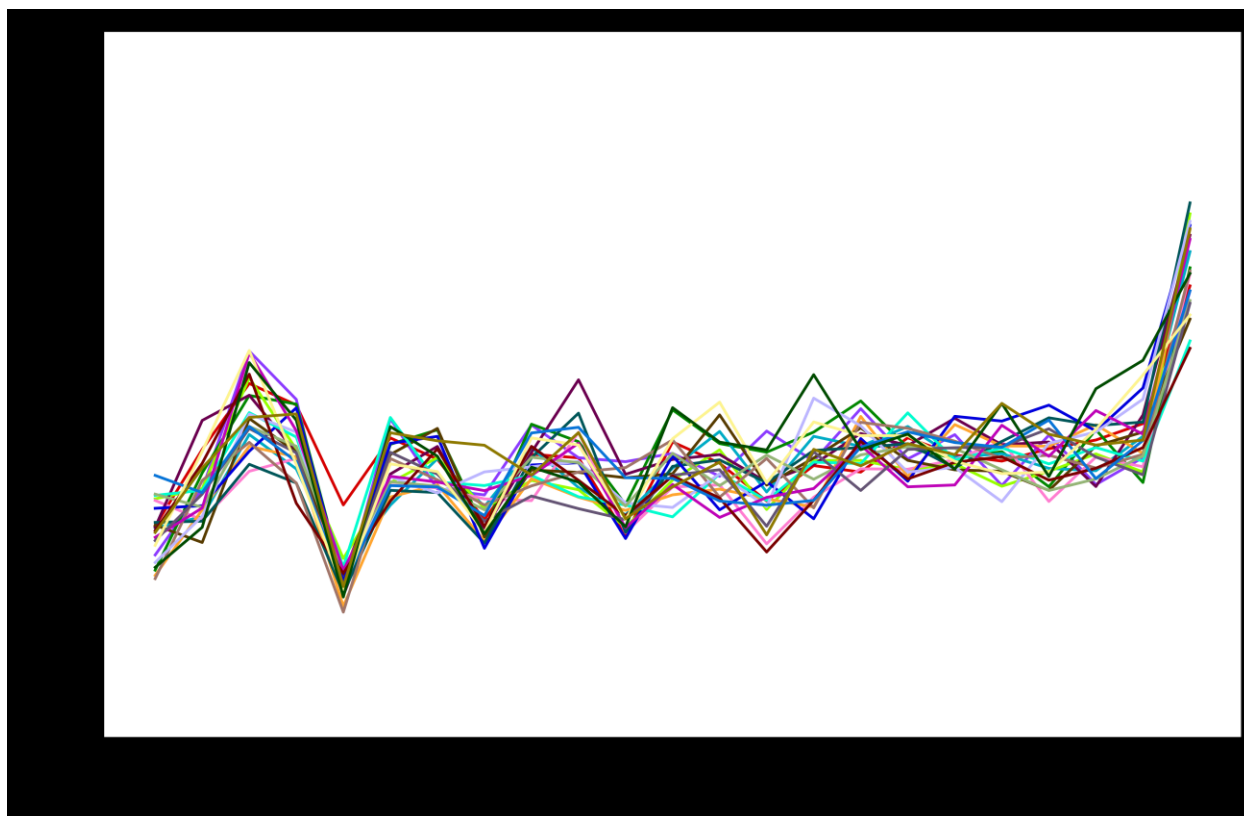


**Figure 45.** The free volume fluctuations of skeletal atoms in the NE molecules from the last 20 snapshots of the MD trajectory for BPE300\_10VA20.

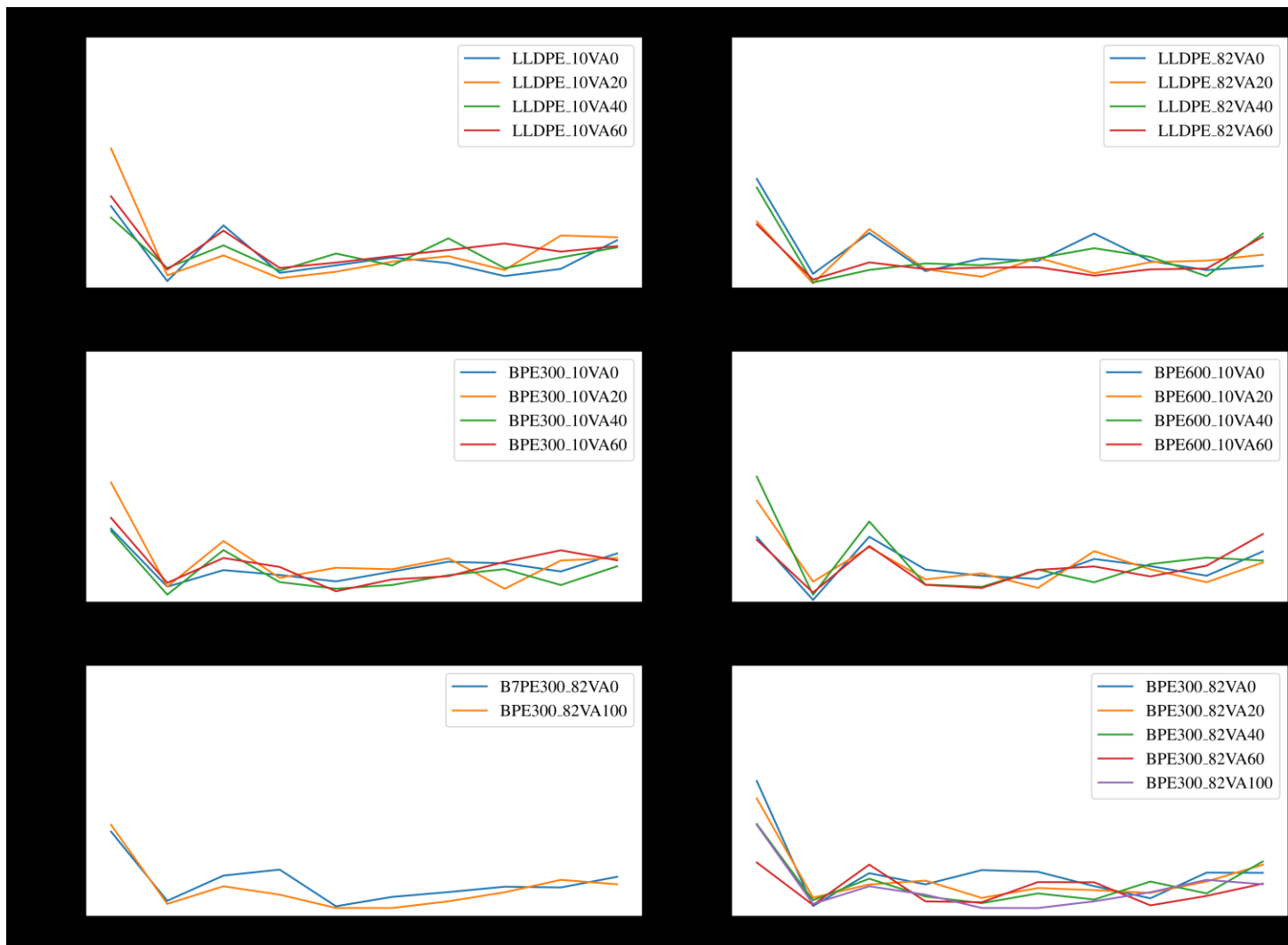
### 5.3.2. Coalescence Dynamics

Figure 45 indicates that the fluctuations of the free volume around the EO-segments are higher than E-segments. In order to further study this observation, the free volume coalescence dynamics around NE molecules was analysed. To quantify the free volume coalescence dynamics around NE molecules, we determined the time evolution of free volume hole size of two neighboring atoms in the sequence of ( $\{v_{fNE_2} + v_{fNE_3}\}, \{v_{fNE_4} + v_{fNE_5}\}, \{v_{fNE_6} + v_{fNE_7}\}, \dots$  and  $\{v_{fNE_{21}} + v_{fNE_{22}}\}$ ). It is noteworthy that the terminal atom of E- and EO-segments are carbon and hydrogen, respectively. For the comparison purpose, we neglected the terminal atoms of the two segments in

the coalescence dynamics calculations. This is because the free volume coalescence should happen along the entire E- or EO-segment, not just at one atom at the branch ends. Fourier transforms of such time series data yielded the power (amplitude) of the free volume fluctuations. The Fourier transform formulation is explained in equations (3-1) to (3-3).

Figure 46 summarizes the calculated powers of various pairs of neighboring atoms of NE molecules in all polyethylene models. It is interesting to note that the  $\{v_{fNE_2} + v_{fNE_3}\}$  atom pairs of EO-segments exhibit a much higher power (i.e., coalescence activities) than all other pairs. By summing the power of fluctuations in each E- and EO-segment in Figure 46 and taking average over different systems, the results show that on average, the fluctuations of free volume coalescence of the entire EO-segments are about 64.0% more than those of the E-segments, where per atom-pair, the power of fluctuations in EO-segments is ~10% more than E-segments. Also, comparison of the power of fluctuations of EO-segment of VA20s, VA40s and VA60s, to VA0, the power of fluctuations is 2, 12 and 16% less than VA0, respectively,  $(100 \times \frac{power_{VAx} - power_{VA0}}{power_{VA0}}, x = 20, 40 \text{ and } 60)$ . Results for E-segments are 2, 1 and 4%. These results clearly show that by increasing the VA content in the PE polymer, the power of fluctuations around EO-segments is mostly affected compared to the E-segments. Another way of capturing the effect of VA is to calculate the power of fluctuations of EO-segments relative to that of the E-segments  $(100 \times \frac{power_{EO} - power_E}{power_E})$ . Over the range of 0 – 60% of VA, the power of fluctuations of EO-segments are 85, 75, 60 and 46% higher than that of E-segments. All the above analysis shows that by increasing the VA content in the PE models, the power of fluctuations for free volume coalescence of the EO-segments decreases significantly. It seems to be in line with the

experimental results mentioned in the introduction section that addition of EVA to polyethylene helps improve its ESCR.



**Figure 46.** The power of the fluctuations of free volume coalescence for different atom pairs of the NE molecules.

## 5.4. Conclusion

In this work, we used molecular dynamics (MD) simulation to investigate how vinyl acetate (VA) functionalized branch ends affect the free volumes coalescence dynamics around an amphiphilic environmental stress cracking (ESC) agent namely nonyl ethoxylate (NE) in the amorphous phase of three polyethylene models with different branching characteristics. The results indicate that VA branch ends slowed down the free volume coalescence dynamics as quantified by the power (amplitude) of fluctuations around the NE molecules, especially the EO-segments. The effect became more pronounced with increasing VA concentration. Since it is hypothesized that free volume coalescence leads to cavitation, the first step of ESC, the present results suggest that cavitation in ESC may start around the hydrophilic segments (EO-segments) of the amphiphilic (NE) molecules and that the presence of VA branch ends reduces the cavitation initiation. The VA concentration results seem to be in line with experimental observation that increasing the VA content of EVA that is added to polyethylene helps enhance its environmental stress crack resistance (ESCR). The current results further corroborate the idea that free volume coalescence may be used to determine effect of short chain branches on ESC.

## 5.5. Acknowledgments

The authors gratefully acknowledge the financial support from Imperial Oil through the IOL University Research Awards program. This study was also enabled by the high-performance computing resources provided by WestGrid, Compute Canada ([www.computecanada.ca](http://www.computecanada.ca)).

# Chapter 6: Conclusions and Future Perspective

---

## 6.1. Overall conclusions

In conclusion, our MD simulations delved into the intricate molecular morphology and dynamics associated with free volumes in cavitation, the first step of ESC, in polyethylene systems. The first investigation focused on LPE and BPE with varying short-chain branch concentrations, exploring the influence of the ESC agent, NE, on packing and free volume coalescence in [PE]-[NE] interface. We found that NE had minimal impact on the packings of LPE and BPE chains, with short-chain branches in BPE suppressing free volume coalescence at the [PE]-[NE] interfaces, potentially mitigating cavitation initiation. This proposed a different perspective based on the free volume concept, on the cavitation, the very first step of ESC.

In the second exploration, we employed MD simulations and the free volume concept to gain molecular insights into cavitation initiation. The coalescence of free volume was identified as a key factor in initiating cavitation, suggesting that cavitation may commence at the hydrophilic head of the ESC agent. Short-chain branches were found to interrupt free volume coalescence, proposing a hypothesis that stronger interactions between the ESC agent's hydrophilic head and the surrounding environment reduce coalescence and, consequently, cavitation. Branch

concentration in polyethylene blends and the interaction between BPE branches and NE were highlighted, revealing distinct behaviors based on branch sizes and attachment to different backbone sizes. Where was shown that the branches on larger backbones have less power in their fluctuation of free volume coalescence.

In the third investigation, we extended our study to examine the impact of VA functionalized branch ends on free volume coalescence dynamics around NE in various PE systems. The results indicated that VA branch ends slowed down free volume coalescence dynamics, particularly around the hydrophilic segments of NE, supporting the hypothesis that VA reduces cavitation initiation. The concentration-dependent effect of VA aligns with experimental observations in EVA blends, where increased VA content enhances ESCR. Collectively, these findings underscore the role of free volume coalescence in determining the impact of short-chain branches and their terminal functional groups on ESC and provide molecular-level insights that contribute to a deeper understanding of ESC phenomena.

In summary, our comprehensive MD simulations shed light on the molecular mechanisms underlying ESC initiation, proposing novel insights based on the interplay between polyethylene structures, ESC agents, and environmental conditions. These findings not only advance our fundamental understanding of ESC but also offer valuable guidance for the design and optimization of polyethylene materials with enhanced ESC resistance.

## **6.2. Future Perspective**

One of the main outcomes of the presented results was that the branches could help mitigate cavitation and potentially enhance ESCR because of their very high mobility. Since all of the

simulated systems were in the amorphous phase, it seems that by keeping the branches in the amorphous phase, and not the crystalline structure, one could not only maintain the crystalline structure of the polymer but also, at the same time, increase the ESCR of the polymer. To achieve this, one possible solution would be using block copolymers.

The results also show that the terminals of the branches play an even more profound role in suppressing cavitation. Functionalizing the terminals of the branches with various groups would be very beneficial, especially with functional groups that tend to interact better with the hydrophilic head of the ESC agent. Namely, groups such as ester/acetate, carboxyl, acryl, ether, and possibly amine groups.

Moreover, a significant result arising from this investigation is the potential prediction of ESC, a phenomenon unfolding over an extended period of time, through computational methods, particularly computational chemistry, in the foreseeable future. Given the progress in computational and technological capabilities, breaking down ESC into smaller sequential steps allows for the advancement of understanding each facet of ESC through computational methods. Through this approach, the prospect of predicting ESC using computational methods becomes increasingly attainable.

# Bibliography

---

- [1] Y. Zhang, P.-Y. Ben Jar, S. Xue, L. Han, and L. Li, “Measurement of Environmental Stress Cracking Resistance of Polyethylene Pipe: A Review,” in *ASME Asia Pacific Pipeline Conference*, 2019, vol. 58912.
- [2] S. Bandyopadhyay and H. R. Brown, “Environmental stress cracking and morphology of polyethylene,” *Polymer (Guildf.)*, vol. 19, no. 5, pp. 589–592, 1978, doi: 10.1016/0032-3861(78)90287-2.
- [3] J. B. P. Soares, R. F. Abbott, and J. D. Kim, “Environmental Stress Cracking Resistance of Polyethylene: The Use of CRYSTAF and SEC to Establish Structure–Property Relationships,” *J. Polym. Sci., Part B*, vol. 38, no. 10, pp. 1267–1275, 2000, doi: 10.1002/(SICI)1099-0488(20000515)38:10<1267::AID-POLB10>3.0.CO;2-5.
- [4] S. Ghosh, V. P. S. Rana, V. Kain, V. Mittal, and S. K. Baveja, “Role of residual stresses induced by industrial fabrication on stress corrosion cracking susceptibility of austenitic stainless steel,” *Mater. Des.*, vol. 32, no. 7, pp. 3823–3831, 2011, doi: 10.1016/j.matdes.2011.03.012.
- [5] J. J. Cheng, M. A. Polak, and A. Penlidis, “A tensile strain hardening test indicator of environmental stress cracking resistance,” *J. Macromol. Sci. Pure Appl. Chem.*, vol. 45, no.

- 8, pp. 599–611, 2008, doi: 10.1080/10601320802168728.
- [6] F. T. Richards and M. L. Foster, “Primary and secondary containment of hazardous substances in cold regions with HDPE liner,” *Soc. Pet. Eng.*, pp. 169–172, 1991, doi: 10.2523/22072-ms.
- [7] P. L. Soni and P. H. Geil, “Environmental stress cracking of polyethylene: temperature effect,” *J. Appl. Polym. Sci.*, vol. 23, no. 4, pp. 1167–1179, 1979.
- [8] C. J. Singleton, E. Roche, and P. H. Geil, “Environmental stress cracking of polyethylene,” *J. Appl. Polym. Sci.*, vol. 21, no. 9, pp. 2319–2340, 1977, doi: 10.1002/app.1977.070210904.
- [9] D. C. Wright and R. T. Limited., *Failure of plastics and rubber products : causes, effects, and case studies involving degradation*. Shawbury, Shrewsbury, Shropshire: Rapra Technology, 2001.
- [10] T. Dooher, A. Saifullah, J. Ullah, C. Magee, A. Mulholland, and D. Dixon, “Environmental stress cracking of polymers: Case studies from industry (ABS and LDPE),” *Eng. Fail. Anal.*, vol. 138, 2022, doi: 10.1016/j.engfailanal.2022.106120.
- [11] R. Communication, “Investigation of the resistance to environmental stress crack of high density polyethylene parts,” *Polymer (Guildf)*, vol. 61, no. 11, pp. 850–854, 2016.
- [12] R. Ayyer, A. Hiltner, and E. Baer, “A fatigue-to-creep correlation in air for application to environmental stress cracking of polyethylene,” *J. Mater. Sci.*, vol. 42, no. 16, pp. 7004–7015, 2007, doi: 10.1007/s10853-006-1108-2.
- [13] S. Ebnesajjad, *Effect of Chemicals on Plastics*. Elsevier Inc.
- [14] J. Lai and A. Bakker, “Analysis of the non-linear creep of high-density polyethylene,”

- Polymer (Guildf.)*, vol. 36, no. 1, pp. 93–99, 1995, doi: 10.1016/0032-3861(95)90680-Z.
- [15] M. Amjadi and A. Fatemi, “Creep and fatigue behaviors of High-Density Polyethylene (HDPE): Effects of temperature, mean stress, frequency, and processing technique,” *Int. J. Fatigue*, vol. 141, no. May, p. 105871, 2020, doi: 10.1016/j.ijfatigue.2020.105871.
- [16] M. Parsons, E. V. Stepanov, A. Hiltner, and E. Baer, “Effect of strain rate on stepwise fatigue and creep slow crack growth in high density polyethylene,” *J. Mater. Sci.*, vol. 35, no. 8, pp. 1857–1866, 2000, doi: 10.1023/A:1004741713514.
- [17] B. P. Russell, K. Karthikeyan, V. S. Deshpande, and N. A. Fleck, “The high strain rate response of Ultra High Molecular-weight Polyethylene: From fibre to laminate,” *Int. J. Impact Eng.*, vol. 60, pp. 1–9, 2013, doi: 10.1016/j.ijimpeng.2013.03.010.
- [18] A. L. Bowman *et al.*, “Free volume and internal structural evolution during creep in model amorphous polyethylene by Molecular Dynamics simulations,” *Polymer (Guildf.)*, vol. 170, no. February, pp. 85–100, 2019, doi: 10.1016/j.polymer.2019.02.060.
- [19] M. Thuy, U. Niebergall, H. Oehler, I. Alig, and M. Böhning, “Evaluation of the damaging effect of crop protection formulations on high density polyethylene using the Full Notch Creep Test,” *Polymer (Guildf.)*, vol. 228, no. May, 2021, doi: 10.1016/j.polymer.2021.123853.
- [20] B. T. P. Yin, S. E. Lovell, and J. D. Ferry, “VISCOELASTIC PROPERTIES OF POLYETHYLENE RUBBER-LIKE STATE \*,” *J. Phys. Chem.*, vol. 65, no. 3, pp. 534–538, 1961.
- [21] Y. Li, X. Sun, S. Zhang, and S. Han, “A fractal crazing constitutive model of glassy polymers considering damage and toughening,” *Eng. Fract. Mech.*, vol. 267, no. February,

- p. 108354, 2022, doi: 10.1016/j.engfracmech.2022.108354.
- [22] H. H. Kausch and G. H. Michler, “The effect of time on crazing and fracture,” *Adv. Polym. Sci.*, vol. 187, no. October, pp. 1–33, 2005, doi: 10.1007/b136954.
- [23] J. W. Wee, Y. Zhao, and B. H. Choi, “Observation and modeling of environmental stress cracking behaviors of high crystalline polypropylene due to scent oils,” *Polym. Test.*, vol. 48, pp. 206–214, 2015, doi: 10.1016/j.polymertesting.2015.10.011.
- [24] H. B. H. Hamouda, M. Simoes-betbeder, F. Grillon, P. Blouet, N. Billon, and R. Piques, “Creep damage mechanisms in polyethylene gas pipes,” *Polymer (Guildf.)*, vol. 42, no. 12, pp. 5425–5437, 2001, doi: 10.1016/S0032-3861(00)00490-0.
- [25] J. M. Lagarón, J. M. Pastor, and B. J. Kip, “Role of an active environment of use in an environmental stress crack resistance (ESCR) test in stretched polyethylene: A vibrational spectroscopy and a SEM study,” *Polymer (Guildf.)*, vol. 40, no. 7, pp. 1629–1636, 1999, doi: 10.1016/S0032-3861(98)00406-6.
- [26] H. R. Brown, “A theory of the environmental stress cracking of polyethylene,” *Polymer (Guildf.)*, vol. 19, no. 10, pp. 1186–1188, 1978, doi: 10.1016/0032-3861(78)90069-1.
- [27] A. Lustiger and R. D. Corneliussen, “The role of crazes in the crack growth of polyethylene,” *J. Mater. Sci.*, vol. 22, no. 7, pp. 2470–2476, 1987, doi: 10.1007/BF01082132.
- [28] J. M. Lagarón, N. M. Dixon, D. L. Gerrard, W. Reed, and B. J. Kip, “Cold-drawn material as model material for the environmental stress cracking (ESC) phenomenon in polyethylene. A raman spectroscopy study of molecular stress induced by macroscopic strain in drawn polyethylenes and their relation to environmental stress cr,”

- Macromolecules*, vol. 31, no. 17, pp. 5845–5852, 1998, doi: 10.1021/ma9717606.
- [29] A. Lustiger, R. L. Markham, and M. M. Epstein, “Environmental stress crack growth in low-density polyethylene,” *J. Appl. Polym. Sci.*, vol. 33, no. 3, pp. 117–123, 1978, doi: 10.1002/app.1981.070260327.
- [30] A. Lustiger, “Environmental stress cracking: the phenomenon and its utility.” 1986.
- [31] Javier C. Cruz and Jeffrey A. Jansen, “Environmental stress cracking,” *ASM Handb.*, vol. 11B, p. 104, 2022, doi: 10.1038/265104a0.
- [32] E. T. Teófilo and M. S. Rabello, “The use of acoustic emission technique in the failure analysis of PET by stress cracking,” *Polym. Test.*, vol. 45, pp. 68–75, 2015, doi: 10.1016/j.polymertesting.2015.05.005.
- [33] J. W. Summers, E. B. Rabinovitch, and J. Rodriguez, “Environmental stress cracking of polyvinyl chloride compounds under long- term stress,” *J. Vinyl Technol.*, vol. 15, no. 4, pp. 237–243, 1993, doi: 10.1002/vnl.730150411.
- [34] Y. Ohde and H. Okamoto, “The effect of surfactant solutions on the growth rate of environmental stress cracking of low-density polyethylene,” *J. Mater. Sci.*, vol. 15, no. 6, pp. 1539–1546, 1980, doi: 10.1007/BF00752136.
- [35] A. K. Saad, H. A. Abdulhussain, F. P. C. Gomes, J. Vlachopoulos, and M. R. Thompson, “Studying the mechanism of biodiesel acting as an environmental stress cracking agent with polyethylenes,” *Polymer (Guildf.)*, vol. 191, p. 122278, 2020, doi: 10.1016/j.polymer.2020.122278.
- [36] M. Fleissner, “Experience with a full notch creep test in determining the stress crack performance of polyethylenes,” *Polym Eng Sci*, vol. 38, no. 2, pp. 330–340, 1998.

- [37] S. Shukla and A. Mishra, "Amorphous Polymer Based Nanocomposites for Biosensor Applications," in *Amorphous Materials: New Research*, 2013.
- [38] J. J. Cheng, M. A. Polak, and A. Penlidis, "Influence of micromolecular structure on environmental stress cracking resistance of high density polyethylene," *Tunn. Undergr.*, vol. 26, no. 4, pp. 582–593, 2011, doi: 10.1016/j.tust.2011.02.003.
- [39] R. A. Isaksen, S. Newman, and R. J. Clark, "Mechanism of environmental stress cracking in linear polyethylene," *J. Appl. Polym. Sci.*, vol. 7, no. 2, pp. 515–531, 1963, doi: 10.1002/app.1963.070070210.
- [40] L. Kurelec, M. Teeuwen, H. Schoffeleers, and R. Deblieck, "Strain hardening modulus as a measure of environmental stress crack resistance of high density polyethylene," *Polymer (Guildf.)*, vol. 46, no. 17, pp. 6369–6379, 2005, doi: 10.1016/j.polymer.2005.05.061.
- [41] J. Cazenave, R. Seguela, B. Sixou, and Y. Germain, "Short-term mechanical and structural approaches for the evaluation of polyethylene stress crack resistance," *Polymer (Guildf.)*, vol. 47, no. 11, pp. 3904–3914, 2006, doi: 10.1016/j.polymer.2006.03.094.
- [42] J. N. Herman and J. A. Biesenberger, "Molecular Weight Distribution and Environmental Stress Cracking of Linear Polyethylene," *Polym. Eng. Sci.*, vol. 6, no. 4, pp. 341–348, 1966, doi: 10.1002/pen.760060410.
- [43] S. Bandyopadhyay and H. R. Brown, "Environmental stress cracking of low molecular weight high density polyethylene," *Polymer (Guildf.)*, vol. 22, no. 2, pp. 245–249, 1981, doi: 10.1016/0032-3861(81)90207-X.
- [44] P. Sardashti, A. J. Scott, C. Tzoganakis, M. A. Polak, and A. Penlidis, "Effect of temperature on environmental stress cracking resistance and crystal structure of Polyethylene," *J.*

- Macromol. Sci. Pure Appl. Chem.*, vol. 51, no. 3, pp. 189–202, 2014, doi: 10.1080/10601325.2014.871934.
- [45] R. A. Bubeck and H. M. Baker, “The influence of branch length on the deformation and microstructure of polyethylene,” *Polymer (Guildf.)*, vol. 23, no. 11, pp. 1680–1684, 1982, doi: 10.1016/0032-3861(82)90193-8.
- [46] A. L. Ward, X. Lu, Y. Huang, and N. Brown, “The mechanism of slow crack growth in polyethylene by an environmental stress cracking agent,” *Polymer (Guildf.)*, vol. 32, no. 12, pp. 2172–2178, 1991, doi: 10.1016/0032-3861(91)90043-I.
- [47] Grayline LLC, “Environmental Stress Cracking Resistance of Polyethylene,” *Whitepaper*, p. 120613, 2017.
- [48] M. J. Shirkavand, H. Azizi, I. Ghasemi, and M. Karabi, “Effect of Molecular Structure Parameters on Crystallinity and Environmental Stress Cracking Resistance of High-Density Polyethylene/TiO<sub>2</sub> Nanocomposites,” *Adv. Polym.*, vol. 37, no. 3, pp. 770–777, 2018, doi: 10.1002/adv.21719.
- [49] J. T. Yeh, C. Y. Chen, and H. S. Hong, “Static fatigue behaviour of linear low-density polyethylenes,” *J. Mater. Sci.*, vol. 29, no. 15, pp. 4104–4112, 1994, doi: 10.1007/BF00355978.
- [50] R. A. García, A. Carrero, M. Aroca, O. Prieto, and C. Domínguez, “Slow Crack Growth Resistance in Resin Blends of Chromium and Metallocene Catalyzed Ethylene-Hexene Copolymers for Pipe Applications,” *Polym. Eng. Sci.*, vol. 48, no. 5, pp. 1–10, 2008, doi: 10.1002/pen.
- [51] R. Qian, X. Lu, and N. Brown, “The effect of concentration of an environmental stress

- cracking agent on slow crack growth in polyethylenes,” *Polymer (Guildf)*., vol. 34, no. 22, pp. 4727–4731, 1993, doi: 10.1016/0032-3861(93)90708-I.
- [52] R. Ayyer, A. Hiltner, and E. Baer, “Effect of an environmental stress cracking agent on the mechanism of fatigue and creep in polyethylene,” *J. Mater. Sci.*, vol. 43, no. 18, pp. 6238–6253, 2008, doi: 10.1007/s10853-008-2926-1.
- [53] R. Toggenburger and S. Newman, “The Environmental stress cracking of polyethylene,” *Polym. Lett.*, vol. 2, pp. 7–12, 1964.
- [54] Y. Qin, V. Litvinov, W. Chassé, J. Sun, and Y. Men, “Environmental stress cracking of polyethylene pipe: Changes in physical structures leading to failure,” *Polymer (Guildf)*., vol. 252, p. 124938, 2022, doi: <https://doi.org/10.1016/j.polymer.2022.124938>.
- [55] E. M. Gutman, R. Kalifa, and G. Malik, “Environmental stress cracking of polyethylene pipes for water,” *J. Mater. Sci. Lett.*, vol. 14, pp. 1017–1018, 1995, doi: 10.1007/BF00274636.
- [56] J. P. Dear, N. S. Mason, and M. Poulton, “Environmental stress cracking of polyethylene pipes in water distribution networks,” *Fract. Nano Eng. Mater. Struct. - Proc. 16th Eur. Conf. Fract.*, vol. 10, no. c, pp. 995–996, 2006, doi: 10.1007/1-4020-4972-2\_493.
- [57] L. L. Böhm, H. F. Enderle, and M. Fleißner, “High-density polyethylene pipe resins,” *Adv. Mater.*, vol. 4, no. 3, pp. 234–238, 1992, doi: 10.1002/adma.19920040317.
- [58] D. Munson, T. M. Adams, and S. Hall, “Determination of material damping values for high density polyethylene pipe materials,” *Am. Soc. Mech. Eng. Press. Vessel. Pip. Div. PVP*, vol. 1, pp. 197–215, 2012, doi: 10.1115/PVP2012-78776.
- [59] J. Zheng *et al.*, “A review of nondestructive examination technology for polyethylene pipe

- in nuclear power plant,” *Front. Mech. Eng.*, vol. 13, no. 4, pp. 535–545, 2018, doi: 10.1007/s11465-018-0515-9.
- [60] “Oil guidelines,” *Alberta Government*. <https://www.alberta.ca/oil-guidelines.aspx>.
- [61] M. Charest, “Alkaline-surfactant-polymer (ASP) flooding in Alberta: small amounts of the right chemicals can make a big difference,” *Can Discov Dig*, vol. 1, pp. 20–52, 2013.
- [62] “Highlights of the Alberta Economy,” *Alberta Government*, 2017. [www.alberta.ca](http://www.alberta.ca).
- [63] M. P. Allen and D. J. Tildesley, *Computer Simulation of Liquids*. 1987.
- [64] “GROMACS User manual.” 2022.
- [65] U. Essmann, L. Perera, M. L. Berkowitz, T. Darden, H. Lee, and L. G. Pedersen, “A smooth particle mesh Ewald method,” *J. Chem. Phys.*, vol. 103, no. 19, pp. 8577–8593, 1995, doi: 10.1063/1.470117.
- [66] R. W. Hockney, S. P. Goel, and J. W. Eastwood, “Quiet high-resolution computer models of a plasma,” *J. Comput. Phys.*, vol. 14, no. 2, pp. 148–158, 1974, doi: 10.1016/0021-9991(74)90010-2.
- [67] L. Verlet, “Computer ‘Experiments’ on Classical Fluids. I. Thermodynamical Properties of Lennard-Jones Molecules,” *Phys. Rev.*, vol. 159, no. 1, pp. 98–103, 1976, doi: 10.1088/0022-3727/9/2/008.
- [68] W. C. Swope and H. C. Andersen, “A computer simulation method for the calculation of equilibrium constants for the formation of physical clusters of molecules: Application to small water clusters,” *J. Chem. Phys.*, vol. 76, no. 1, pp. 637–649, 1982.
- [69] K. Huang, “Statistical Mechanics (2nd edn),” in *John Wiley & Sons*, 1977, pp. 143–145.
- [70] H. J. C. Berendsen, J. P. M. Postma, W. F. van Gunsteren, A. DiNola, and J. R. Haak,

- “Molecular dynamics with coupling to an external bath,” *J. Chem. Phys.*, vol. 81, no. 8, p. 3684, 1984, doi: 10.1063/1.448118.
- [71] G. Bussi, D. Donadio, and M. Parrinello, “Canonical sampling through velocity rescaling,” *J. Chem. Phys.*, vol. 126, no. 1, p. 014101, 2007, doi: 10.1063/1.2408420.
- [72] S. Nosé, “A molecular dynamics method for simulations in the canonical ensemble,” *Mol. phys.*, vol. 52, no. 2, pp. 255–268, 1984.
- [73] W. G. Hoover, “Canonical dynamics: Equilibrium phase-space distributions,” *Phys. Rev. A*, vol. 31, no. 3, pp. 1695–1697, 1985.
- [74] H. C. Andersen, “Molecular dynamics simulations at constant pressure and/or temperature,” *J. Chem. Phys.*, vol. 72, no. 4, pp. 2384–2393, 1980, doi: 10.1063/1.439486.
- [75] M. Parrinello and A. Rahman, “Polymorphic transitions in single crystals : A new molecular dynamics method Polymorphic transitions in single crystals : A new molecular dynamics method,” *J. Appl. Phys.*, vol. 52, pp. 7182–7190, 1981, doi: 10.1063/1.328693.
- [76] G. J. Martyna, M. E. Tuckerman, D. J. Tobias, and M. L. Klein, “Explicit reversible integrators for extended systems dynamics,” *Mol. Phys.*, vol. 87, no. 5, pp. 1117–1157, 1996, doi: 10.1080/00268979600100761.
- [77] S. Alavi, “Molecular Simulations: Fundamentals and Practice,” in *Adhesion*, Wiley-VCH Verlag GmbH & Co. KGaA, 2020, p. 185.
- [78] D. C. Rapaport, R. L. Blumberg, S. R. McKay, and W. Christian, *The Art of Molecular Dynamics Simulation*, vol. 10, no. 5. AIP Publishing, 1996.
- [79] H. Kumar and P. K. Maiti, “Introduction to Molecular Dynamics Simulation,” in *Computational and statistical physics*, Gurgaon: Hindustan Book Agency, 2018, pp. 161–

192.

- [80] M. Griebel, G. Zumbusch, and S. Knapek, *Numerical Simulation in Molecular Dynamics*. Heidelberg: Springer Berlin, 2007.
- [81] A. D. MacKerell *et al.*, “All-atom empirical potential for molecular modeling and dynamics studies of proteins,” *J. Phys. Chem. B*, vol. 102, no. 18, pp. 3586–3616, 1998, doi: 10.1021/jp973084f.
- [82] W. L. Jorgensen and J. Tirado-rives, “The OPLS [optimized potentials for liquid simulations] potential functions for proteins, energy minimizations for crystals of cyclic peptides and crambin,” *J. Am. Chem. Soc.*, vol. 110, no. 6, pp. 1657–1666, 1988.
- [83] W. L. Jorgensen, D. S. Maxwell, and J. Tirado-Rives, “Development and testing of the OPLS all-atom force field on conformational energetics and properties of organic liquids,” *J. Am. Chem. Soc.*, vol. 118, no. 45, pp. 11225–11236, 1996, doi: 10.1021/ja9621760.
- [84] E. Neria, S. Fischer, and M. Karplus, “Simulation of activation free energies in molecular systems,” *J. Chem. Phys.*, vol. 105, no. 5, pp. 1902–1921, 1996, doi: 10.1063/1.472061.
- [85] W. R. P. Scott *et al.*, “The GROMOS biomolecular simulation program package,” *J. Phys. Chem.A*, vol. 103, no. 19, pp. 3596–3607, 1999, doi: 10.1021/jp984217f.
- [86] W. F. van Gunsteren and H. J. C. Berendsen, “Groningen Molecular Simulation ({GROMOS}) Library Manual,” *Biomos, Groningen*, 1987.
- [87] K. A. Maerzke, N. E. Schultz, R. B. Ross, and J. I. Siepmann, “TraPPE-UA force field for acrylates and Monte Carlo simulations for their mixtures with Alkanes and alcohols,” *J. Phys. Chem. B*, vol. 113, no. 18, pp. 6415–6425, 2009, doi: 10.1021/jp810558v.
- [88] M. G. Martin and J. I. Siepmann, “Transferable potentials for phase equilibria. 1. United-

- atom description of n-alkanes,” *J. Phys. Chem. B*, vol. 102, no. 14, pp. 2569–2577, 1998, doi: 10.1021/jp972543+.
- [89] L. Monticelli, S. K. Kandasamy, X. Periole, R. G. Larson, D. P. Tieleman, and S.-J. Marrink, “The MARTINI Coarse-Grained Force Field: Extension to Proteins,” *J. Chem. Theory Comput.*, vol. 4, no. 5, pp. 819–834, May 2008, doi: 10.1021/ct700324x.
- [90] S. O. Yesylevskyy, L. V. Schäfer, D. Sengupta, and S. J. Marrink, “Polarizable water model for the coarse-grained MARTINI force field,” *PLoS Comput. Biol.*, vol. 6, no. 6, pp. 1–17, 2010, doi: 10.1371/journal.pcbi.1000810.
- [91] A. Satoh, *Introduction to Practice of Molecular Simulation*. Elsevier, 2011.
- [92] M. Diem and C. Oostenbrink, “The effect of different cutoff schemes in molecular simulations of proteins,” *J. Comput. Chem.*, vol. 41, no. 32, pp. 2740–2749, 2020, doi: 10.1002/jcc.26426.
- [93] P. Del Moral and S. Penev, *Computational and statistical physics*. 2018.
- [94] V. Kumar, C. R. Locker, P. J. in ’t Veld, and G. C. Rutledge, “Effect of Short Chain Branching on the Interlamellar Structure of Semicrystalline Polyethylene The,” *Macromolecules*, vol. 50, no. 3, pp. 1206–1214, 2017.
- [95] S. H. Jeong, J. M. Kim, J. Yoon, C. Tzoumanekas, M. Kröger, and C. Baig, “Influence of molecular architecture on the entanglement network: Topological analysis of linear, long- and short-chain branched polyethylene melts via Monte Carlo simulations,” *Soft Matter*, vol. 12, no. 16, pp. 3770–3786, 2016, doi: 10.1039/c5sm03016a.
- [96] M. E. Tuckerman, *Statistical Mechanics: Theory and Molecular Simulation*. Oxford University Press, 2023.

- [97] S. Kavyani, S. Amjad-iranagh, and M. Zarif, “Effect of temperature, pH, and terminal groups on structural properties of carbon nanotube-dendrimer composites: A coarse-grained molecular dynamics simulation study,” *J. Mol. Liq.*, vol. 363, p. 119825, 2022, doi: <https://doi.org/10.1016/j.molliq.2022.119825>.
- [98] S. Kavyani, M. Dadvar, H. Modarress, and S. Amjad-Iranagh, “Molecular perspective mechanism for drug loading on carbon nanotube-dendrimer: A coarse-grained molecular dynamics study,” *J. Phys. Chem. B*, vol. 122, no. 33, pp. 7956–7969, 2018, doi: 10.1021/acs.jpcc.8b04434.
- [99] S. Kavyani, S. Amjad-iranagh, M. Dadvar, and H. Modarress, “Hybrid Dendrimers of PPI(core) – PAMAM(shell): A Molecular Dynamics Simulation Study,” *J. Phys. Chem. B*, vol. 120, pp. 9564–9575, 2016, doi: 10.1021/acs.jpcc.6b05142.
- [100] J.-P. Hansen and I. R. McDonald, *Theory of Simple Liquids*, vol. 53, no. 9. New York, 1986.
- [101] D. Chandler, “Reduced Configurational Distributions Functions,” in *Introduction to Modern Statistical Mechanics*, Oxford University Press, 1987, p. 198.
- [102] J.-P. Hansen and I. R. McDonald, “Particle densities and distribution functions,” in *Theory of Simple Liquids*, 1986, p. 28.
- [103] D. Frenkel, B. Smit, J. Tobochnik, S. R. McKay, and W. Christian, “Understanding Molecular Simulation,” *Comput. Phys.*, vol. 11, no. 4, pp. 351–354, 1997.
- [104] P. A. Burrough, R. A. McDonnell, and C. D. Lloyd, “Nierest Neighbours: Thiessen Polygons,” in *Principles of Geographical Information Systems*, Oxford University Press, 2015, p. 160.
- [105] A. Okabe, *Spatial Tessellations*, Second Edi. 2000.

- [106] F. Aurenhammer, “Voronoi diagrams—a survey of a fundamental geometric data structure,” *ACM*, vol. 23, no. 3, pp. 345–405, 1991, doi: 10.1145/116873.116880.
- [107] Joe Jordan, “2D and 3D Voronoi tessellations: a python entry point for the voro++ library,” 2014. <https://github.com/joe-jordan/pyvoro>.
- [108] C. H. Rycroft, “Voro++: a general overview,” 2013. <https://math.lbl.gov/voro++/about.html>.
- [109] C. H. Rycroft, “VORO++: A three-dimensional Voronoi cell library in C++,” *Chaos*, vol. 19, no. 4, 2009, doi: 10.1063/1.3215722.
- [110] C. H. Rycroft, G. S. Grest, J. W. Landry, and M. Z. Bazant, “Analysis of granular flow in a pebble-bed nuclear reactor,” *Phys. Rev. E*, vol. 74, no. 2, pp. 1–16, 2006, doi: 10.1103/PhysRevE.74.021306.
- [111] C. H. Rycroft, “Multiscale modeling in granular flow,” 2007.
- [112] C. P. J. Wong and P. Choi, “A free volume theory on the chain length dependence of the diffusivity of linear polymers,” *Soft Matter*, vol. 15, no. 45, pp. 9300–9309, 2019, doi: 10.1039/c9sm01900f.
- [113] P. Hittmair and R. Ullman, “Environmental stress cracking of polyethylene,” *J. Appl. Polym. Sci.*, vol. 6, no. 19, pp. 1–14, 1962, doi: 10.1002/app.1962.070061901.
- [114] R. S. Chen, Y. H. Muhammad, and S. Ahmad, “Physical, mechanical and environmental stress cracking characteristics of epoxy/glass fiber composites: Effect of matrix/fiber modification and fiber loading,” *Polym. Test.*, vol. 96, p. 107088, 2021, doi: 10.1016/j.polymertesting.2021.107088.
- [115] L. M. Robeson, “Environmental Stress Cracking: A Review,” *Polym. Eng. Sci.*, vol. 53, no.

- 3, pp. 1–10, 2012, doi: 10.1002/pen.
- [116] J. A. Jansen, “Environmental Stress Cracking - The Plastic Killer,” *Adv. Mater. Process.*, vol. 27, no. 2, 2008, doi: 10.2307/j.ctvfjd02q.6.
- [117] D. Van Der Spoel, E. Lindahl, B. Hess, G. Groenhof, A. E. Mark, and H. J. C. Berendsen, “GROMACS: fast, flexible, and free,” *J. Comput. Chem.*, vol. 26, no. 16, pp. 1701–1718, Dec. 2005, doi: 10.1002/jcc.20291.
- [118] B. Hess and C. Kutzner, “GROMACS 4: Algorithms for highly efficient, load-balanced, and scalable molecular simulation,” *J. Chem. Theory Comput.*, vol. 4, pp. 435–447, 2008, doi: 10.1021/ct700301q.
- [119] A. Toda, K. Taguchi, K. Nozaki, and M. Konishi, “Melting behaviors of polyethylene crystals: An application of fast-scan DSC,” *Polymer (Guildf.)*, vol. 55, no. 14, pp. 3186–3194, 2014, doi: 10.1016/j.polymer.2014.05.009.
- [120] G. Bussi, D. Donadio, and M. Parrinello, “Canonical sampling through velocity rescaling Giovanni,” *J. Chem. Phys.*, vol. 126, no. 1, p. 14101, 2007.
- [121] D. L. Faulkner, “The role of surfactant structure and monoethanolamine in the environmental stress cracking of polycarbonate,” *J. Appl. Polym. Sci.*, vol. 32, no. 5, pp. 4909–4917, 1986, doi: 10.1002/app.1986.070320513.
- [122] F. L. Scholten, J. Pisters, and B. Venema, “A more reliable detergent for constant load experiments on polyethylene,” *Polym. Test.*, vol. 8, no. 6, pp. 385–405, 1988, doi: 10.1016/0142-9418(88)90042-6.
- [123] P. D. Frayer, P. P. Tong, and W. W. Dreher, “The role of intercrystalline links in the environmental stress cracking of high density polyethylene,” *Polym. Eng. Sci.*, vol. 17, no.

- 1, pp. 27–31, 1977, doi: 10.1002/pen.760170105.
- [124] T. G. Fox and P. J. Flory, “SecondOrder transition temperatures and related properties of polystyrene. I. Influence of molecular weight,” *J. Appl. Phys.*, vol. 21, no. 6, pp. 581–591, 1950, doi: 10.1063/1.1699711.
- [125] S. Capponi, F. Alvarez, and D. Rackó, “Free volume in a PVME polymer–water solution,” *Macromolecules*, vol. 53, no. 12, pp. 4770–4782, 2020, doi: 10.1021/acs.macromol.0c00472.
- [126] A. Lustiger and R. L. Markham, “Importance of tie molecules in preventing polyethylene fracture under long-term loading conditions,” *Polymer (Guildf.)*, vol. 24, no. 12, pp. 1647–1654, 1983, doi: 10.1016/0032-3861(83)90187-8.
- [127] A. Lustiger and N. Ishikawa, “An analytical technique for measuring relative tie- molecule concentration in polyethylene,” *J. Polym. Sci., Part B Polym. Phys.*, vol. 29, no. 9, pp. 1047–1055, 1991, doi: 10.1002/polb.1991.090290902.
- [128] L. Hubert, L. David, R. Séguéla, G. Vigier, C. Corfias-Zuccalli, and Y. Germain, “Physical and mechanical properties of polyethylene for pipes in relation to molecular architecture. II. Short-term creep of isotropic and drawn materials,” *J. Appl. Polym. Sci.*, vol. 84, no. 12, pp. 2308–2317, 2002, doi: 10.1002/app.10538.
- [129] X. Lu, Z. Zhou, and N. Brown, “A sensitive mechanical test for slow crack growth in polyethylene,” *Polym. Eng. Sci.*, vol. 37, no. 11, pp. 1896–1900, 1997, doi: 10.1002/pen.11839.
- [130] L. Hubert, L. David, R. Séguéla, G. Vigier, C. Degoulet, and Y. Germain, “Physical and mechanical properties of polyethylene for pipes in relation to molecular architecture. I.

- Microstructure and crystallisation kinetics,” *Polymer (Guildf)*., vol. 42, no. 20, pp. 8425–8434, 2001, doi: 10.1016/S0032-3861(01)00351-2.
- [131] R. K. Krishnaswamy, Q. Yang, L. Fernandez-Ballester, and J. A. Kornfield, “Effect of the distribution of short-chain branches on crystallization kinetics and mechanical properties of high-density polyethylene,” *Macromolecules*, vol. 41, no. 5, pp. 1693–1704, 2008, doi: 10.1021/ma070454h.
- [132] R. P. White and J. E. G. Lipson, “Polymer Free Volume and Its Connection to the Glass Transition,” *Macromolecules*, vol. 49, no. 11, pp. 3987–4007, 2016, doi: 10.1021/acs.macromol.6b00215.
- [133] E. Von Meerwall, S. Beckman, J. Jang, and W. L. Mattice, “Diffusion of liquid n-alkanes: Free-volume and density effects,” *J. Chem. Phys.*, vol. 108, no. 10, pp. 4299–4304, 1998, doi: 10.1063/1.475829.
- [134] C. P. J. Wong and P. Choi, “Prediction of crossover in the molecular weight dependence of polyethylene viscosity using a polymer free volume theory,” *Soft Matter*, vol. 16, no. 32, pp. 7458–7469, 2020, doi: 10.1039/d0sm00752h.
- [135] S. Kavyani and P. Choi, “Molecular dynamics study of the environmental stress cracking agent assisted cavitation in linear and branched polyethylene,” *Polymer (Guildf)*., vol. 264, no. 3, p. 125542, 2023, doi: 10.1016/j.polymer.2022.125542.
- [136] J. L. Jordan, D. T. Casem, J. M. Bradley, A. K. Dwivedi, E. N. Brown, and C. W. Jordan, “Mechanical Properties of Low Density Polyethylene,” *J. Dyn. Behav. Mater.*, vol. 2, no. 4, pp. 411–420, 2016, doi: 10.1007/s40870-016-0076-0.
- [137] P. Olesik, M. Godzierz, M. Kozioł, J. Jała, U. Szeluga, and J. Myalski, “Structure and

- mechanical properties of high-density polyethylene composites reinforced with glassy carbon,” *Materials (Basel)*., vol. 14, no. 14, pp. 1–10, 2021, doi: 10.3390/ma14144024.
- [138] P. Sardashti, A. J. Scott, C. Tzoganakis, M. A. Polak, and A. Penlidis, “Effect of temperature on environmental stress cracking resistance and crystal structure of Polyethylene,” *J. Macromol. Sci. A J MACROMOL SCI A*, vol. 51, no. 3, pp. 189–202, 2014, doi: 10.1080/10601325.2014.871934.
- [139] P. J. DesLauriers and M. P. McDaniel, “Stability and Utility of Pyridyl Disulfide Functionality in RAFT and Conventional Radical Polymerizations,” *J. Polym. Sci. A Polym. Chem.*, vol. 46, no. April, pp. 7207–7224, 2008, doi: 10.1002/pola.
- [140] R. Li, “Environmental degradation of wood-HDPE composite,” *Polym. Degrad. Stab.*, vol. 70, no. 2, pp. 135–145, 2000, doi: 10.1016/S0141-3910(00)00099-9.
- [141] E. M. Abdel-Bary, M. N. Ismail, A. A. Yehia, and A. A. Abdel-Hakim, “Recycling of polyethylene films used in greenhouses - Development of multilayer plastic films,” *Polym. Degrad. Stab.*, vol. 62, no. 1, pp. 111–115, 1998, doi: 10.1016/S0141-3910(97)00267-X.
- [142] A. M. Henderson, “Ethylene-Vinyl Acetate (EVA) Copolymers: A General Review,” *IEEE Electr. Insul. Mag.*, vol. 9, no. 1, pp. 30–38, 1993, doi: 10.1109/57.249923.
- [143] O. Y. Alothman, “Processing and characterization of high density polyethylene/ethylene vinyl acetate blends with different VA contents,” *Adv. Mater. Sci. Eng.*, vol. 2012, 2012, doi: 10.1155/2012/635693.
- [144] V. V. Novikov, “The Thermal and Mechanical Properties of Poly(ethylene-co-vinyl acetate) Random Copolymers (PEVA) and its Covalently Crosslinked Analogues (cPEVA),” *Polymers (Basel)*., vol. 34, no. 5, pp. 688–694, 1996.

- [145] H. A. Khonakdar, U. Wagenknecht, S. H. Jafari, R. Hässler, and H. Eslami, “Dynamic mechanical properties and morphology of polyethylene/ethylene vinyl acetate copolymer blends,” *Adv. Polym. Technol.*, vol. 23, no. 4, pp. 307–315, 2004, doi: 10.1002/adv.20019.
- [146] N. T.-H. Pham, “Characterization of Low-Density Polyethylene and LDPE-Based/Ethylene-Vinyl Acetate with Medium Content of Vinyl,” *Polymers (Basel)*., vol. 13, no. 14, p. 2352, 2021.
- [147] Y. Chen, “Investigations of environmental stress cracking resistance of HDPE/EVA and LDPE/EVA blends,” *J. Appl. Polym. Sci.*, vol. 131, no. 4, pp. 1–8, 2014, doi: 10.1002/app.39880.
- [148] B. Borisova and J. Kressler, “Environmental stress-cracking resistance of LDPE/EVA blends,” *Macromol. Mater. Eng.*, vol. 288, no. 6, pp. 509–515, 2003, doi: 10.1002/mame.200390048.
- [149] M. J. Wisotsky, A. E. Kober, and I. A. Zlochower, “Copolymerization of ethylene with vinyl acetate. I. Effect of polymerization temperature on degree of branching,” *J. Appl. Polym. Sci.*, vol. 15, no. 7, pp. 1737–1742, 1971, doi: 10.1002/app.1971.070150717.
- [150] D. H. Bailey and P. N. Swarztrauber, “A Fast Method for the Numerical Evaluation of Continuous Fourier and Laplace Transforms,” *SIAM J. Sci. Comput.*, vol. 15, no. 5, pp. 1105–1110, 1994, doi: 10.1137/0915067.
- [151] M. D. Adams, *Signals and systems*. 2020.
- [152] W. Kaplan, *Advanced Calculus*. Fifth Edition: Addison Wesley Publishing Company, 2002.